

A Sponsored Supplement to *Science*

Sharper images: Exploring confocal and superresolution microscopy

Sponsored by

Produced by the
Science/AAAS Custom
Publishing Office



Science
AAAS

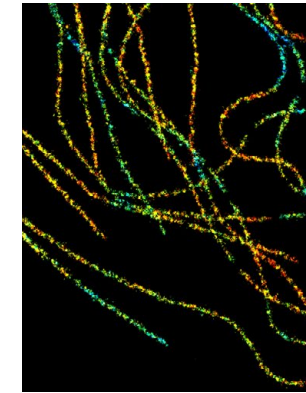
Science Careers

FROM THE JOURNAL SCIENCE AAAS

Step up your job search with *Science* Careers

- Access thousands of job postings
- Sign up for job alerts
- Explore career development tools and resources

Search jobs on [ScienceCareers.org](https://www.sciencecareers.org) today



Sharper images: Exploring confocal and superresolution microscopy

About the cover: 3D superresolution image of microtubules acquired with Nikon N-STORM. Colors represent z-depth.

This booklet was produced by the *Science*/AAAS Custom Publishing Office and sponsored by NIKON.

Editors: Jackie Oberst, Ph.D.; Sean Sanders, Ph.D.
Proofreader/Copyeditor: Bob French
Designer: Amy Hardcastle

ROGER GONCALVES, ASSOCIATE SALES DIRECTOR
Custom Publishing
Europe, Middle East, and India
rgoncalves@science-int.co.uk
+41-43-243-1358

© 2017 by The American Association for the Advancement of Science. All rights reserved. 22 September 2017

Introductions

- 2 Moore's law realized in microscopy
Jackie Oberst, Ph.D.
Sean Sanders, Ph.D.
Science/AAAS
- 3 Matching resolution to your application
Lynne Chang, Ph.D.
Strategic Marketing Manager
Nikon Instruments Inc.

Research articles

- 4 Superresolution imaging of the cytoplasmic phosphatase PTPN22 links integrin-mediated T cell adhesion with autoimmunity
Garth L. Burn, Georgina H. Cornish, Katarzyna Potrzebowska *et al.*
- 15 GTPase activity-coupled treadmilling of the bacterial tubulin FtsZ organizes septal cell wall synthesis
Xinxing Yang, Zhixin Lyu, Amanda Miguel *et al.*
- 20 Sequential transcriptional waves direct the differentiation of newborn neurons in the mouse neocortex
Ludovic Telley, Subashika Govindan, Julien Prados *et al.*
- 25 Expansion microscopy
Fei Chen, Paul W. Tillberg, Edward S. Boyden

White paper

- 31 Latest innovations in Nikon confocal technology
Adam White, Ph.D.
Biosystems Product Manager, Confocal and Super-Resolution
Nikon Instruments Inc.

Application note

- 34 The spectrum of resolution: Confocal, SIM, and STORM
John R. Allen
Applications and Marketing Specialist
Nikon Instruments Inc.



Moore's law realized in microscopy

Advances in confocal technologies seem to emerge with increasing regularity.

Confocal microscopy has become the workhorse of cell biology. It is rare not to see these instruments in the average life science laboratory. And advances in confocal technologies seem to emerge with increasing regularity. In fact, it could be argued that Moore's law—describing his observation that the number of transistors that fits onto a computer's integrated circuits doubles approximately every two years, bringing advances in speed and declines in cost—could be applied to the microscopy field.

Whereas a conventional (i.e., widefield) fluorescent microscope can only "see" as far as the light can penetrate, and leaves a blurred, unfocused background, a confocal microscope eliminates the out-of-focus signal for a more in-depth, 3D image. Algorithms can be developed to further sharpen the edges of a specimen under a confocal microscope, a process known as deconvolution.

The detail that can be seen in an object—the resolution—of a light microscope is limited by the diffraction of light through the instrument's lens opening, or aperture. Superresolution techniques, as the name indicates, allow images to be seen with a higher resolution—past the diffraction limit of light. The 2014 Nobel Prize in Chemistry was awarded to Eric Betzig, William E. Moerner, and Stefan Hell for "the development of super-resolved fluorescence microscopy," which brings "optical microscopy into the nanodimension."

Superresolution methods such as stochastic optical reconstruction microscopy (STORM) use photoactivatable or photoswitchable fluorescent dyes or proteins that randomly emit at different times, enabling precise, nanometer-scale localization of molecules. Structured illumination microscopy (SIM) takes advantage of interference patterns generated from finely structured light interacting with objects in the specimen to collect superresolution information. Expansion microscopy physically expands the specimen, using a polymer system, to resolve diffraction-limited objects using conventional microscopes.

The selection of articles in this booklet reflects these latest microscopy techniques. Clearly there is no one-size-fits-all instrument in the imaging world. Researchers must determine what their trade-offs will be in terms of imaging depth, resolution, phototoxicity, and speed. However, most will find that confocal microscopy offers, as one article author explains, "more limited resolution improvement, but otherwise all-around robust performance well suited towards a variety of research needs."

We hope you enjoy these articles. Perhaps they will propel you to use these techniques or inspire you to develop some of your own.

Jackie Oberst, Ph.D.

Sean Sanders, Ph.D.

Custom Publishing Office
Science/AAAS



Matching resolution to your application

Nikon continues to invest in improving the functionality and performance of our confocal systems.

Recent years have seen a variety of confocal-based imaging solutions enter the commercial marketplace that bridge the resolution gap between widefield and superresolution microscopy. With the range of resolutions that are now achievable, the process of matching an imaging system to an application is not always straightforward. Balancing resolution against speed, throughput, and even ease of sample preparation becomes critical when making these selections. For example, a twofold improvement in resolution may provide significant new insights into certain biological processes without sacrificing the ability to capture live events. Conversely, a 10-fold resolution gain realized with localization-based techniques may be a necessity when studying molecular interactions, and worth the sacrifice in acquisition speed. Furthermore, a $\sqrt{2}$ improvement in resolution may be enough to supply the additional clarity needed to understand a phenomenon while retaining all the advantages of a robust confocal system.

The "Spectrum of Resolution" application note in this booklet outlines the different superresolution and "enhanced resolution" technologies that Nikon offers, including the benefits and limitations of each system. It also presents figures showing the resolutions obtained by each technology using nanoruler resolution standards. We have also included a white paper entitled "The Latest Innovations in Nikon Confocal Technology." Despite the introduction of superresolution imaging techniques, confocal systems continue to furnish a robust imaging platform for many research labs and are often the most widely used instruments in core facilities. Nikon continues to invest in improving the functionality and performance of our confocal systems, including a new high-resolution 1K resonant scanner, a flexible spectral detector, and an Enhanced Resolution module for achieving sharper confocal images.

This collection of research articles highlights the benefits of the different imaging technologies (e.g., N-SIM, N-STORM, and A1 confocal) for their particular application. Also included is an original article introducing the concept of expansion microscopy, which enables users to achieve superresolution using non-superresolution imaging platforms, a novel concept and a field that has recently garnered much interest from the scientific community. We hope this booklet provides a timely review of innovations and applications in both the confocal and superresolution technology space, and aids the reader in selecting the best imaging technology for their research.

Lynne Chang, Ph.D.

Strategic Marketing Manager
Nikon Instruments Inc.

RESEARCH ARTICLE

IMMUNOLOGY

Superresolution imaging of the cytoplasmic phosphatase PTPN22 links integrin-mediated T cell adhesion with autoimmunity

Garth L. Burn,¹ Georgina H. Cornish,¹ Katarzyna Potrzebowska,² Malin Samuelsson,² Juliette Griffié,³ Sophie Minoughan,³ Mark Yates,¹ George Ashdown,³ Nicolas Pernodet,² Vicky L. Morrison,⁴ Cristina Sanchez-Blanco,¹ Harriet Purvis,¹ Fiona Clarke,¹ Rebecca J. Brownlie,⁵ Timothy J. Vyse,⁶ Rose Zamoyska,⁵ Dylan M. Owen,^{3*} Lena M. Svensson,^{2**†} Andrew P. Cope,^{1**†}

Integrins are heterodimeric transmembrane proteins that play a fundamental role in the migration of leukocytes to sites of infection or injury. We found that protein tyrosine phosphatase nonreceptor type 22 (PTPN22) inhibits signaling by the integrin lymphocyte function-associated antigen-1 (LFA-1) in effector T cells. PTPN22 colocalized with its substrates at the leading edge of cells migrating on surfaces coated with the LFA-1 ligand intercellular adhesion molecule-1 (ICAM-1). Knockout or knockdown of *PTPN22* or expression of the autoimmune disease-associated PTPN22-R620W variant resulted in the enhanced phosphorylation of signaling molecules downstream of integrins. Superresolution imaging revealed that PTPN22-R620 (wild-type PTPN22) was present as large clusters in unstimulated T cells and that these disaggregated upon stimulation of LFA-1, enabling increased association of PTPN22 with its binding partners at the leading edge. The failure of PTPN22-R620W molecules to be retained at the leading edge led to increased LFA-1 clustering and integrin-mediated cell adhesion. Our data define a previously uncharacterized mechanism for fine-tuning integrin signaling in T cells, as well as a paradigm of autoimmunity in humans in which disease susceptibility is underpinned by inherited phosphatase mutations that perturb integrin function.

INTRODUCTION

Integrins function as adhesion receptors that control cell-cell and cell-matrix interactions, thereby regulating the migration of cells into tissues. Lymphocyte function-associated antigen-1 (LFA-1; also known as CD11a/CD18 or $\alpha_L\beta_2$ integrin) is the major integrin used by T cells. In addition to mediating T cell adhesion and migration, LFA-1 transduces environmental cues that affect a wide range of cellular functions,

including cell differentiation, proliferation, cytokine production, cytotoxicity, and cell survival (1–6). Optimal function requires changes in the conformation and clustering of LFA-1 in ways that promote cell adherence, which are achieved through two distinct, yet overlapping, signaling pathways (7). Inside-out signaling is initiated by antigen or chemokine receptors and results in conformational changes in LFA-1 that increase its affinity for its ligands, such as intercellular adhesion molecule-1 (ICAM-1), and the binding of cytoplasmic signaling modules to integrin tails (8, 9). Outside-in signaling is initiated after LFA-1 engages ICAM-1, and it leads to the Src- and Syk-mediated phosphorylation of tyrosines, the plasma membrane translocation of Rap1 (Ras-related protein 1), and the binding of talin and kindlin-3 to the cytoplasmic tail of the β_2 subunit of LFA-1 (3, 10). Although counterregulation of LFA-1-dependent protein tyrosine phosphorylation is required for repeated cycles of adhesion, de-adhesion, protrusion, and contraction of T cells (11, 12), the protein tyrosine

phosphatases that support this function are not well understood.

Protein tyrosine phosphatase nonreceptor type 22 (PTPN22; also known as Lyp in humans and PEP in mice) is a protein tyrosine phosphatase that dephosphorylates Src and Syk family kinases (13). Interest in PTPN22 has grown considerably since initial reports of strong associations between a missense single-nucleotide polymorphism in the *PTPN22* gene (1858C>T, encoding the R620W variant) and a growing number of autoimmune diseases, including type 1 diabetes, rheumatoid arthritis, and systemic lupus erythematosus (14). Functional studies have focused on how the phosphatase regulates antigen receptor signaling in lymphocytes, but precisely how the R620W variant confers susceptibility to autoimmune disease is unknown. The fact that the R620W mutation targets the P1 polyproline domain of PTPN22 has raised the possibility that impaired interactions between the mutant phosphatase and the Src homology 3 (SH3) domain of C-terminal Src kinase (Csk), a negative regulator of Src family kinases, could disrupt mechanisms that have evolved to attenuate antigen receptor signaling in lymphocytes (14). Despite these insights, some studies have suggested that the R620W variant is a loss-of-function mutation, whereas others pointed to a gain of function (15, 16). Here, we investigated whether PTPN22 regulated LFA-1-mediated signaling because the kinases Lck and ZAP70, which are substrates of PTPN22, are also phosphorylated after engagement of LFA-1 (17, 18). Our experiments were also motivated by the possibility that perturbations in integrin signaling might play a role in provoking immune-mediated inflammatory diseases in individuals carrying the PTPN22-R620W variant.

RESULTS

PTPN22 colocalizes with its substrates at the leading edge of migrating T cells

To examine whether PTPN22 regulated outside-in integrin signaling, we plated activated primary human T cells onto ICAM-1-coated glass and then fixed, stained, and imaged the cells by confocal microscopy. PTPN22 mainly polarized to the lamellipodium at the leading edge of migrating T cells (on ICAM-1), with some staining in the uropod, whereas PTPN22 was not polarized in nonmigrating T cells on glass coated with poly-L-lysine (PLL) (Fig. 1A). Specificity of staining was confirmed by gene knockdown, by analysis of patterns of staining obtained with monoclonal and polyclonal

antibodies specific for PTPN22, and by localization studies with T cells expressing green fluorescent protein (GFP)-tagged PTPN22 (PTPN22-GFP) (fig. S1, A to C). Confocal microscopy and fluorescence intensity plots revealed the phosphorylation of activating tyrosine residues on Lck (pY394), ZAP70 (pY493), and Vav (pY174), which were colocalized with PTPN22 at the leading edge of migrating cells (Fig. 1A and fig. S1D) but not nonmigrating cells (fig. S1E). Analysis and quantification of total internal reflection fluorescence (TIRF) microscopy images confirmed the plasma membrane-proximal associations between PTPN22 and its phosphorylated substrates at the leading edge of migrating T cells, when compared to nonmigrating T cells on PLL (fig. S2, A and B).

Integrin signaling stimulates an association between PTPN22 and its phosphorylated substrates

Biochemical analysis of whole-cell lysates confirmed the inducible phosphorylation of integrin signaling intermediates in migrating T cells in response to different integrin ligands (fig. S3, A and B), and the specificity of this response was confirmed in experiments with soluble anti-ICAM-1 antibodies (fig. S3C). Lysates of nonmigrating and migrating cells were subjected to immunoprecipitation with an anti-PTPN22 antibody and were then analyzed by Western blotting with an anti-phosphotyrosine antibody. Whereas a single phosphoprotein band was detected in the nonmigrating T cells, many more phosphoprotein bands were detected in the migrating T cells, suggesting the inducible association of PTPN22 with phosphotyrosine substrates (fig. S3D). Three of these bands resolved to molecular masses corresponding to phosphorylated Lck (56 kDa), ZAP70 (70 kDa), and Vav (118 kDa). The specificity of these interactions and the associations between these substrates and PTPN22 over time were confirmed by Western blotting analysis of anti-PTPN22 immunoprecipitates with phosphospecific antibodies (Fig. 1B). Furthermore, PTPN22 associated only with phosphorylated protein substrates, as suggested by Western blotting analysis of total Lck and ZAP70 abundances (Fig. 1B), which indicates that the phosphorylation of its substrates in migrating T cells was required for their interaction with PTPN22.

PTPN22 is an inhibitor of integrin signaling, and the R620W variant is a loss-of-function mutant

Targeting *PTPN22* with small interfering RNA (siRNA) reduced the abundance of PTPN22 protein in migrating primary

human T cells by ~50 to 60%, without affecting the abundance of LFA-1 (fig. S3E), but increased the ICAM-1-dependent phosphorylation of Lck (pY394), ZAP70 (pY493), and Vav (pY174) when compared to that in migrating cells treated with control siRNA (Fig. 1C). Unlike for pY493-ZAP70, there was a less pronounced increase in the phosphorylation of the regulatory Tyr³¹⁹ site of ZAP70, which is not a target of PTPN22 (13). *PTPN22* knockdown was also associated with increased T cell motility (Fig. 1D), whereas overexpression of the GFP-tagged PTPN22-R620 variant (wild type), but not a catalytically inactive C227A variant or GFP alone, in PTPN22-sufficient T cells reduced cell motility (Fig. 1E). The phosphatase activity of PTPN22 was therefore required for the regulation of integrin-mediated cell motility. Integrin-dependent phosphorylation of the classical mitogen-activated protein kinases (MAPKs) extracellular signal-regulated kinase 1 (ERK1) and ERK2 (collectively referred to as ERK1/2) was also observed after engagement of LFA-1 (Fig. 1C), consistent with its localization in nascent adhesion complexes and its contribution to the “motor phase” of lamellipodium protrusion (19–21). ERK1/2 phosphorylation was blocked by the Lck inhibitor PP2 (fig. S3F), suggesting that the integrin-dependent activation of Lck was upstream of ERK phosphorylation, as previously reported (18). Consistent with these data, ERK1/2 phosphorylation was enhanced in migrating *Ptpn22*^{-/-} murine T cells (Fig. 1F) and in human T cells carrying either one or two copies of the *PTPN22* genetic variant encoding PTPN22-W620 (Fig. 1G). These data suggest that PTPN22 is an inhibitor of LFA-1 signaling and that the R620W variant is a loss-of-function mutant.

PTPN22 and Csk localize in plasma membrane-proximal clusters that decluster during LFA-1-stimulated migration

Diffraction-limited microscopy showed substantial localization of PTPN22 at the leading edge of migrating T cells after engagement of LFA-1 (Fig. 1A). To obtain quantitative imaging data of this phenomenon at the plasma membrane, we used TIRF-direct stochastic optical reconstruction microscopy (dSTORM) superresolution microscopy and quantitative cluster analysis. These techniques quantify protein (localization) and cluster number, as well as cluster size and the density of PTPN22 protein localized at the plasma membrane of stationary cells or at the leading edge of migrating T cells. The visualization of single molecules can be represented by point maps and cluster heat maps. Using this approach, we found that

PTPN22 was highly clustered at the plasma membrane of nonmigrating T cells (plated on PLL), whereas migrating T cells contained smaller, less dense clusters (Fig. 2A), which was confirmed by quantitative cluster analysis (Fig. 2, B and C); localizations per cluster (Fig. 2C) reflect the number of PTPN22 molecules per cluster. Quantification by Ripley's K function, a measure of the extent of clustering, also revealed a substantial reduction in clustering [peak of $L(r)-r$ curve] and the presence of smaller clusters (position of the peak on the x axis) at the leading edge (Fig. 2D), further confirming that PTPN22 was substantially less clustered in migrating T cells.

Csk also exhibited this declustering phenomenon upon stimulation of LFA-1 (15% of localizations were in clusters of migrating cells versus 30% in nonmigrating cells), although the heat maps revealed more heterogeneity in Csk clusters compared to those of PTPN22 (fig. S4, A to C). Concurrent with the LFA-1-dependent declustering of PTPN22 and Csk, we detected increased association between the phosphatase and the kinase in cell lysates immunoprecipitated with antibodies against either PTPN22 or Csk (fig. S4, D and E), whereas the adaptor protein associated with glycolipid-enriched microdomains (PAG, also known as Csk-binding protein) (22) had less Csk and PTPN22 associated with it in ICAM-1-stimulated cells (fig. S4, F and G). Consistent with these findings, tyrosine phosphorylation of PAG, which promotes the association between PAG and Csk and the retention of Csk in plasma membrane microdomains (23), was also reduced upon engagement of LFA-1 (fig. S4H). These data indicate that the declustering of both PTPN22 and Csk coincides with the dissociation of Csk from dephosphorylated PAG and the increased association of PTPN22 with Csk.

Nanoscale organization of PTPN22-R620 and PTPN22-W620 clusters in migrating T cells

Closer examination of PTPN22-R620 localizations at the nanoscale level revealed that the transition from the nonmigrating to the migrating state was associated with three cluster characteristics. First, there was a modest reduction in the total number of clusters (Fig. 3A, closed symbols). Second, PTPN22-R620-containing clusters became smaller, which is based on a marked reduction in the percentage of PTPN22 molecules that occurred within clusters (Fig. 3B, closed symbols), which is consistent with the cluster heat maps and the changes in the diameter and density of clusters upon stimulation with ICAM-1 (Fig. 2, A to

¹Academic Department of Rheumatology, Centre for Molecular and Cellular Biology of Inflammation, Faculty of Life Sciences and Medicine, King's College London, London SE1 1UL, U.K.

²Department of Experimental Medical Science, Lund University, 221 84 Lund, Sweden. ³Department of Physics and Randall Division of Cell and Molecular Biophysics, Faculty of Life Sciences and Medicine, King's College London, London SE1 1UL, U.K. ⁴Institute of Immunology, Infection and Inflammation, University of Glasgow, Glasgow G12 8TA, U.K. ⁵Institute of Immunology and Infection Research, Centre for Immunity, Infection and Evolution, University of Edinburgh, Edinburgh EH9 3FL, U.K. ⁶Department of Medical and Molecular Genetics, Faculty of Life Sciences and Medicine, King's College London, London SE1 9RT, U.K.

*These senior authors contributed equally to this work.

†Corresponding author. Email: andrew.cope@kcl.ac.uk (A.P.C.); lena.m.svensson@med.lu.se (L.M.S.)

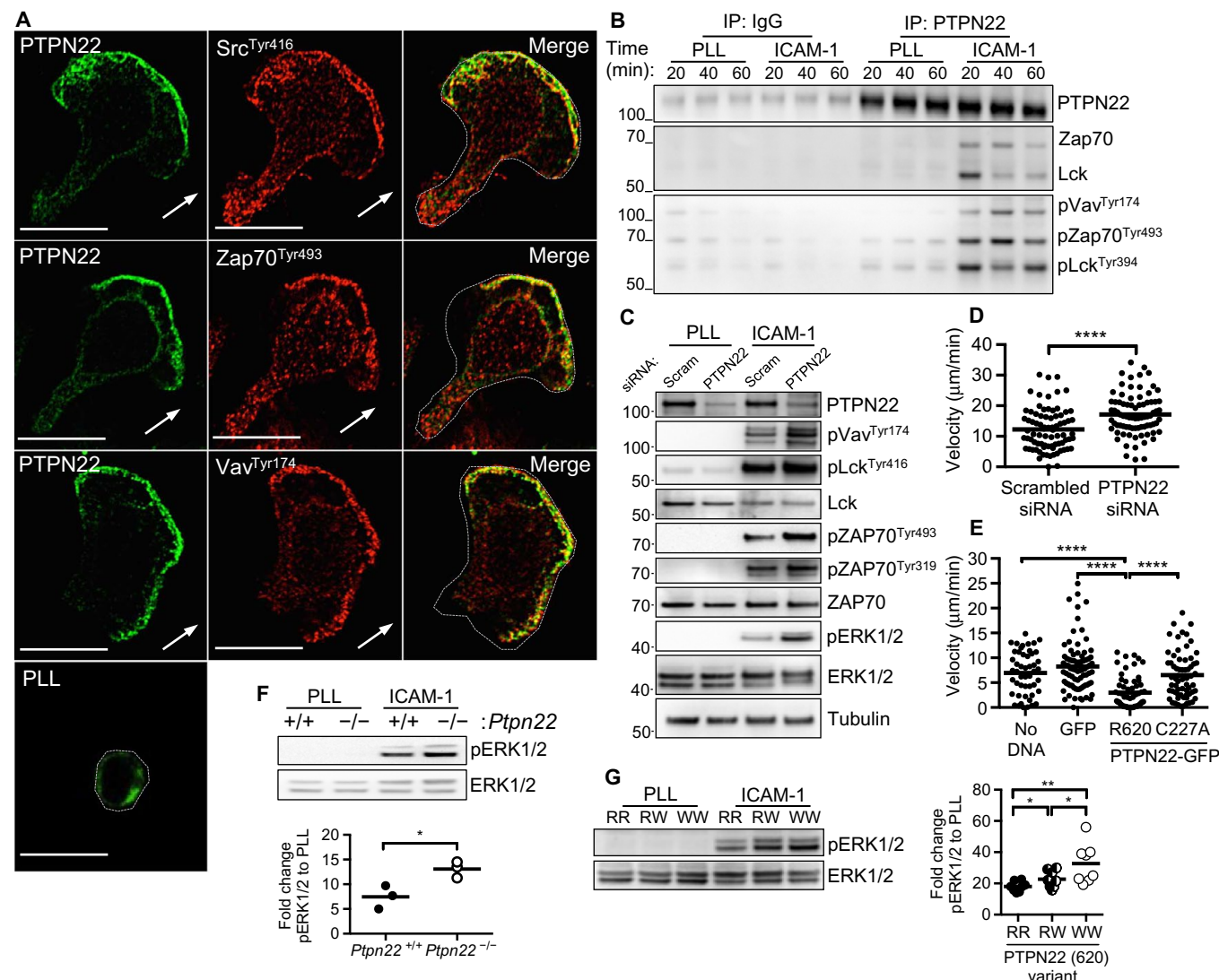


Fig. 1. PTPN22 is an inhibitor of LFA-1 signaling, colocalizing with its phosphorylated substrates at the leading edge of migrating T cells. (A) Primary human T cell blasts were layered onto glass slides coated with PLL or ICAM-1 for 20 min before being stained with mouse anti-PTPN22 antibody (green) and the indicated phosphospecific antibodies (red), and then imaged by confocal microscopy. The direction of migration is indicated by large white arrows. Scale bar, 10 μ m. Data represent the analysis of 30 to 40 cells from four independent experiments. (B) Human T cells layered onto PLL- or ICAM-1-coated plates for the indicated times were lysed, subjected to immunoprecipitation (IP) with mouse anti-PTPN22 antibody or control immunoglobulin G (IgG), and then analyzed by Western blotting with antibodies against the indicated proteins. Western blots are representative of five independent experiments. (C) T cells were transfected with scrambled (Scram) or PTPN22-specific (PTPN22) siRNAs and were then cultured for a further 48 hours before being plated onto PLL- or ICAM-1-coated plates. After 20 min, the adherent cells were harvested, lysed, and analyzed by Western blotting with antibodies against the indicated proteins. Western blots are representative of three experiments. (D) T cell blasts were transfected with scrambled or PTPN22-specific siRNAs and cultured for 24 hours before being plated onto ICAM-1-coated plates. The migration of single cells was tracked by time-lapse microscopy. Dot plots show pooled data from three experiments with the mean speeds \pm SD of 100 to 150 T cells transfected with the indicated siRNAs. **** P < 0.0001. (E) T cells were mock-transfected (no DNA) or were transfected with the indicated GFP expression vectors. After 24 hours, the velocity of the cells on ICAM-1 was quantified as described for (D). Data are means \pm SD derived from three pooled experiments analyzing a total of 50 to 90 cells. **** P < 0.0001; ns, not significant. (F) T cells isolated from the lymph nodes of *Ptpn22*^{+/+} or *Ptpn22*^{-/-} littermate mice were allowed to migrate for 20 min on PLL- or ICAM-1-coated plates. (Top) Lysates of adherent cells were analyzed by Western blotting with antibodies against the indicated proteins. Western blots are representative of three experiments. (Bottom) Fold changes in the abundance of pERK1/2 in the indicated cells plated on ICAM-1 relative to the abundance of pERK1/2 in cells plated on PLL were determined. Data are means \pm SD of three experiments. * P = 0.042. (G) Human T cell blasts were generated from genotyped donors expressing PTPN22-R620 (RR), PTPN22-R620W (RW), or PTPN22-W620 (WW) and allowed to migrate on PLL- or ICAM-1-coated plates for 20 min. (Left) Cells were lysed and analyzed by Western blotting with antibodies against the indicated proteins. (Bottom) Fold changes in the abundance of pERK1/2 in the indicated migrating cells relative to the abundance of pERK1/2 in nonmigrating cells were determined. Data are means \pm SD of eight experiments. Pairwise comparisons (two-tailed t test): RR versus RW, * P = 0.0337; RW versus WW, * P = 0.0144; RR versus WW, ** P = 0.0093.

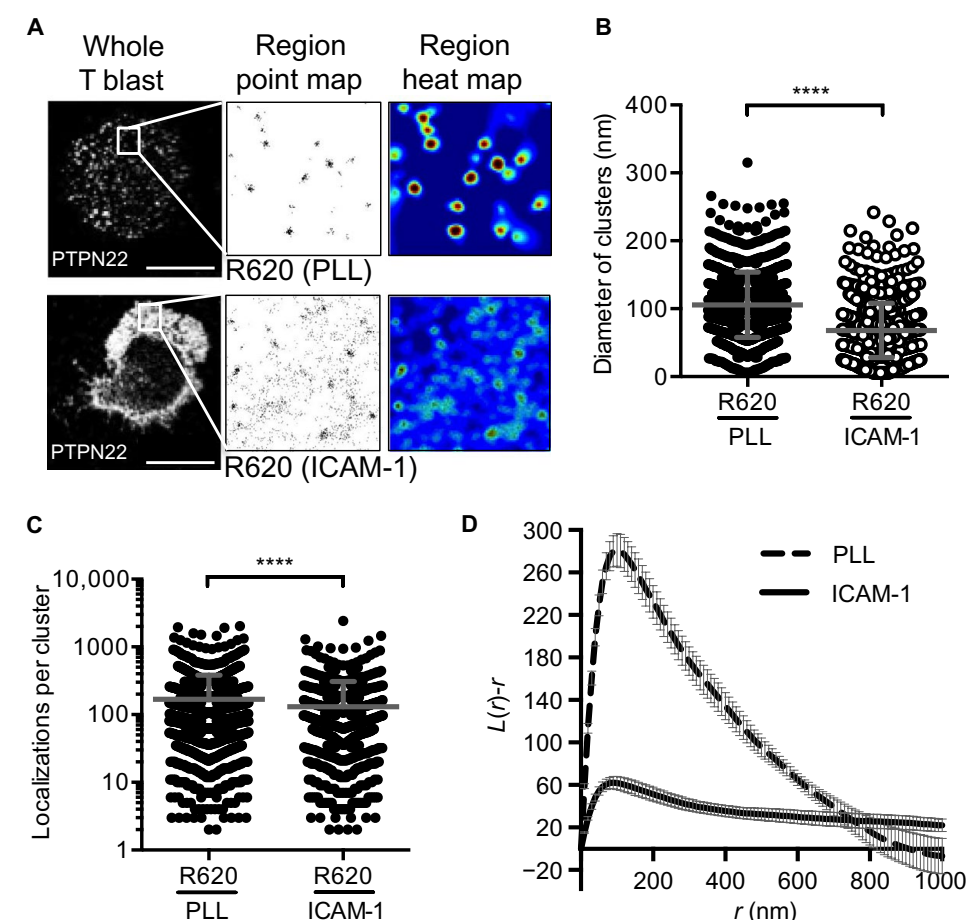


Fig. 2. PTPN22 exists in large clusters that disperse upon engagement of LFA-1. (A) Primary T cell blasts were generated from the peripheral blood of PTPN22-R620 homozygous donors and layered onto PLL- or ICAM-1-coated plates for 20 min before they were fixed, permeabilized, and stained with mouse anti-PTPN22 antibodies. Images were acquired with a Nikon N-STORM microscope, and molecule distributions were analyzed with cluster analysis algorithms. For each condition, N-STORM images are representative of PTPN22 molecule distributions at the whole-cell level and in 4- μ m² region maps (boxed), which were selected from the leading edge of the migrating T cell. Pointillist (Gaussian-fitted) and pseudocolored heat maps are representative of cluster data acquired after the processing of N-STORM image regions with the cluster analysis algorithm. Scale bars, 5 μ m for the PLL condition; 10 μ m for the ICAM-1 condition. Data are representative of three experiments analyzing 40 to 50 cells per experiment. (B and C) Cluster analysis of the images represented in (A) was used to define (B) the diameter of the PTPN22-R620-containing clusters and (C) the number of localizations of PTPN22-R620 per cluster for >900 clusters in nonmigrating cells (PLL) and migrating cells (ICAM-1). Data are pooled from three independent experiments analyzing 50 cells per experiment. **** P < 0.0001. (D) Ripley's K function curves (mean \pm SEM) were generated to quantify the degree of clustering of PTPN22-R620 in nonmigrating T cells (PLL, solid line) and migrating T cells (ICAM-1, dashed line). Data are representative of three experiments, analyzing between 30 and 50 cells per experiment.

C). Third, there was a marked increase in the number of PTPN22-R620 localizations at the leading edge (Fig. 3C, closed symbols). Thus, in response to the stimulation of LFA-1 by ICAM-1, PTPN22 molecules were dispersed from clusters and accumulated at the plasma membrane in closer proximity to LFA-1 signaling intermediates.

The clustering characteristics of the disease-associated W620 mutant PTPN22 were similar to those of the common R620 variant in nonmigrating cells (Fig. 3D, top; compare open versus closed symbols for cells plated on PLL in Fig. 3, A to C). In

contrast, migrating T cells expressing the PTPN22-W620 mutant had increased numbers and density of clusters (Fig. 3, A and B, open symbols), which were evident in the region point maps and heat maps (Fig. 3D, bottom). The amplitude of Ripley's K function also suggested that PTPN22-W620 was more clustered than PTPN22-R620 (Fig. 3E). Unexpectedly, the total number of molecules of PTPN22-W620 at the plasma membrane was substantially reduced compared to that of PTPN22-R620 after stimulation of LFA-1 (Fig. 3C, open versus closed symbols for ICAM-1). This finding was consistent

with the point maps, which showed reduced numbers of localizations outside of the clusters (Fig. 3D, bottom, and fig. S5A), which could not be explained by differences in protein abundances at the whole-cell level (fig. S5, B and C).

Using simulated data to model the consequences of varying the density of the nonclustered background of molecules that surround clusters, we found that both the linearity and the gradient of Ripley's K function depended on the number of nonclustered localizations (fig. S5, D and E). These simulations, together with the observed Ripley's K function data (Fig. 3E), indicated that differences between the clustering of PTPN22-R620 and PTPN22-W620 were not a result of changes in the clustering behavior of W620 but rather were a consequence of the lack of localization of PTPN22-W620 outside clusters, a finding that was consistent with the pointillist maps (fig. S5A). We surmised that declustered PTPN22-W620 molecules were not retained at the plasma membrane in migrating T cells to the same extent as were declustered PTPN22-R620 molecules. To explore the mechanism behind this difference in plasma membrane localization, we tested whether the P1 domain mutation in PTPN22-W620 compromised its binding to SH3 domain-containing protein partners, such as Csk, in response to integrin stimulation. Homozygous donor-derived PTPN22-R620- or PTPN22-W620-expressing T cells that migrated on ICAM-1 were lysed, subjected to immunoprecipitation with anti-Csk antibody, and analyzed by Western blotting with an anti-PTPN22 antibody. The results demonstrated that the association between Csk and PTPN22-W620 was reduced in migrating T cells compared to that between Csk and PTPN22-R620 (Fig. 3F). This suggests that upon stimulation of LFA-1, the retention of PTPN22 at the plasma membrane depends on the formation of a complex with Csk or other SH3 domain-containing proteins.

PTPN22 associates with the LFA-1 signaling complex and inhibits LFA-1 clustering

The LFA-1-dependent adhesion and migration of T cells are regulated by conformational changes in the extracellular domain of the α and β chains of the integrin, as well as the physical clustering of heterodimers at the plasma membrane (24–26). Furthermore, Lck and ZAP70 associate with the cytoplasmic tail of the β chain of ligand-bound LFA-1 (17, 27). Initial evidence for an association

between LFA-1 and its regulator, PTPN22, was derived from confocal images showing that LFA-1 and PTPN22 were colocalized at the leading edge (Fig. 4A). By TIRF microscopy, the colocalization of LFA-1 and PTPN22 was also observed at the interface with ICAM-1 at the leading edge (Fig. 4B), returning a Manders' colocalization coefficient (MCC) of 0.43 ± 0.14 . This association was also supported by co-immunoprecipitation experiments, in which LFA-1-PTPN22 interactions were observed to increase as a function of LFA-1 engagement (Fig. 4C). To address the mechanism for this association, we examined immunoprecipitates from the human leukemic Jurkat cell line and its Lck-deficient derivative JCaM1.6 (which both have comparable amounts of ZAP70 and PTPN22), and we found that PTPN22 did not appear to form complexes with LFA-1 in the absence of Lck (Fig. 4D and fig. S6). These data suggest that PTPN22 associates with the LFA-1 signaling complex in an Lck-dependent manner, where it interacts with substrates to regulate integrin signaling.

To examine the relationship between the regulation of LFA-1 signaling by PTPN22 and the function of LFA-1, we first investigated how the loss of PTPN22 function might affect LFA-1 clustering at the cell surface. Superresolution TIRF-dSTORM maps showed increased clustering of LFA-1 at the leading edge of migrating T cells expressing the PTPN22-W620 variant compared to that in cells expressing PTPN22-R620 (Fig. 5A), which was corroborated by Ripley's K function (Fig. 5B). Although there were no differences in the total number of LFA-1 localizations or in the number of clusters between cells expressing the two different PTPN22 variants (Fig. 5, C and D), the percentage of LFA-1 molecules participating in clusters were increased in T cells expressing the PTPN22-W620 variant (Fig. 5E). Thus, the loss of PTPN22 function was associated with increased LFA-1 clustering at the leading edge of migrating T cells.

Integrin-dependent adhesion is increased in T cells expressing the loss-of-function PTPN22-W620 variant

In light of these findings, we evaluated the functional consequences of enhanced LFA-1 clustering by directly comparing the adhe-

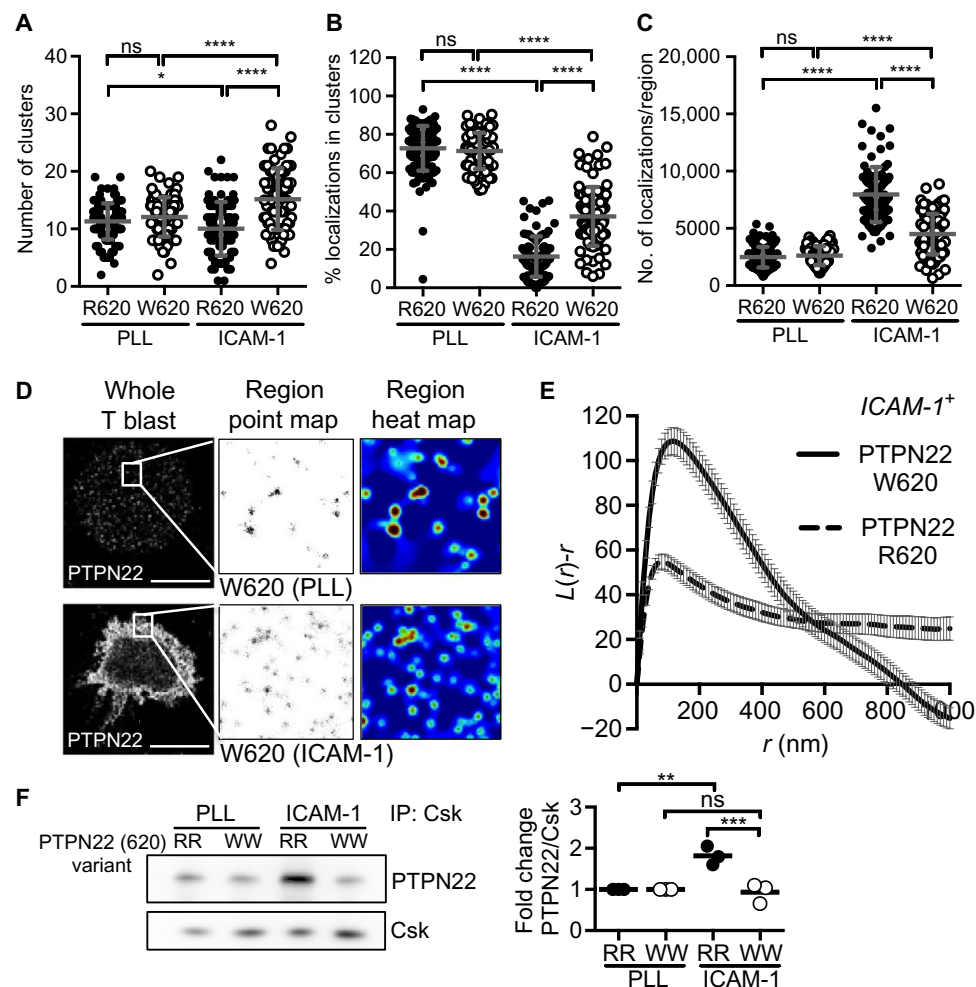


Fig. 3. Retention of PTPN22-W620 at the plasma membrane is impaired. (A to E) Primary T cell blasts were generated from the peripheral blood of PTPN22-R620 and PTPN22-W620 homozygous donors and layered onto PLL- or ICAM-1-coated plates for 20 min before they were fixed, permeabilized, and stained with mouse anti-PTPN22 antibodies. N-STORM images were acquired as described for Fig. 2, and cluster analysis was used to define (A) the number of PTPN22-R620 and PTPN22-W620 clusters per region ($n = 126$ regions), (B) the percentage of the indicated PTPN22 variant localizations in the clusters ($n = 126$ clusters), and (C) the number of the indicated PTPN22 variant localizations per region ($n = 126$ regions). Bars represent means \pm SD. * $P < 0.02$; **** $P < 0.0001$; ns, not significant. (D) Pointillist (Gaussian-fitted) and pseudocolored heat maps are representative of cluster data acquired after the processing of N-STORM image regions, as described for Fig. 2A. Scale bars, $5 \mu\text{m}$ for the PLL condition; $10 \mu\text{m}$ for the ICAM-1 condition. Data show the analysis of 50 cells per experiment and are representative of three experiments. (E) Ripley's K function curves (mean \pm SEM) were constructed to quantify the degree of clustering of PTPN22-R620 (dashed line) and PTPN22-W620 (solid line) in T cells migrating on ICAM-1. Data are representative of three independent experiments. (F) T cells expressing PTPN22-R620 (RR) or PTPN22-W620 (WW) derived from homozygous donors were plated on PLL- or ICAM-1-coated surfaces for 20 min. (Left) The cells were then lysed, subjected to immunoprecipitation with anti-Csk antibody, and analyzed by Western blotting with antibodies against the indicated proteins. Western blots are representative of three experiments. (Right) Quantification of the ratio of the abundance of PTPN22 to that of Csk, relative to that for cells plated on PLL. Data represent means of three independent experiments. Tukey's ordinary one-way analysis of variance (ANOVA) multiple comparisons test, **** $P < 0.0005$; ** $P < 0.005$; ns, not significant.

sion of T cells expressing either PTPN22-R620 or PTPN22-W620 under conditions of shear flow. T cells expressing the disease-associated PTPN22-W620 variant were more adherent to ICAM-1 than cells expressing the R620 variant (Fig. 6A). *Ptpn22*^{-/-} murine T cells phenocopied the disease-associated variant, being more adherent than wild-type T cells under shear flow (Fig. 6B) and

more adherent in de-attachment assays (Fig. 6C). Thus, a loss-of-function PTPN22 mutant that enhanced LFA-1 signaling increased LFA-1 clustering and cell adhesion. Together, our results suggest that in migrating T cells, PTPN22 disperses from large, plasma membrane-proximal clusters into smaller clusters that are capable of interacting with the LFA-1 signaling complex, where

inhibition of signaling leads to reduced integrin clustering and adhesion. If the localization of PTPN22 at the plasma membrane is compromised, regulation of integrin signals is uncoupled, and both integrin clustering and cell adhesion are enhanced.

DISCUSSION

Protein tyrosine phosphatases are now established as key regulators of integrin signaling (11, 12). The protein tyrosine phosphatase-PEST (PTP-PEST) family of phosphatases, which consists of PTPN12 and PTPN22, can be added to a growing list of inhibitors of integrin function, which includes DOK1 (RhoH, docking protein 1), calpain, and the ubiquitin ligase SHARPIN (SHANK-associated regulator of G protein signaling homology domain-interacting protein) (28–31). Single-molecule localization microscopy enabled us to image PTPN22 at the nanoscale level and to document that the plasma membrane-proximal de-clustering of PTPN22 is linked both temporally and spatially to its inhibitory function. This is in contradistinction to the opposing clustering behavior reported previously for kinase-associated signaling modules (32, 33), which enables digital signaling and increases signal transduction fidelity (34). Whether clustering in the steady state is unique to PTPN22 or is a common mechanism for sequestering phosphatases from their substrates will require further study.

The inhibitory functions of PTPN22 were confirmed by gene targeting in mouse and human T cells. We also found that a catalytically active PTPN22 was required to inhibit integrin-dependent cell motility. Experiments with PTPN22-W620-expressing T cells from homozygous donors indicated that the disease-associated variant was a loss-of-function mutant, at least in the context of LFA-1 signaling. The basis for this functional difference is underpinned in part by the impaired binding of the mutated P1 polyproline domain of PTPN22-W620 with SH3 domain-containing proteins, notably Csk. The spatiotemporal dynamics of PTPN22-Csk interactions and

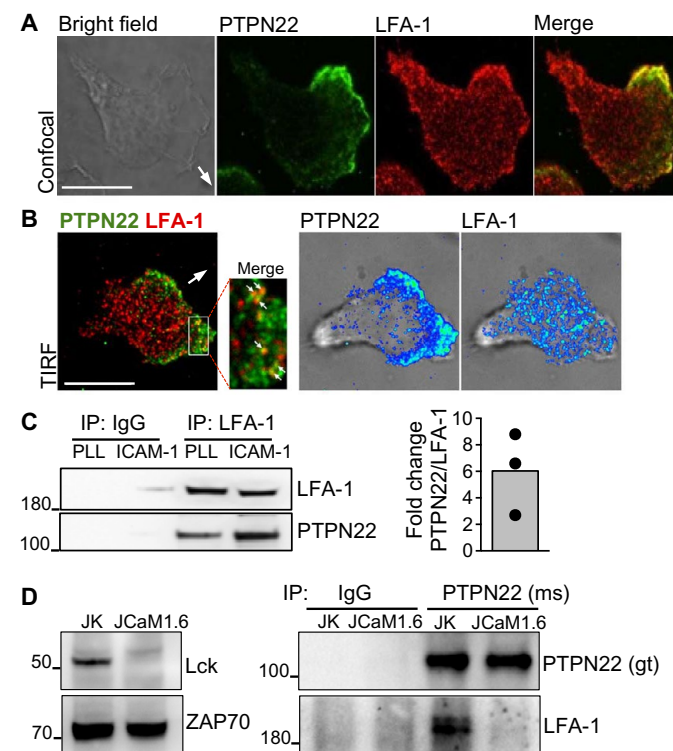


Fig. 4. PTPN22 colocalizes with LFA-1 at the leading edge of migrating T cells. (A and B) T cells migrating on an ICAM-1-coated surface were stained with antibodies specific for PTPN22 (green) and LFA-1 (red) and imaged by (A) confocal microscopy or (B) TIRF microscopy. The direction of migration is shown by white arrows. (B) (Left) The boxed region is shown under higher magnification, and the colocalization of PTPN22 and LFA-1 is indicated by small white arrows. (Right) Bright-field images with intensity scales for PTPN22 and LFA-1 in stained cells. Data are representative of regions selected from the leading edges of 30 to 40 cells from four independent experiments. (C) (Left) T cells that were plated on PLL- or ICAM-1-coated surfaces were lysed, subjected to immunoprecipitation with anti-LFA-1 antibody or control IgG, and analyzed by Western blotting with antibodies against the indicated proteins. Western blots are representative of three experiments. (Right) Quantification of the ratio of the abundance of PTPN22 to that of LFA-1 from T cells plated onto ICAM-1 relative to that for cells plated on PLL. Data are means derived from three independent experiments. (D) Jurkat cells (JK) and their Lck-deficient derivatives (JCaM1.6) were plated onto PLL-coated surfaces for 20 min before being lysed. (Left) Cell lysates were analyzed by Western blotting with antibodies against the indicated proteins. (Right) Cell lysates were subjected to immunoprecipitation with mouse anti-PTPN22 antibody or control IgG and analyzed by Western blotting with antibodies specific for the indicated proteins. Western blots are representative of two experiments (for the reciprocal experiment, see fig. S6). ms, mouse antibody; gt, goat antibody.

the effect of disrupting these associations on PTPN22 function are complex and may be signal-specific. For example, Vang *et al.* (35) demonstrated that dissociation of PTPN22 from Csk is a prerequisite for targeting the phosphatase to plasma membrane lipid raft domains, where it attenuates T cell receptor (TCR) signaling. PTPN22-W620 partitions into rafts more efficiently than does PTPN22-R620, whereas the forced dissociation of PTPN22 from Csk with a recombinant Csk-SH3 domain also reduces TCR signaling. These data support the gain-of-function hypothesis with respect to the PTPN22-W620

variant and TCR signaling, and suggest that the effect of the disease-associated mutant is context-dependent. Whereas uncoupling of the association between Csk and PTPN22-W620 seems a consistent feature relevant to TCR- and integrin-dependent signaling (36, 37), we cannot rule out the possibility that disrupting the interactions between PTPN22 and other SH3 domain-containing proteins could contribute to the signaling phenotypes reported. A comparative biochemical analysis of the PTPN22-R620 and PTPN22-W620 interactomes, using technologies that were reported for PAG (38), would provide a systematic and unbiased approach to address this issue.

We present a model depicting how PTPN22 inhibits LFA-1 signaling and how the PTPN22-W620 mutant enhances LFA-1 signaling and integrin-dependent adhesion (Fig. 7). According to this model, PTPN22 exists in large clusters in the steady state, where it is sequestered from its substrates. Active signals stimulate de-clustering, which is an event that we are now studying in the context of TCR and LFA-1 stimulation and one that targets clustered pools of both PTPN22 and Csk. Precisely how the clusters dis-aggregate is not known, but the process serves to deliver monomers of PTPN22 to the plasma membrane zone, enabling interactions with its binding partners. Lck is constitutively associated with the β subunit of LFA-1 (17) and is required for the recruitment of PTPN22 to the LFA-1 signaling complex.

In *PTPN22*^{-/-} cells, the LFA-1-stimulated phosphorylation of these intermediates goes unchecked, manifesting as the enhanced phosphorylation of signaling intermediates and augmented integrin-dependent signaling, cell motility, and adhesion. The outcome of expressing the PTPN22-W620 is the same, except that in this case, the total cellular amounts of the phosphatase are equivalent to those in PTPN22-R620-expressing T cells, but the W620 variant fails to bind to Csk (or possibly other SH3 domain-containing proteins). Instead, PTPN22-W620 is distributed throughout the rest of the cell rather than

Fig. 5. Expression of the PTPN22-W620 mutant enhances LFA-1 clustering at the leading edge of migrating T cells. (A) T cells from homozygous donors expressing PTPN22-R620 or PTPN22-W620 were layered onto PLL- or ICAM-1-coated plates for 20 min before being fixed and stained with anti-LFA-1 antibody. Images were acquired, and the molecular distributions were analyzed as described in Fig. 2. For each PTPN22 variant, representative images are shown for their cell surface LFA-1 molecule distributions. Single regions were used to generate pointillist and pseudo-colored cluster heat maps. Scale bar, 5 μ m. Data show representative images from an analysis of 70 to 80 cells per genotype and are representative of three experiments. (B) Ripley's K function curves (mean \pm SEM) were constructed to quantify the degree of clustering of surface LFA-1 in migrating T cells that expressed PTPN22-R620 (dashed line) or PTPN22-W620 (solid line). Data are representative of three independent experiments. (C to E) Cluster analysis of N-STORM images derived from PTPN22-R620- and PTPN22-W620-expressing T cells migrating on ICAM-1 was used to quantify (C) the number of LFA-1 localizations per region ($n = 83$ regions), (D) the number of LFA-1 clusters ($n = 83$ regions), and (E) the percentage of LFA-1 localizations in clusters ($n = 83$ clusters). Data are means \pm SD. **** $P < 0.0001$; ns, not significant.

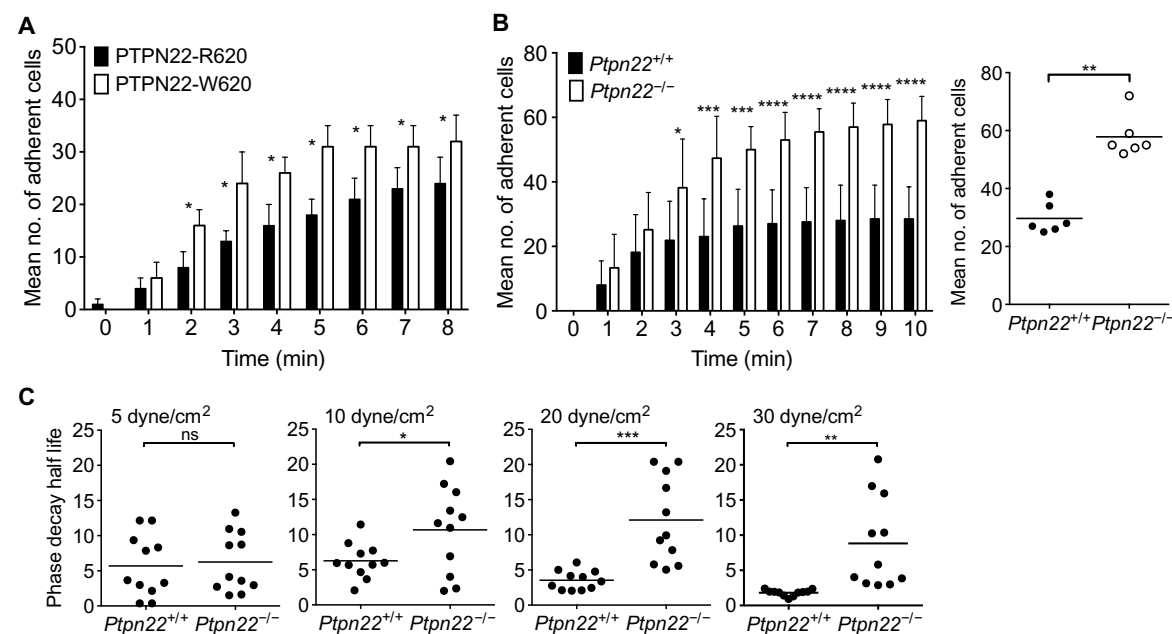
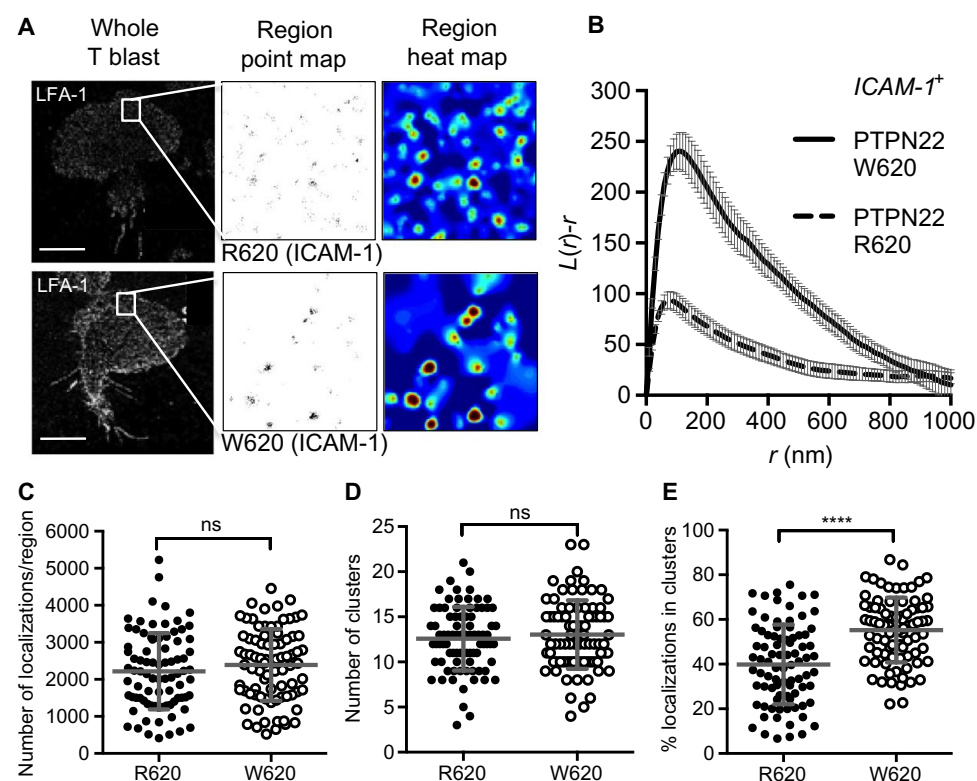


Fig. 6. T cells expressing loss-of-function PTPN22 mutants or those deficient in PTPN22 are more adherent under shear flow. (A) T cells expressing PTPN22-R620 or PTPN22-W620 derived from homozygous donors were flowed over glass slides coated with ICAM-1 (5 μ g/ml) at a shear flow rate of 0.5 dyne/cm² and imaged by time-lapse, wide-field microscopy. Cells adhering to ICAM-1-coated glass were counted every 1 min for a total of 8 min. Pooled data for cells of each genotype were derived from 12 independent experiments. * $P = 0.049$. (B) T cells were generated from the lymph nodes of *Ptpn22*^{+/+} and *Ptpn22*^{-/-} littermate mice, and their adherence under shear flow was quantified as described in (A). A representative experiment (left) and pooled data (right) show the mean number of adherent cells \pm SD after 10 min for cells of each genotype, based on six independent experiments. ** $P = 0.002$. (C) T cells from the indicated mice were prepared as described in (B) and allowed to adhere to glass slides coated with ICAM-1 (5 μ g/ml) for 10 min. Shear force was applied at the indicated flow rates, and time-lapse, wide-field movies were acquired. The numbers of adherent T cells were counted every 1 min for 10 min. Phase decay analysis was used to generate half-life values for cell attachment over time. Data represent 11 independent experiments. * $P = 0.0472$; ** $P = 0.005$; **** $P = 0.0008$; ns, not significant.

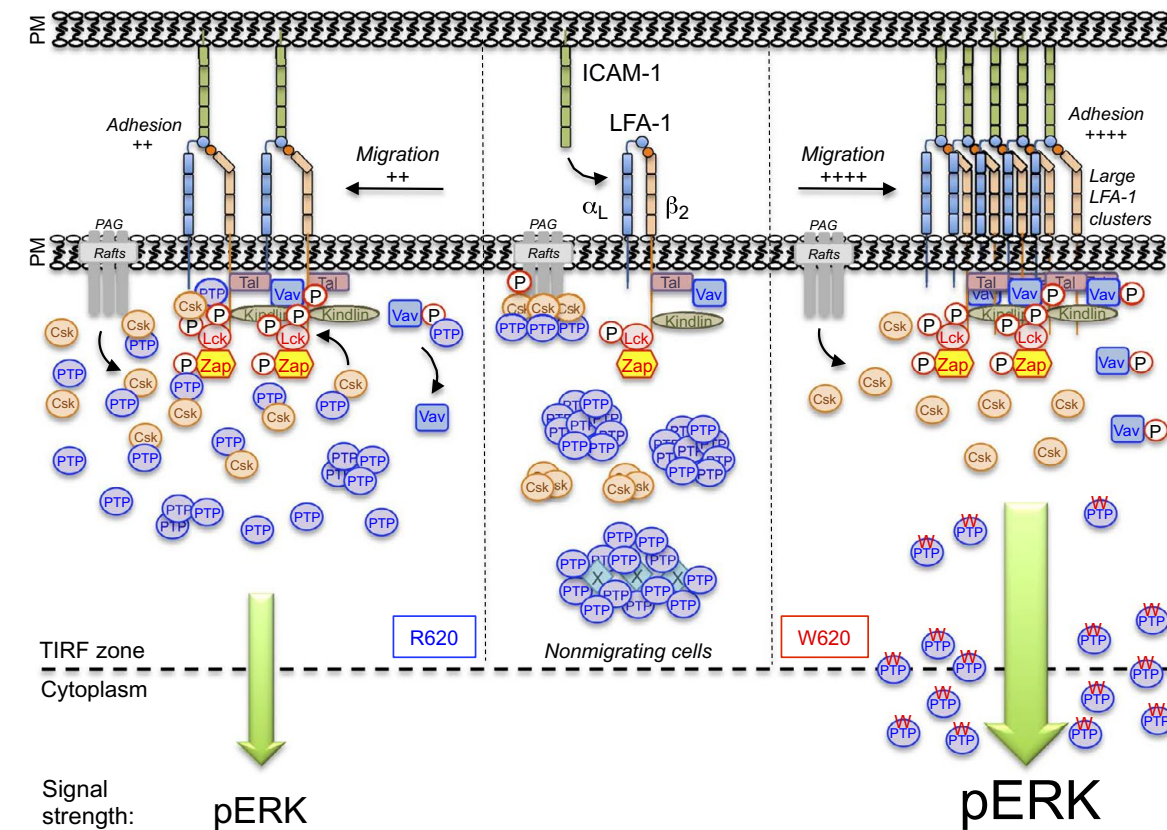


Fig. 7. Mechanistic model for the regulation of integrin signaling by PTPN22. The transition of LFA-1 from a low- or intermediate-affinity state (middle) to a high-affinity state (left) is characterized by the phosphorylation of Lck, ZAP70, and Vav, which are associated with the cytoplasmic tail of the β_2 subunit of LFA-1. Subsequently, spatiotemporal regulation of LFA-1 signals is mediated by the dispersal of PTPN22 and Csk from clusters, the disassociation of PTPN22 and Csk from PAG at the plasma membrane, and the increased association of PTPN22 with Csk through the P1 domain of PTPN22 and the SH3 domain of Csk. PTPN22-Csk complexes target their phosphorylated substrates in the LFA-1 signaling complex, which leads to the attenuation of LFA-1 signaling. Although the declustering of the loss-of-function PTPN22-W620 mutant is preserved, the binding of PTPN22-W620 to Csk is impaired (right). The mutant phosphatase is not retained at the plasma membrane, and in the absence of membrane-proximal binding partners, such as Csk, PTPN22-W620 diffuses away from the plasma membrane. As a consequence, LFA-1 signal intensity is augmented and sustained, further promoting LFA-1 clustering at the cell surface and increasing integrin-dependent adhesion (right). The spatiotemporal organization of PTPN22-R620 (PTP), PTPN22-W620 (PTP-W), Csk, talin (Tal), Lck, Vav1 (Vav), ZAP70 (Zap), and kindlin is illustrated. P denotes phosphorylation on tyrosine residues.

being retained near the LFA-1 signaling complex. Failure to attenuate LFA-1 signals is associated with much larger, denser clusters of LFA-1 at the cell surface, equipping the cell with domains of increased adhesiveness.

How might this increased cell adhesiveness translate to altered cell function in vivo? We suspect that the consequences of increased adhesion under shear flow conditions could perturb multiple phases of the homing of cells to lymph nodes and tissues, including the adhesion of cells on vascular endothelium coupled to transmigration into tissues, trafficking across high endothelial venules within lymphoid organs, and interactions between cells or with the surrounding extracellular matrix. Integrins have other functions in addition to mediating adhesion and migration because they promote interactions between T cells and antigen-presenting cells in ways that underpin the earliest steps in T cell activation and differentiation (9, 39), as well as downstream

effector responses, such as cytokine production and cytotoxic functions (4–6). We propose that aberrations in integrin function be included in the repertoire of mechanisms underpinning a predisposition to autoimmune disease in individuals carrying loss-of-function *PTPN22* mutations (40). Loss of immune tolerance, however, will depend on the balance of function between effector and regulatory T (T_{reg}) cells because our work has previously demonstrated that the increased adhesiveness of *Ptpn22*^{-/-} T_{reg} cells is associated with their greater potency (41).

MATERIALS AND METHODS

Antibodies and integrin ligands

Mouse monoclonal antibody and affinity-purified goat polyclonal antibody raised against human PTPN22 were purchased from R&D Systems. Antibodies specific for Vav1 (C-14), ZAP70 (1E7.2), Lck (3A5), and Csk (C20) were from Santa Cruz Biotechnology. Rabbit polyclonal antibodies against

pSrc (Tyr⁴¹⁶), pZAP70 (Tyr³¹⁹/Syk-Tyr³⁵²), pZAP70 (Tyr⁴⁹³/Syk-Tyr⁵²⁶), p44/42 MAPK (ERK1/2) (Thr²⁰²/Tyr²⁰⁴) (197G2), α - and β -tubulin, and β -actin were from Cell Signaling Technology; antibodies specific for pVav1 (Tyr¹⁷⁴) (EP5107), PAG (ab14989), and CD11a were from Abcam. The monoclonal anti-LFA-1 antibody mAb38 was a gift from N. Hogg (Francis Crick Institute, London, U.K.). Horseradish peroxidase (HRP)-conjugated sheep anti-mouse IgG (Amersham), goat anti-rabbit Ig-HRP (Dako), mouse monoclonal light chain-specific anti-goat IgG (Jackson Laboratory), goat anti-mouse IgG, goat anti-rabbit IgG, donkey anti-mouse IgG, donkey anti-rabbit IgG, and the IgG Zenon antibody labeling kit were from Life Technologies. Recombinant human ICAM-1/CD54 Fc chimera, recombinant murine ICAM-1/CD54 Fc chimera, recombinant VCAM-1, and fibronectin were obtained from R&D Systems.

Mice

Ptpn22^{-/-} mice were generated and genotyped as described previously (41). The line was rederived into the Biological Services Unit at King's College London and bred on a C57BL/6 background for 10 generations under specific pathogen-free conditions, in compliance with the Home Office regulations and local ethically approved guidelines. Sex- and age-matched *Ptpn22*^{+/+} and *Ptpn22*^{-/-} littermates were used in experiments.

Media, cell culture, and transfection

Human T cells were cultured in complete medium [Iscove's modified Dulbecco's medium (IMDM), 10% fetal bovine serum (FBS), penicillin, and streptomycin], whereas mouse T cells were cultured in Glutamax-RPMI, 10% FBS, 50 μM β-mercaptoethanol (β-ME), 100 μM sodium pyruvate, 20 mM Hepes, penicillin, and streptomycin. Glutamax-RPMI, 50 μM β-ME, 100 μM sodium pyruvate, 25 mM Hepes, penicillin, and streptomycin were used as cell migration medium. Human peripheral blood mononuclear cells (PBMCs) were isolated from whole blood with Lymphoprep (STEMCELL Technologies) and were stimulated with phytohemagglutinin (1 μg/ml, Thermo Fisher Scientific) in IMDM medium supplemented with 10% fetal calf serum, penicillin, and streptomycin (PAA) for the first 48 hours and with interleukin-2 (IL-2; 20 ng/ml, aldesleukin, Novartis) for up to 10 days. T cells were purified with a Pan T Cell Isolation kit (catalog no. 130-091-156, Miltenyi Biotec) to a purity of >97%, as determined by flow cytometry analysis. Donors belonging to TwinsUK (www.twinsuk.ac.uk) and selected on the basis of their rs2476601 genotype (*PTPN22* C1858T, corresponding to *PTPN22*-R620W protein) also provided PBMCs after informed consent. Transfection of primary human T cell blasts was performed with the Amaxa Nucleofector and Human T Cell Nucleofection Kit, program T-020 (Lonza). Plasmid DNA (2 μg) and siRNA pools (Invitrogen, Thermo Fisher Scientific) were used to transfect 1 × 10⁷ T cells. Mouse T cells were generated from splenic and lymph node cell suspensions, adjusted to a density of 3 × 10⁶ cells/ml, and cultured in complete medium. Cells were stimulated with concanavalin A (1 μg/ml, Sigma) for 48 hours, subjected to a Ficol gradient, and resuspended in complete medium supplemented with IL-2 (20 ng/ml) at a density of 2 × 10⁶ cells/ml. All adhesion and migration assays were performed with mouse T cells after they had been cultured for 4 to 5 days in IL-2. The human leukemic T cell line, Jurkat, and its Lck-deficient derivative JCaM1.6 were also used in experiments (42).

Generation of PTPN22-GFP constructs

A pEF5HA plasmid encoding PTPN22 (a gift from N. Bottini, La Jolla Institute for Allergy and Immunology, La Jolla, CA) was sequenced and used as a plasmid backbone for site-directed mutagenesis to generate a panel of PTPN22 mutants, and a 3' GFP fragment was introduced by subcloning. All constructs were verified by sequencing. Targeted mutations were introduced with the following specific primer pairs: R620W CCACCTTCCTGTATGGACACCTGAATCATTTA (forward) and TAAATGATTTCAGGTGTC-CATACAGGAAGTGG (reverse); C227A, TGTTCCCATATGCATTACGCCAGTGCTG-GCTGTGGAAGGACTGG (forward) and CCAAGTCTTCCACAGCCAGCACTGGCGT-GAATGCATATGGGAACA (reverse).

T cell stimulation and signaling with integrin ligands

Glass coverslips (32 mm, VWR International) were coated in six-well sterile plates with the integrin ligands ICAM-1-Fc (3 μg/ml, unless indicated otherwise), VCAM-1-Fc (3 μg/ml), or fibronectin (10 μg/ml) or with PLL (Sigma) overnight at 4°C, washed three times with phosphate-buffered saline (PBS), and blocked for 1 hour at room temperature with 2% bovine serum albumin (BSA) in PBS. T cell blasts were rested in migration medium for 30 min and then added to coverslips (at 3 × 10⁶ cells per coverslip) and incubated for 20 min at 37°C. Unbound cells were then aspirated, and 1 ml of lysis buffer was added to the coverslips (1 × 6-well plate, 2 × 10⁷ cells per well) before being lysed on ice for 20 min. Lysates were cleared by centrifugation and diluted in sample buffer for Western blotting or immunoprecipitation experiments.

Western blotting and immunoprecipitations

Cells were lysed directly in 2× SDS-polyacrylamide gel electrophoresis (SDS-PAGE) sample buffer or in lysis buffer containing 1% Triton X-100 (Sigma) with phosphatase and protease inhibitors (Roche). Proteins were separated by SDS-PAGE and transferred to Immobilon-P polyvinylidene difluoride membranes by standard Western blotting techniques. After incubation with primary and secondary antibodies, reactive bands on the blots were visualized by Super-Signal chemiluminescent reaction (Pierce Biotechnology) in a ChemiDoc Station (Bio-Rad). For immunoprecipitations, 1 to 2 μg of control or specific antibody were added to cell lysates overnight at 4°C, which was followed by the addition of 20 μl of magnetic beads (Millipore) and incubation for 1 hour at 4°C. The beads were washed three times in lysis buffer before being eluted with 20 μl

of boiling 2× SDS-PAGE sample buffer. Cell lysates and immunoprecipitates were used immediately or were stored at -80°C until needed for analysis.

Immunofluorescence staining and microscopy

Coverslips, glass-bottomed dishes (Mat-Tek), or eight-well glass-bottomed microscopy chambers (ibidi) were coated overnight at 4°C with human recombinant ICAM-1-Fc (3 μg/ml) or 0.01% PLL, washed three times in Hanks' balanced salt solution, and blocked in 5% BSA for 1 hour. T cells were re-suspended at 2.5 × 10⁵ cells/ml in migration medium that had been equilibrated overnight at 37°C in 5% CO₂ and added to glass coated with ICAM-1-Fc. After 20 min of migration, the cells were pH shift-fixed [that is, they were treated for 5 min with 3% paraformaldehyde (PFA)-80 mM Pipes dipotassium salt (pH 6.8), supplemented with 2 mM Mg²⁺ and 5 mM EGTA, which was followed by treatment for 10 min with 3% PFA and 100 mM Borax (pH 11)] and then permeabilized with 0.1% Triton X-100 for 5 min at 4°C. Autofluorescence was quenched by treating the samples with NaBH₄ (1 mg/ml) for 15 min. The chambers were blocked with 10% goat serum for 1 hour and then incubated with primary antibody overnight and an appropriate secondary antibody for 20 min at room temperature. Confocal microscopy was performed with a Zeiss LSM 700 Axio Imager M2 system at ×63 magnification (Plan-Apochromat 63×/1.40 Oil M27, Zeiss; zoom, 4; 512 × 512 pixel scan). TIRF images were obtained with a Zeiss observer Z1 (inverted) microscope equipped with a TIRF slider [Plan-Apochromat 100×/1.40 Oil DIC (UV) VIS-IR, Zeiss]. Images were collected, processed, and analyzed with SlideBook 5.5 (3i) or ImageJ software. Colocalization of signaling proteins was determined according to the method of Dunn *et al.* (43). Briefly, TIRF images were processed with the automatic method of local background subtraction by median filtering and finally by small-value subtraction with SlideBook6 software. Four regions (1.6 μm × 1.6 μm) were chosen in the front lamella of the cell. Subsequently, MCC was calculated with the inbuilt SlideBook6 function. Results from five regions were averaged per cell in four different experiments and analyzed with Prism 6.0 software (GraphPad).

Direct stochastic optical reconstruction microscopy

dSTORM imaging was performed on a Nikon N-STORM microscope with a 100× 1.49 numerical aperture oil immersion TIRF objective. Cells were imaged under TIRF

illumination with a 647-nm laser with photoactivation at 405 nm in oxygen-scavenging buffer [including glucose oxidase (50 μg/ml), HRP (25 μg/ml), and 75 mM cysteamine in base buffer (pH 8.0)]. Fluorescence was collected on an Andor iXon EM-CCD camera. Acquisition time was between 5 and 15 min, with an integration time of 10 ms. Molecular coordinates were calculated with Nikon NIS N-STORM software using a photon threshold of 3000 per point spread function.

Cluster analysis

The output from the NIS N-STORM software was in the form of pointillist *x-y* coordinates of the localized fluorophores. Data were divided into nonoverlapping 2 μm × 2 μm square regions, avoiding cell boundaries. Ripley's K function can be used to quantify the level and size scale of molecular clustering, and the use of this function has previously been demonstrated in experiments with T cells (44–46). The K function was calculated for each region with the Excel plug-in SpPack (47) with the following equation:

$$K(r) = \frac{A}{n^2} \sum_{i=1}^n \sum_{j=1}^n \delta_{ij}$$

where $\delta_{ij} = 1$ if the distance between molecules *i* and *j* is less than *r*; otherwise, $\delta_{ij} = 0$. Therefore, δ_{ij} represents the drawing of concentric circles of radius *r* around each point, *i*, and counting how many other points, *j*, are encircled. As defined, the *K(r)* value scales linearly with the circle area for increasing *r* and is therefore converted into the *L* function with the following equation:

$$L(r) = \sqrt{K(r)/\pi}$$

This function is represented by a plot of *L(r)-r* versus *r*. In the case of a completely spatially random (CSR) distribution of molecules, *L(r)-r = 0* for all *r*. If *L(r)-r* is positive, this represents clustering on a particular spatial scale, *r*. A negative *L(r)-r* value represents a more regular distribution than that of CSR (negative clustering). Edge effects were corrected by means of a toroidal wrap. Confidence intervals (95%) were calculated by simulating 100 CSR distributions with the same total molecular density as that of the experimental data. To test the effect of reducing the density of monomers (that is, the CSR background) on the Ripley's K function curves, we analyzed simulated data. A 3 μm × 3 μm region was simulated with a single Gaussian profile cluster at its center (SD = 100 nm, 100 points), which was then overlaid with a CSR background. We then varied the

density of the CSR overlay and analyzed the resulting Ripley's K function curves. In the presence of zero background, the curve decays linearly to negative infinity at increasing *r*; however, in the presence of increasing background, the curve asymptotically approaches zero (as is the case for a pure CSR distribution). To generate the pseudocolored cluster maps, the degree of clustering of each molecule was calculated with Getis' variant of Ripley's K function (48). This is simply the *L(r)* value omitting averaging over all molecules in the region (*j*). Therefore, for each molecule, *i*, this value is given by the following equation:

$$L(r)_i = \sqrt{\frac{A}{n} \sum_{j=1}^n \delta_{ij}/\pi}$$

Molecules at the edge of the region of interest had their *L(r)* value corrected with a buffer region of width *r*. To generate the cluster maps, the *L(r)* values were interpolated onto a 5-nm resolution grid with MATLAB software, and the *L(r)* color surface was pseudocolored. To extract cluster statistics, the map was thresholded at a value of *L(r) = 200*, with areas above this value considered to be clusters. Clusters were separated with an 8-connectivity rule that enabled us to extract the number of clusters, cluster sizes, number of molecules per cluster, and other parameters.

Flow cytometry

T cell blasts were stained in cold flow cytometry (fluorescence-activated cell sorting) buffer (0.5% BSA and 0.01% sodium azide in PBS) with antibodies and live/dead discrimination, washed, fixed with 2% PFA, and analyzed with a FACSCalibur flow cytometer. Data analysis was performed with FlowJo software (Tree Star Inc.).

Time-lapse microscopy

To monitor cell attachment under shear flow, glass-bottomed flow chambers (μ-Slide VI^{0.4}, ibidi) were coated with ICAM-1-Fc (5 μg/ml), and T cell blasts (1 × 10⁶ cells/ml) were flowed over the glass at 0.5 dyne/cm² for 8 to 10 min in migration medium. Wide-field, time-lapse movies were acquired in 10 areas per slide. Cell numbers were counted over time, and the data were presented as means ± SD. To monitor cell detachment under shear flow, T cells isolated from *Ptpn22*^{+/+} and *Ptpn22*^{-/-} mice (5 × 10⁶ cells/ml in migration medium) were allowed to adhere to glass-bottomed flow chambers (μ-Slide VI^{0.1}, ibidi) coated with ICAM-1-Fc (5 μg/ml) for 10 min, and then migration medium (incubator-equilibrated

overnight) was applied at shear flow rates from 5 to 30 dynes/cm². Wide-field, time-lapse images were acquired for 10 min, and cell counts were accrued every 1 min. Data were plotted exponentially reflecting loss of cell numbers over time, and the phase decay half-life was calculated with Prism 6.0 software (GraphPad). Values represent the rate at which the T cells detached from the glass over time; lower values indicate increased detachment.

Statistical analysis

All statistical analyses were performed with Prism 6.0 software (GraphPad). Distributions of data points and their variance were determined, and parametric or non-parametric tests were applied, as appropriate. Comparisons between two groups were evaluated with a Mann-Whitney *U* test; unpaired Student's *t* tests were used for normally distributed data. Comparison of three or more independent conditions was determined with the rank-based non-parametric Kruskal-Wallis *H* test or with Tukey's ordinary one-way ANOVA multiple comparisons test for normally distributed data. For comparison of cell motility, cell adhesion, and clustering data between groups, unpaired two-tailed *t* tests were used. Student's *t* tests were also applied to compare densitometric measurements between independent Western blotting experiments. Differences were considered to be statistically significantly different when *P* < 0.05.

REFERENCES AND NOTES

- R. O. Hynes, *Cell* **110**, 673–687 (2002).
- M. S. Johnson, N. Lu, K. Denessiouk, J. Heino, D. Gullberg, *Biochim. Biophys. Acta* **1788**, 779–789 (2009).
- N. Hogg, I. Patzak, F. Willenbrock, *Nat. Rev. Immunol.* **11**, 416–426 (2011).
- V. S. Ramgolam *et al.*, *PLOS ONE* **5**, e14450 (2010).
- O. D. Perez *et al.*, *Nat. Immunol.* **4**, 1083–1092 (2003).
- Y. Kaufmann, P. Golstein, M. Pierres, T. A. Springer, Z. Eshhar, *Nature* **300**, 357–360 (1982).
- A. Huttenlocher, A. R. Horwitz, *Cold Spring Harb. Perspect. Biol.* **3**, a005074 (2011).
- T. Kinashi, *Nat. Rev. Immunol.* **5**, 546–559 (2005).
- M. L. Dustin, S. K. Bromley, Z. Kan, D. A. Peterson, E. R. Unanue, *Proc. Natl. Acad. Sci. U.S.A.* **94**, 3909–3913 (1997).
- N. K. Verma *et al.*, *J. Cell. Physiol.* **226**, 1489–1498 (2011).
- K. Burridge, S. K. Sastry, J. L. Sallee, *J. Biol. Chem.* **281**, 15593–15596 (2006).
- J. L. Sallee, E. S. Wittchen, K. Burridge, *J. Biol. Chem.* **281**, 16189–16192 (2006).
- J. Wu *et al.*, *J. Biol. Chem.* **281**, 11002–11010 (2006).

14. G. L. Burn, L. Svensson, C. Sanchez-Blanco, M. Saini, A. P. Cope, *FEBS Lett.* **585**, 3689–3698 (2011).
15. T. Vang *et al.*, *Nat. Genet.* **37**, 1317–1319 (2005).
16. J. Zikherman *et al.*, *J. Immunol.* **182**, 4093–4106 (2009).
17. R. Evans, A. C. Lellouch, L. Svensson, A. McDowall, N. Hogg, *Blood* **117**, 3331–3342 (2011).
18. S. Fagerholm, T. J. Hilden, C. G. Gahmberg, *Eur. J. Immunol.* **32**, 1670–1678 (2002).
19. M. C. Mendoza *et al.*, *Mol. Cell* **41**, 661–671 (2011).
20. M. C. Mendoza, M. Vilela, J. E. Juarez, J. Blenis, G. Danuser, *Sci. Signal.* **8**, ra47 (2015).
21. V. J. Fincham, M. James, M. C. Frame, S. J. Winder, *EMBO J.* **19**, 2911–2923 (2000).
22. T. Brdička *et al.*, *J. Exp. Med.* **191**, 1591–1604 (2000).
23. M. Hrdinka, V. Horejsi, *Oncogene* **33**, 4881–4892 (2014).
24. B.-H. Luo, C. V. Carman, T. A. Springer, *Ann. Rev. Immunol.* **25**, 619–647 (2007).
25. T. S. van Zanten *et al.*, *Proc. Natl. Acad. Sci. U.S.A.* **106**, 18557–18562 (2009).
26. M. Kim, C. V. Carman, W. Yang, A. Salas, T. A. Springer, *J. Cell Biol.* **167**, 1241–1253 (2004).
27. E. G. Arias-Salgado *et al.*, *Proc. Natl. Acad. Sci. U.S.A.* **100**, 13298–13302 (2003).
28. A. J. Garton, A. J. Flint, N. K. Tonks, *Mol. Cell Biol.* **16**, 6408–6418 (1996).
29. L. K. Cherry, X. Li, P. Schwab, B. Lim, L. B. Klickstein, *Nat. Immunol.* **5**, 961–967 (2004).
30. M. Bolomini-Vittori *et al.*, *Nat. Immunol.* **10**, 185–194 (2009).
31. N. J. Anthis *et al.*, *J. Biol. Chem.* **284**, 36700–36710 (2009).
32. Y. Neve-Oz, Y. Razvag, J. Sajman, E. Sherman, *Biochim. Biophys. Acta* **1853**, 810–821 (2015).
33. J. Rossy, D. M. Owen, D. J. Williamson, Z. Yang, K. Gaus, *Nat. Immunol.* **14**, 82–89 (2013).
34. E. Roob III, N. Trendel, P. Rein Ten Wolde, A. Mugler, *Biophys. J.* **110**, 1661–1669 (2016).
35. T. Vang *et al.*, *Nat. Chem. Biol.* **8**, 437–446 (2012).
36. N. Bottini *et al.*, *Nat. Genet.* **36**, 337–338 (2004).
37. A. B. Begovich *et al.*, *Am. J. Hum. Genet.* **75**, 330–337 (2004).
38. K. Reginald, *et al.*, *J. Immunol.* **195**, 5472–5481 (2015).
39. M. L. Dustin, A. K. Chakraborty, A. S. Shaw, *Cold Spring Harb. Perspect. Biol.* **2**, a002311 (2010).
40. A. Veillette, I. Rhee, C. M. Souza, D. Davidson, *Immunol. Rev.* **228**, 312–324 (2009).
41. R. J. Brownlie *et al.*, *Sci. Signal.* **5**, ra87 (2012).
42. D. B. Straus, A. Weiss, *Cell* **70**, 585–593 (1992).
43. K. W. Dunn, M. M. Kamocka, J. H. McDonald, *Am. J. Physiol. Cell Physiol.* **300**, C723–C742 (2011).
44. D. J. Williamson *et al.*, *Nat. Immunol.* **12**, 655–662 (2011).
45. B. D. Ripley, *J. R. Stat. Soc. Ser. B* **41**, 368–374 (1979).
46. B. D. Ripley, *J. R. Stat. Soc. Ser. B* **39**, 172–212 (1977).
47. G. L. W. Perry, *Environ. Model Softw.* **19**, 559–569 (2004).
48. D. M. Owen *et al.*, *J. Biophotonics* **3**, 446–454 (2010).

ACKNOWLEDGMENTS

We thank N. Hogg for providing anti-LFA-1 antibodies, N. Bottini for supplying PTPN22 cDNA constructs, N. Hogg and S. Fagerholm for helpful comments on the manuscript, and T. Prevost for advice on all statistical analysis.

Funding: This research was supported by Arthritis Research UK grants 16409 (to R.Z.), 19652 (to A.P.C., L.M.S., and R.Z.), 20525 (to G.H.C., A.P.C., L.M.S., and R.Z.), and 20848 (to V.L.M.); a Royal Society collaborative travel grant (to L.M.S. and A.P.C.); Wellcome Trust project grant 086054 (to R.J.B., A.P.C., and R.Z.); Wellcome Trust Investigator Award 096669 (to R.Z.); a Strategic Award from the Wellcome Trust for the Centre for Immunity, Infection and Evolution (095831 to R.Z.); Swedish Medical Council awards K2010-80P-21592-01-4 and K2010-80X-215917-01-4; Stiftelsen Olle Engquist Byggmästare, I&A Lundberg forskningsstiftelse, Gyllenstiernska Krappers-stiftelsen, Gustav V 80 jubileum fond, Nanna Svartz, and Crafoord awards (to L.M.S.); Anna-Greta Crafoords postdoctoral fellowship (to K.P.); a European Research Council starter grant (337187 to D.M.O.); and a Marie Curie Career Integration Grant (334303 to D.M.O.). This work was also supported by infrastructure funded by the National Institute for Health Research Biomedical Research Centre at Guy's and St. Thomas' NHS

Foundation Trust and King's College London (reference: guysbrc-2012-17) and by the Nikon Imaging Centre at King's College London.

Author contributions: G.L.B., G.H.C., K.P., and M.S. performed most of the experiments and analyzed the data; M.S., J.G., S.M., M.Y., G.A., and N.P. contributed to the imaging experiments and their analysis, including simulations; V.L.M. contributed to the analysis of cell adhesion under flow; C.S.-B., H.P., F.C., and R.J.B. contributed to the execution and analysis of mouse experiments; T.J.V. identified and provided PTPN22-genotyped donors; G.L.B., G.H.C., R.Z., D.M.O., L.M.S., and A.P.C. designed the experiments and analyzed the data; and G.L.B., G.H.C., L.M.S., and A.P.C. wrote the manuscript. **Competing interests:** The authors declare that they have no competing interests.

Submitted 8 January 2016
Accepted 16 September 2016
Published 4 October 2016
10.1126/scisignal.aaf2195

Citation: G. L. Burn, G. H. Cornish, K. Potrzebowska, M. Samuelsson, J. Griffié, S. Minoughan, M. Yates, G. Ashdown, N. Pernodet, V. L. Morrison, C. Sanchez-Blanco, H. Purvis, F. Clarke, R. J. Brownlie, T. J. Vyse, R. Zamoyska, D. M. Owen, L. M. Svensson, A. P. Cope, Superresolution imaging of the cytoplasmic phosphatase PTPN22 links integrin-mediated T cell adhesion with autoimmunity. *Sci. Signal.* **9**, ra99 (2016).

SUPPLEMENTARY MATERIALS

www.sciencesignaling.org/cgi/content/full/9/448/ra99/DC1

Fig. S1. PTPN22 and its phosphorylated substrates localize to the leading edge of migrating T cells.

Fig. S2. TIRF microscopy confirms the colocalization of PTPN22 with its phosphorylated substrates.

Fig. S3. Engagement of integrin leads to the phosphorylation of PTPN22 substrates in migrating T cells.

Fig. S4. Csk declusters upon engagement of LFA-1 and associates with PTPN22 in migrating T cells.

Fig. S5. Analysis of cluster characteristics and the abundances of PTPN22-R620 and PTPN22-W620 in migrating T cells.

Fig. S6. PTPN22 associates with LFA-1 in an Lck-dependent manner.

REPORT

BACTERIAL DIVISION

GTPase activity-coupled treadmilling of the bacterial tubulin FtsZ organizes septal cell wall synthesis

Xinxing Yang,¹ Zhixin Lyu,^{1*} Amanda Miguel,^{2*} Ryan McQuillen,¹ Kerwyn Casey Huang,^{2,3†} Jie Xiao^{1†}

The bacterial tubulin FtsZ is the central component of the cell division machinery, coordinating an ensemble of proteins involved in septal cell wall synthesis to ensure successful constriction. How cells achieve this coordination is unknown. We found that in *Escherichia coli* cells, FtsZ exhibits dynamic treadmilling predominantly determined by its guanosine triphosphatase activity. The treadmilling dynamics direct the processive movement of the septal cell wall synthesis machinery but do not limit the rate of septal synthesis. In FtsZ mutants with severely reduced treadmilling, the spatial distribution of septal synthesis and the molecular composition and ultrastructure of the septal cell wall were substantially altered. Thus, FtsZ treadmilling provides a mechanism for achieving uniform septal cell wall synthesis to enable correct polar morphology.

The tubulin homolog FtsZ (1) is the central component of the cell division machinery in nearly all walled bacterial species (2). During division, FtsZ polymerizes on the cytoplasmic face of the inner membrane to form a ring-like structure, the Z-ring (3), and recruits more than 30 proteins to the division site (4). Many of these proteins are involved in septal synthesis of the peptidoglycan (PG) cell wall (4). The guanosine triphosphatase (GTPase) activity of FtsZ is highly conserved (5, 6), and the binding and hydrolysis of GTP underlie the dynamic assembly and disassembly of FtsZ (7, 8). Although several proposed mechanisms revolve around GTPase activity-dependent constriction force generation by the Z-ring (9), in *E. coli* the GTPase activity of FtsZ appears nonessential for cell division and does not dictate the cell constriction rate (10, 11). Thus, the biological function of FtsZ's GTPase activity in bacterial cell division remains elusive.

To understand the role of GTPase activity in division, we characterized Z-ring dynamics in live *E. coli* BW25113 cells by using total internal reflection fluorescence (TIRF) microscopy to monitor the fluorescence of an FtsZ-GFP fusion protein (fig. S1) (12).

FtsZ-GFP was expressed in the presence of endogenous, unlabeled wild-type FtsZ at $46 \pm 4.3\%$ of total cellular FtsZ concentration (mean \pm SD, $n = 3$; fig. S2). The integrated TIRF intensity of the Z-ring exhibited large, approximately periodic fluctuations (Fig. 1, A and B; fig. S3; and movies S1 and S2). We observed similar behaviors with other fluorescent fusions (figs. S4 and S5 and movie S3) (13, 14) but not with fixed cells (fig. S4G) or fluorescent beads (fig. S4H), suggesting periodic assembly and disassembly cycles of FtsZ polymers in the Z-ring.

The power spectral densities (PSDs) of individual cells revealed clear peaks in the intensity fluctuations (Fig. 1C). The mean PSD curve of all cells showed a lognormal-like distribution (Fig. 1D, green curve) with a peak period of 115 ± 10 s (mean \pm SEM; table S1) after subtracting the contribution of Z-ring dynamics due to stochastic subunit exchange (Fig. 1D, red curve) (7, 8, 12). We calibrated the FtsZ-GFP intensity with cellular expression levels of FtsZ and FtsZ-GFP (figs. S1 and S6) (12), to estimate that 683 ± 439 FtsZ molecules (mean \pm SD; Fig. 1E) assembled in each TIRF intensity peak (Fig. 1B); these likely correspond to groups of smaller FtsZ clusters previously described in superresolution imaging studies (15–17). The assembly and disassembly rates of these FtsZ polymers (Fig. 1B) were essentially the same (Fig. 1F), indicating a dynamic steady state of polymer assembly and disassembly.

Treating cells with specific inhibitors (12) of proteins involved in cell wall synthesis did not affect the periodic FtsZ fluctuations (Fig.

1G and table S2). Mutants lacking one of the proteins that regulates the Z-ring (SlmA, SulA, MinC, ClpX, and ClpP) or stabilizes it (ZapA, ZapB, ZapC, ZapD, and MatP) (12) also displayed wild-type Z-ring behavior (Fig. 1, H and I; fig. S7; and table S3). Thus, Z-ring dynamics are likely due to FtsZ's intrinsic polymerization properties, which are related to its GTPase activity.

To examine whether GTPase activity influences the periodic assembly and disassembly dynamics, we constructed strains each with a single point mutation at the chromosomal *ftsZ* locus (12). The catalytic GTP turnover rate constants (k_{cat}) of these mutant proteins in vitro (12, 18, 19) ranged from 14% to 71% of the wild-type k_{cat} value (fig. S8A and table S1) (12). Because of the high cellular concentration of GTP (~ 5 mM) (20), the in vivo GTPase activity of these mutants should mainly represent their maximal GTP hydrolysis rate (reflected in k_{cat}). Z-ring dynamics were significantly reduced in mutants with lower GTPase activity (Fig. 1, J and K, and table S1). In addition, the subunit exchange rate constants (k_{ex}) of these mutants, extracted from PSD curves or obtained from fluorescence recovery after photobleaching (FRAP) (fig. S8, C to E), decreased with k_{cat} (12) in a manner consistent with coupling to GTP hydrolysis. We observed the same trend using GFP-ZapA (fig. S4F). The fluctuation frequency and k_{ex} of each mutant were highly correlated with k_{cat} (Fig. 1, K and L) and with each other (Fig. 1M). Clearly, the periodic Z-ring dynamics are strongly coupled to GTP hydrolysis.

In some kymographs of cells lacking well-defined midcell Z-rings, zigzags were apparent, indicating directional movement of FtsZ polymers (fig. S9, A and B, and movies S4 to S7). Imaging at higher temporal and spatial resolution (12) revealed that FtsZ polymers exhibited apparently transverse, processive movement across the short axis of the cell, particularly in shorter cells (Fig. 2, A to D; fig. S10; movie S3; and movies S8 to S13). This dynamic movement likely underlies a previous study reporting oscillatory waves of FtsZ (21).

Because individual FtsZ molecules remain stationary in polymers (fig. S11) (15, 22, 23), the processive movement of FtsZ polymers is most consistent with polymerization at one end and depolymerization at the other, an essential feature of treadmilling. Indeed, treadmilling of FtsZ in vitro has recently been observed (22). Three-dimensional structured illumination microscopy time-lapse imaging directly showed circumferential treadmilling of essentially all Z-rings (Fig. 2, E and F, and movie S14). Using kymographs, we determined the apparent

polymerization and depolymerization speeds of each trajectory (Fig. 2C) (I2) and their distributions, which were similar (Fig. 2D and table S1), consistent with the classic definition of treadmilling. Hereafter, we refer to the average of these two speeds as the treadmilling speed (table S1).

The treadmilling speed of each mutant strongly correlated with k_{cat} (Fig. 2G) and

with the fluctuation frequency (Fig. 2H). Whole-genome sequencing did not reveal secondary point mutations that could account for these behaviors (table S4). Therefore, although other polymeric properties of FtsZ and/or interactions may also contribute, our data strongly indicate that FtsZ's GTPase activity underlies treadmilling.

Next, we investigated the role of FtsZ treadmilling in cell division. Using scanning electron microscopy, we confirmed that FtsZ mutants with severe disruptions to GTPase activity frequently exhibited slanted, twisted, and/or incomplete septum morphologies (Fig. 3A and fig. S12) (24–26). Although it has been suggested that the pattern of FtsZ localization dictates the shape of the invagi-

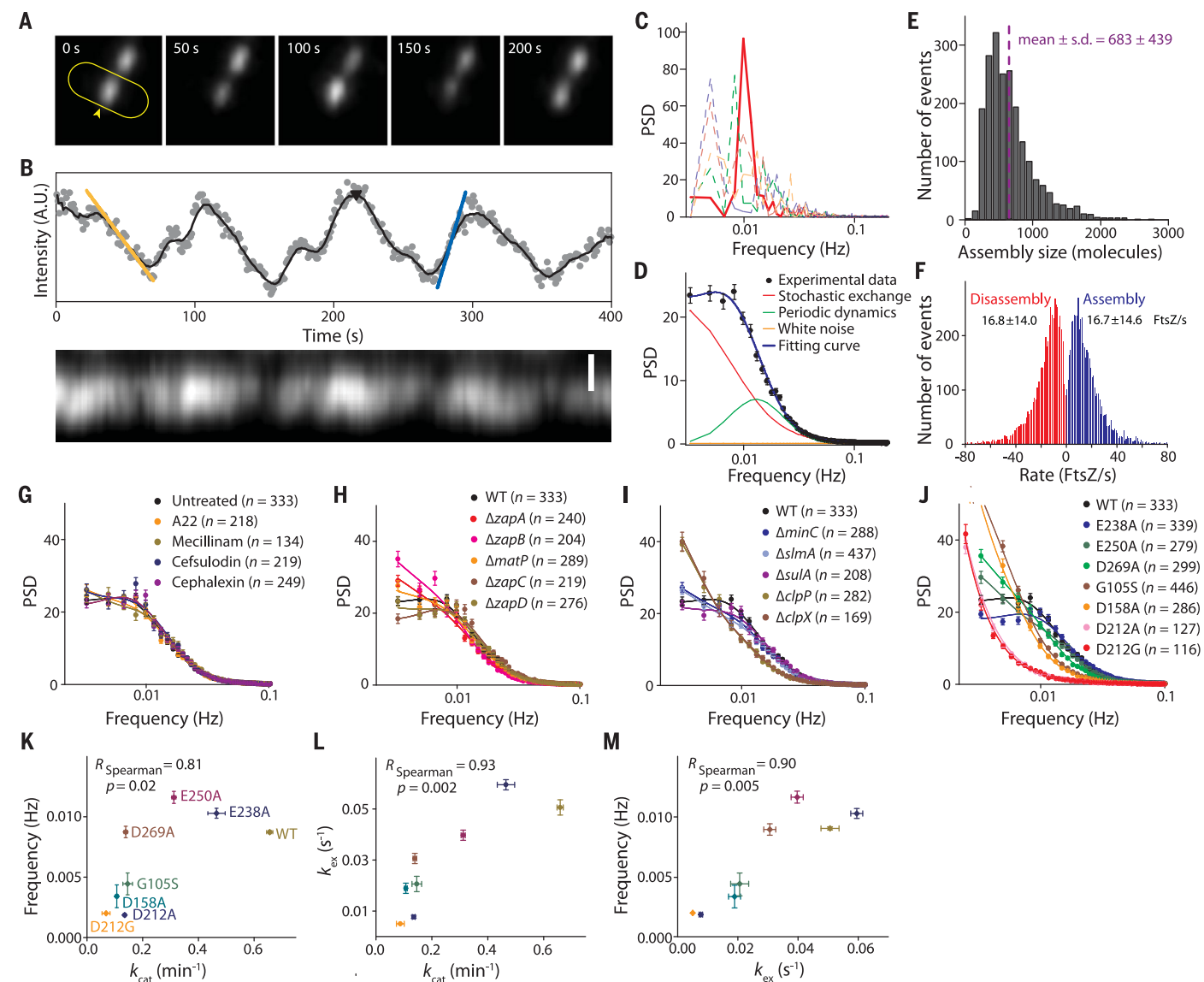


Fig. 1. FtsZ exhibits periodic dynamics coupled to GTPase activity. (A) Montages of live *E. coli* cells showing periodic FtsZ-GFP (arrowhead) intensity fluctuations. (B) Integrated fluorescence time trace and kymograph of the cell outlined in (A) (1 frame/s; movie S1). The black curve is the moving average (every 20 points) of the raw intensity (gray dots). The assembly and disassembly rates were determined as the maximal slopes along each rise (blue line) and decay (yellow line), respectively. Assembly size was estimated from intensity peaks (black arrowhead) (I2). Scale bars, 0.5 μm . (C) Representative power spectral density (PSD) curves for individual cells (dashed lines), with the one from (B) highlighted in solid red. (D) The mean PSD over all cells (\pm SEM; $n = 333$ cells), fitted with a model (blue curve) that takes into account stochastic subunit exchange between the Z-ring and the cytoplasmic pool (red curve) and the periodic fluctuations (green curve) (I2). (E) FtsZ assembly size distribution

with 683 ± 439 FtsZ and FtsZ-GFP molecules ($n = 2039$ fluorescence peaks). (F) Distributions of assembly and disassembly rates. (G to J) Average PSD curves in drug-treated cells (G), in cells lacking Z-ring stabilizers (H) or regulators (I), and in cells expressing FtsZ GTPase mutants (J). In (G), cells were treated with A22 (inhibitor of MreB), mecillinam (inhibitor of the elongation-specific transpeptidase PBP2), cefsulodin (inhibitor of division-specific glycosyltransferase and transpeptidase PBP1b), and cephalixin (inhibitor of the division-specific transpeptidase FtsI) at concentrations above their minimum inhibitory concentration. Error bars denote SEM. (K) The GTPase catalytic turnover rate k_{cat} is correlated with Z-ring periodic frequency. E238A, Glu²³⁸ \rightarrow Ala; D269A, Asp²⁶⁹ \rightarrow Ala; G105S, Gly¹⁰⁵ \rightarrow Ser. (L) k_{cat} is correlated with the stochastic exchange rate k_{ex} . (M) k_{ex} is correlated with Z-ring periodic frequency. Error bars denote SD.

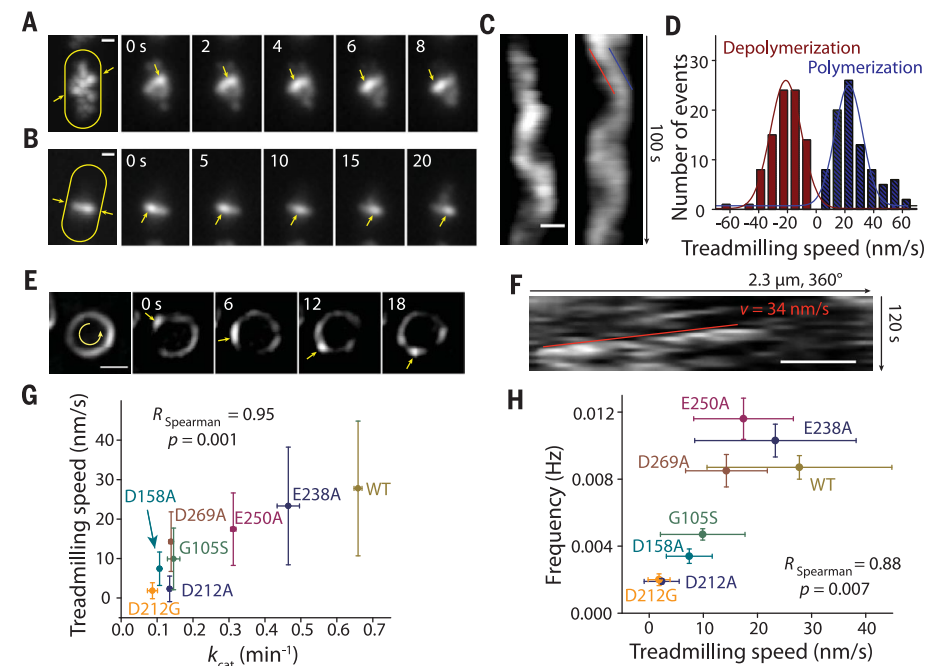


Fig. 2. FtsZ polymers exhibit treadmilling dynamics in live *E. coli* cells. (A and B) Maximum intensity projection (left panels) and montages from time-lapse imaging (movies S8 and S9) of a cell in which a midcell Z-ring was not assembled (A) and a cell with a clearly visible midcell Z-ring (B). (C) Kymographs of the cells in (A) and (B) computed from the intensity along the line between the two yellow arrows. (D) Distributions of polymerization and depolymerization speeds as measured from the leading and trailing edges of individual cells' kymographs [blue and red lines in (C)]. (E) Structured illumination microscopy maximum-intensity projection (left panel) and montage from time-lapse imaging of counter-clockwise Z-ring treadmilling. (F) Kymograph of fluorescence along circumference of cell in (E). (G and H) Treadmilling speeds correlated with k_{cat} (G) and Z-ring dynamics (H). Error bars denote SD. Scale bars, 0.5 μm .

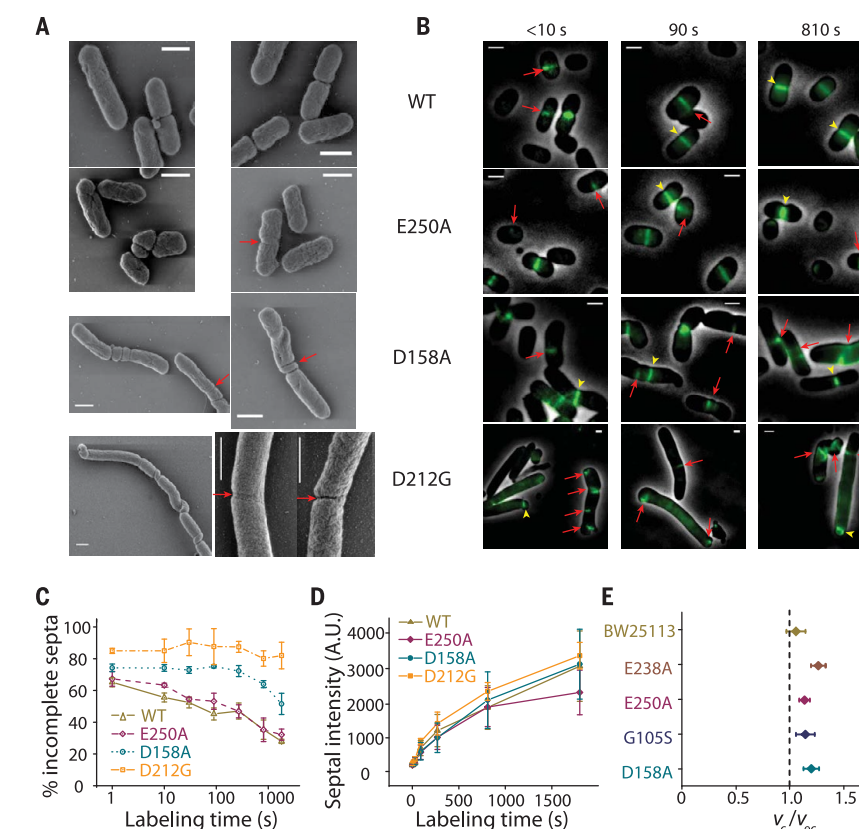


Fig. 3. FtsZ GTPase mutants change the spatial distribution pattern but not the rate of septal PG synthesis. (A) Representative scanning electron microscopy images of FtsZ wild-type, E250A, D158A, and D212G cells. Red arrows denote deformed, asymmetric septa. (B) Representative images of HADA-labeled septa for short (<10 s), intermediate (90 s), and long (810 s) labeling pulses. Red arrows and yellow arrowheads denote incomplete and complete septa, respectively. (C) Severe GTPase mutants had large percentages of cells with incompletely labeled septa even for long pulses. (D) Integrated septal HADA fluorescence increased similarly with labeling pulse duration in all strains. (E) The ratio of septum closure rate (v_c) to elongation rate during constriction (v_{ec}) was similar among tested GTPase mutants. Error bars denote SEM. Scale bars, 1 μm .

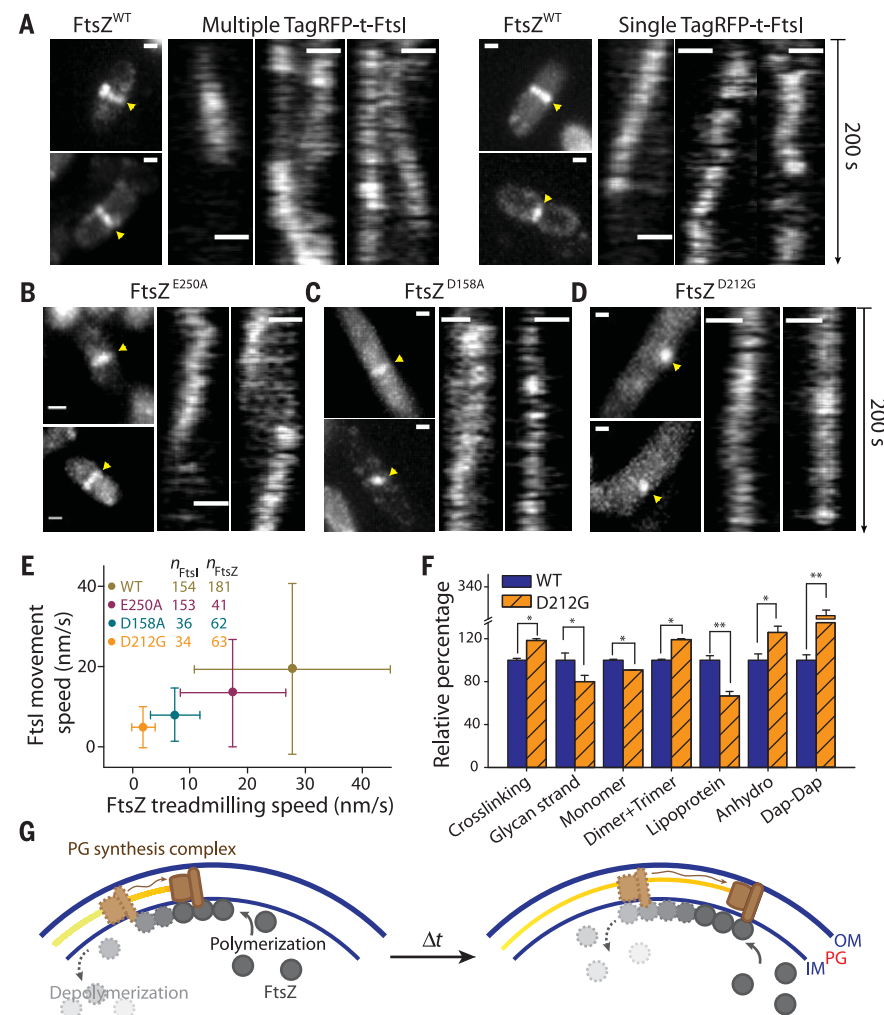


Fig. 4. Altered directional movement of FtsI and septal PG composition in FtsZ^{mut} cells. (A) Directional movement of multiple (left) or single (right) TagRFP-t-FtsI molecules along the septum in FtsZ cells. Images with yellow arrowheads are maximum intensity projections; kymograph images are from positions denoted by the arrowheads. (B to D) Examples of TagRFP-t-FtsI directional movement in E250A (B), D158A (C), and D212G (D) cells. (E) Mean TagRFP-t-FtsI movement speed is highly correlated with FtsZ treadmilling speed; error bars denote SD (see table S1). (F) UPLC analysis reveals altered PG composition in FtsZ^{D212G} cells. The relative percentage of each component of D212G was normalized to that of wild-type cells. Error bars denote SD, $n = 3$; * $P < 0.05$, ** $P < 0.01$ (unpaired t test). (G) A schematic model depicting FtsZ treadmilling (gray circles) that drives directional movement (wavy arrows) of the septal PG synthesis machinery (brown rectangles), leading to processive synthesis of new septal PG (yellow). IM and OM, inner and outer membranes; scale bars, 0.5 μ m.

nating septum (24), this connection has not been supported by superresolution imaging in several species (13, 15–17, 27–31), which showed that the wild-type Z-ring is actually composed of heterogeneously distributed, discontinuous FtsZ clusters. Therefore, it is possible that dynamic remodeling of the Z-ring, rather than its localization pattern, is required for symmetrical invagination (32). We hypothesized that the treadmilling dynamics would allow the Z-ring to sample the surface of the growing septum evenly over time, thereby ensuring a uniform spatial distribution of PG synthesis along the septum. To test this hypothesis, we pulse-labeled wild-type cells and three mutants

with the fluorescent D-alanine analog HCC-amino-D-alanine (HADA) (33). Blocking the activity of either PBP1b or FtsI, two proteins specific for septal cell wall synthesis, abolished septal HADA incorporation (fig. S13), which suggests that incorporation is specific to new septal PG synthesis. We observed that for labeling pulses shorter than the treadmilling period (<100 s), >60% and >80% of wild-type and D212G (Asp²¹² → Gly) cells, respectively, displayed punctate incorporation of HADA at septa (Fig. 3, B and C). With longer pulses (>100 s), the percentage of cells with incompletely labeled septa in wild-type cells and in cells of the mild GTPase mutant E250A (Glu²⁵⁰ → Ala) rapidly dropped

(Fig. 3, B and C). However, large fractions of cells of the more drastic mutants D212G and D158A (Asp¹⁵⁸ → Ala) still had incompletely labeled septa even after 1800 s (Fig. 3, B and C). The total integrated septal HADA intensity increased with longer labeling times, but there was no statistically significant difference between the wild type and the three mutants (Fig. 3D and fig. S14). The septum closure rate, which should be proportional to the total septal PG synthesis rate, was essentially the same as that of the wild type for all mutants except D212A and D212G (Fig. 3E and table S5), as found previously (11); septum closure rate measurements in D212A and D212G were unreliable because of the frequent failure of cell division (movie S15). These data are most consistent with FtsZ GTPase activity affecting the spatiotemporal distribution of synthesis, rather than the septal PG synthesis rate.

Next, we reasoned that because FtsZ recruits many proteins involved in septal synthesis, the dynamics of the essential septal transpeptidase FtsI would likely follow that of FtsZ. Using single-molecule tracking in wide-field epifluorescence microscopy, we tracked the movement of a complementing (fig. S15), N-terminal fluorescent protein fusion of FtsI (TagRFP-t-FtsI) at visible constriction sites in FtsZ^{WT} and three FtsZ^{mut} backgrounds. Kymographs of TagRFP-t-FtsI fluorescence in FtsZ^{WT} cells showed diagonal tracks similar to those of FtsZ (Fig. 4A and fig. S16), indicating that individual TagRFP-t-FtsI molecules moved directionally along the septum, in contrast to stationary FtsZ molecules in treadmilling FtsZ polymers (Fig. 2 and fig. S11) (22). The TagRFP-t-FtsI movement was not unidirectional and exhibited large variations in time and in different cells (Fig. 4A and movies S16 to S18). In the FtsZ^{mut} strains, TagRFP-t-FtsI moved more slowly (Fig. 4, B to D), with mean speed comparable to the corresponding FtsZ treadmilling speed (Fig. 4E). Thus, FtsZ treadmilling guides the directional movement of FtsI and thereby directs the distribution of new septal PG.

Finally, we used ultraperformance liquid chromatography (UPLC) to investigate whether the biochemical composition of the PG itself was altered in D212G cells (12). In both LB and minimal media, D212G cells had shorter glycan strands and greater cross-linking than did wild-type cells (Fig. 4F and fig. S17A), indicating imbalances in the relative levels of septal glycan strand polymerization and cross-linking in FtsZ^{D212G} cells. We also observed a large increase in alternative meso-diaminopimelic acid (Dap-Dap) cross-links (Fig. 4F), indicating that the nature of cross-linking reactions was also

perturbed. We observed that the differences in PG composition between minicells (round DNA-less cells produced by polar divisions) isolated from FtsZ^{D212G} and BW25113 Δ minC cells were similar to the differences seen with intact cells, indicating that the shorter glycans and greater cross-linking are not attributable to aberrant placement of the division site (fig. S17B). A *Caulobacter crescentus* FtsZ mutant showed opposite changes (less cross-linking and longer glycan strands), along with bulging of the septal wall (34). Thus, the balance between glycan strand polymerization and cross-linking activities is likely an important factor in defining the shape of the septum, with FtsZ coordinating the two enzymatic activities.

Our results show that FtsZ engages in treadmilling powered by GTP hydrolysis to spatially organize the septal PG synthesis machinery (Fig. 4G) without limiting the rate of septum closure. In *Bacillus subtilis*, FtsZ treadmilling appears to distribute septal PG synthesis and also to dictate the synthesis rate (35). The differences between the two organisms may reflect differential requirements for PG synthesis between Gram-negative and Gram-positive bacteria. Furthermore, whereas the actin homolog MreB relies on wall synthesis for its movement, FtsZ exploits its innate treadmilling capacity to control the movement of septal synthesis enzymes. The broad conceptual similarities among FtsZ, MreB, and the movement of cellulose synthase complexes along cortical microtubules in plants (36) suggest that coupling cytoskeletal motion to wall synthesis may be a general strategy across the kingdoms of life to ensure evenly distributed, robust septal wall synthesis and morphogenesis through time-averaging.

REFERENCES AND NOTES

1. E. Nogales, K. H. Downing, L. A. Amos, J. Löwe, *Nat. Struct. Biol.* **5**, 451–458 (1998).
2. S. Vaughan, B. Wickstead, K. Gull, S. G. Addinall, *J. Mol. Evol.* **58**, 19–29 (2004).
3. E. F. Bi, J. Lutkenhaus, *Nature* **354**, 161–164 (1991).
4. A. J. Egan, W. Vollmer, *Ann. N.Y. Acad. Sci.* **1277**, 8–28 (2013).

5. P. de Boer, R. Crossley, L. Rothfield, *Nature* **359**, 254–256 (1992).
6. D. Raychaudhuri, J. T. Park, *Nature* **359**, 251–254 (1992).
7. Y. Chen, K. Bjornson, S. D. Redick, H. P. Erickson, *Biophys. J.* **88**, 505–514 (2005).
8. J. Stricker, P. Maddox, E. D. Salmon, H. P. Erickson, *Proc. Natl. Acad. Sci. U.S.A.* **99**, 3171–3175 (2002).
9. H. P. Erickson, *Proc. Natl. Acad. Sci. U.S.A.* **106**, 9238–9243 (2009).
10. E. Bi, J. Lutkenhaus, *J. Bacteriol.* **172**, 5602–5609 (1990).
11. C. Coltharp, J. Buss, T. M. Plumer, J. Xiao, *Proc. Natl. Acad. Sci. U.S.A.* **113**, E1044–E1053 (2016).
12. See supplementary materials.
13. J. Buss *et al.*, *PLOS Genet.* **11**, e1005128 (2015).
14. D. A. Moore, Z. N. Whatley, C. P. Joshi, M. Osawa, H. P. Erickson, *J. Bacteriol.* **199**, e00553-16 (2016).
15. J. Buss *et al.*, *Mol. Microbiol.* **89**, 1099–1120 (2013).
16. V. W. Rowlett, W. Margolin, *Biophys. J.* **107**, L17–L20 (2014).
17. M. P. Strauss *et al.*, *PLOS Biol.* **10**, e1001389 (2012).
18. H. A. Arjes, B. Lai, E. Emelue, A. Steinbach, P. A. Levin, *BMC Microbiol.* **15**, 209 (2015).
19. C. Lu, J. Stricker, H. P. Erickson, *BMC Microbiol.* **1**, 7 (2001).
20. B. D. Bennett *et al.*, *Nat. Chem. Biol.* **5**, 593–599 (2009).
21. S. Thanedar, W. Margolin, *Curr. Biol.* **14**, 1167–1173 (2004).
22. M. Loose, T. J. Mitchison, *Nat. Cell Biol.* **16**, 38–46 (2014).
23. L. Niu, J. Yu, *Biophys. J.* **95**, 2009–2016 (2008).
24. S. G. Addinall, J. Lutkenhaus, *Mol. Microbiol.* **22**, 231–237 (1996).
25. E. Bi, J. Lutkenhaus, *J. Bacteriol.* **174**, 5414–5423 (1992).
26. J. Stricker, H. P. Erickson, *J. Bacteriol.* **185**, 4796–4805 (2003).
27. G. Fuet *et al.*, *PLOS ONE* **5**, e12680 (2010).
28. S. J. Holden *et al.*, *Proc. Natl. Acad. Sci. U.S.A.* **111**, 4566–4571 (2014).
29. M. Jacquet *et al.*, *MBio* **6**, e01108-15 (2015).
30. Z. Lyu, C. Coltharp, X. Yang, J. Xiao, *Biopolymers* **105**, 725–734 (2016).
31. Z. Li, M. J. Trimble, Y. V. Brun, G. J. Jensen, *EMBO J.* **26**, 4694–4708 (2007).
32. J. Lutkenhaus, S. Pichoff, S. Du, *Cytoskeleton* **69**, 778–790 (2012).
33. E. Kuru *et al.*, *Angew. Chem. Int. Ed.* **51**, 12519–12523 (2012).
34. K. Sundararajan *et al.*, *Nat. Commun.* **6**, 7281 (2015).
35. A. W. Bisson-Filho *et al.*, *Science* **355**, 739–743 (2017).
36. A. R. Paredez, C. R. Somerville, D. W. Ehrhardt, *Science* **312**, 1491–1495 (2006).

ACKNOWLEDGMENTS

We thank members of the Xiao and Huang labs for helpful discussions and technical assistance; E. Goley, P. Levin, C. Coltharp, J. Buss, G. Lan, J. Lutkenhaus, E. Garner, and G. Squyres for critical discussions; E. Kuru, Y. Brun, and M. VanNieuwenhze for the HADA dye and assistance in its use; J. Lutkenhaus for the MC123 strain; H. Erickson for the FtsZ antibody and internal FtsZ-FP fusion; P. de Boer for the TB43 strain; E. Goley, P. Levin, and their lab members for helpful advice on protein purification and GTPase assay; R. Tsien for the TagRFP-t construct; M. Delannoy for assistance with SEM; K. Esther, D. Jesse, and Nikon for assistance with N-SIM imaging; and J. Franklin for assistance with whole-genome sequencing. Supported by NIH New Innovator award DP2OD006466 and NSF career award MCB-1149328 (K.C.H.); an NSF graduate research fellowship and an ARCS Scholar Awards fellowship (A.M.); NIH grant R01 GM086447, NSF EAGER award MCB-1019000, and a Hamilton Smith Innovative Research award (J.X.); and NSF grant PHYS-1066293. We are grateful for the hospitality of the Aspen Center for Physics. HADAs were received under a material transfer agreement from M. VanNieuwenhze at Indiana University.

SUPPLEMENTARY MATERIALS

www.sciencemag.org/content/355/6326/744/suppl/DC1
Materials and Methods
Figs. S1 to S17
Tables S1 to S6

References (37–50)
Movies S1 to S19

26 September 2016
Accepted 20 January 2017
10.1126/science.aak9995

RESEARCH ARTICLE

NEURODEVELOPMENT

Sequential transcriptional waves direct the differentiation of newborn neurons in the mouse neocortex

Ludovic Telley,^{1,7*} Subashika Govindan,^{1,7*} Julien Prados,^{1,7} Isabelle Stevant,^{2,7} Serge Nef,^{2,7} Emmanouil Dermitzakis,^{2,5,6,7} Alexandre Dayer,^{1,3,7} Denis Jabaudon^{1,4,7,†}

During corticogenesis, excitatory neurons are born from progenitors located in the ventricular zone (VZ), from where they migrate to assemble into circuits. How neuronal identity is dynamically specified upon progenitor division is unknown. Here, we study this process using a high-temporal-resolution technology allowing fluorescent tagging of isochronic cohorts of newborn VZ cells. By combining this *in vivo* approach with single-cell transcriptomics in mice, we identify and functionally characterize neuron-specific primordial transcriptional programs as they dynamically unfold. Our results reveal early transcriptional waves that instruct the sequence and pace of neuronal differentiation events, guiding newborn neurons toward their final fate, and contribute to a road map for the reverse engineering of specific classes of cortical neurons from undifferentiated cells.

During neocortical development, distinct classes of neurons assemble to form local and long-range circuits. Although class-specific genes and features identify cortical neuron types relatively late in differentiation (1–5), early postmitotic fate specification programs have been inaccessible. Here, we describe the dynamic transcriptional activity controlling layer 4 (L4) excitatory neuron birth and differentiation in the mouse neocortex.

Mammalian cortical progenitor cells in the ventricular zone (VZ) undergo DNA synthesis [S-phase, susceptible to bromodeoxyuridine (BrdU) labeling] at the basal border of the VZ and mitosis (M-phase, lasting about an hour at midcorticogenesis in mice) when their soma is apically located, adjacent to the ventricular space (6, 7). At this location, mitotic cells are susceptible to labeling by intraventricular injection of carboxyfluorescein esters [“FlashTag” (FT)], which bind to and fluorescently label

intracellular proteins (8). The short extracellular half-life of FT in the mouse ventricular space ensures effective pulse-labeling of juxtaventricular dividing cells (Fig. 1A and fig. S1). Intracellularly, FT is linearly diluted at each mitosis, such that fluorescence reflects the number of cell divisions that have occurred since the time of labeling (fig. S1, D and E, and movie S1) (8). FT⁺ newborn cells synchronously moved away from the ventricular wall within 3 hours of labeling (Fig. 1A, bottom), reached the subventricular zone (SVZ) within 12 hours, and entered the cortical plate (CP) 24 to 48 hours after mitosis (Fig. 1B). Isochronic cohorts of VZ cells born at the time of injection can thus be specifically identified and tracked during their initial differentiation.

The laminar fate of FT⁺ neurons was linked to the day of FT injection at all ages examined [embryonic day (E) 11.5 to E17.5] (fig. S2 and Fig. 1C). At postnatal day (P) 7, when neuronal migration is complete, E14.5-labeled FT⁺ neurons were restricted to a sublamina of L4 (Fig. 1C). These neurons were born at the time of the FT pulse, not later, because they mostly remained unlabeled after continuous BrdU administration beginning at the time of the FT pulse (fig. S1, B to D). Injection of FT at E14 and E14.5 using two dye colors in the same embryo showed two distinct populations of labeled neurons within L4 at P7, revealing a tight relationship between time of birth

and final radial location, even within a single layer (Fig. 1D). Thus, we used E14.5 FT injections to label L4 neurons *in vivo* from the time of mitosis in the VZ and track their early molecular differentiation.

We observed that newborn cells sequentially expressed PAX6, a VZ marker, TBR2 a SVZ marker, and the early neuronal protein TBR1 (9, 10) within the first 48 hours after mitosis (fig. S3). This reveals a highly dynamic cellular process characterized by overlapping signature shifts in protein expression. For an unbiased account of the transcriptional programs active just after cell birth in single cells, we isolated E14.5-born FT⁺ cells 6, 12, 24, and 48 hours after mitosis by using cortical microdissection followed by fluorescence-activated cell sorting (FACS). We characterized transcriptional activity using single-cell RNA sequencing in microfluidically isolated single cells (fig. S4, A and B) (1, 11, 12).

To determine the sequence and pace of early differentiation processes, we first examined the expression dynamics of a core set of genes involved in proliferation, neurogenesis (i.e., which promote differentiative divisions), and neuronal differentiation. We found that proliferative (P), neurogenic (Ng), and neuronal (N) transcripts were sequentially expressed: All P transcripts were repressed first, Ng transcripts showed delayed repression, and N transcripts were induced after cell division (see fig. S4C and table S1). The closely timed repression of P and Ng transcripts reveals that exit from the cell cycle and initial postmitotic specification are partially overlapping rather than strictly sequential processes. We used these program-specific dynamics to identify a broader set of proliferative-type (P_{type}), neurogenic-type (Ng_{type}), and neuronal-type (N_{type}) transcripts (fig. S4D and data table S1). The functional relevance of these three programs was supported by the enrichment of P_{type}, Ng_{type}, and N_{type} transcripts in the VZ, SVZ, and CP, respectively; differential enrichment in specific gene ontology terms; and sequential expression in single cells (fig. S4, D and E, and fig. S5). These findings reveal the highly dynamic unfolding of proliferative, neurogenic, and neuronal programs after mitosis *in vivo*.

Two main classes of juxtaventricular cells are initially labeled by FT in the VZ: (i) progenitor cells and (ii) newborn neurons (Fig. 1A and fig. S1D). We sought to identify neuron-specific transcriptional programs by distinguishing neurons from progenitors. For this purpose, we used a machine-learning approach to cluster cells based on transcriptional expression signatures (13).

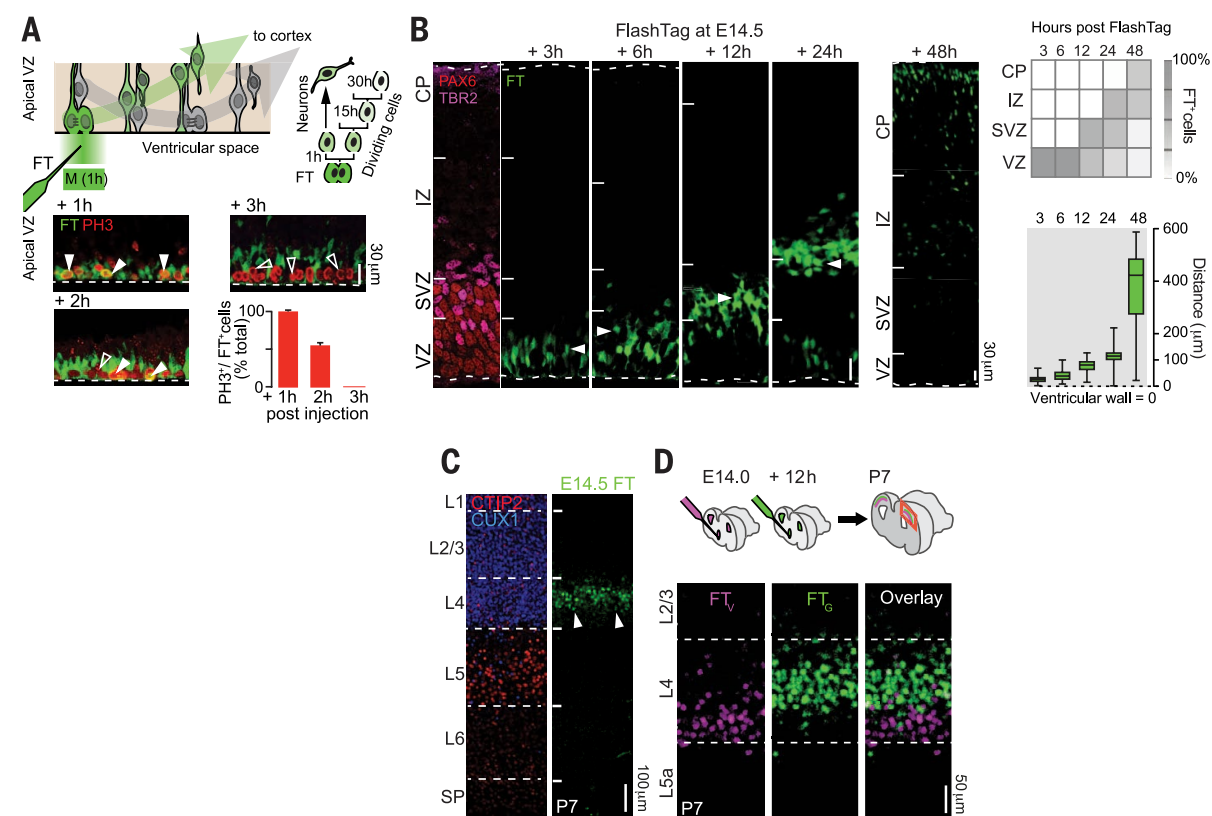


Fig. 1. FT labels time-locked cohorts of newborn VZ cells during corticogenesis. (A) (Top) Schematic representation of the FT labeling principle. (Bottom) Pulse-labeling of isochronic mitotic cells using FT at E14.5. PH3, phospho-histone 3, an M-phase marker. (B) Isochronic cohorts of FT⁺ cells radially migrate from the VZ to the CP. PAX6 and TBR2 delineate the VZ and SVZ. (C) E14.5 FT labeling identifies a subset of L4 neurons at P7. (D) E14 (FT_v⁺) and E14.5 (FT_G⁺) VZ-born neurons occupy distinct sublaminae within L4. Cx, cortex; IZ, intermediate zone. See also figs. S1 and S2.

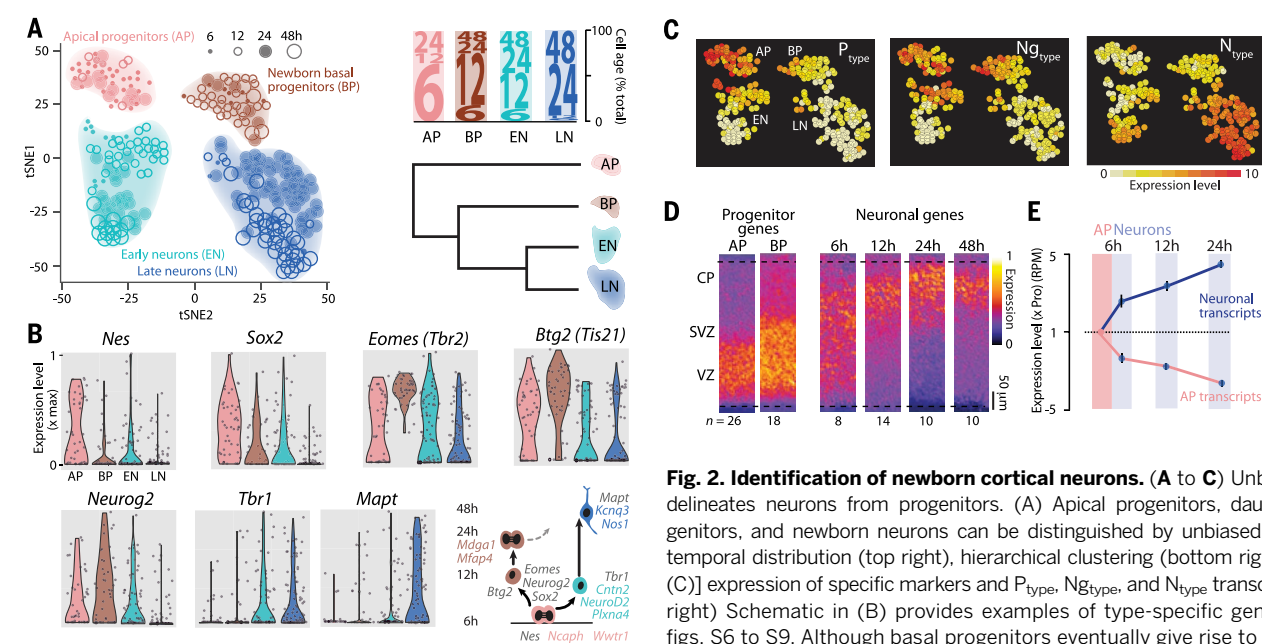


Fig. 2. Identification of newborn cortical neurons. (A to C) Unbiased clustering delineates neurons from progenitors. (A) Apical progenitors, daughter basal progenitors, and newborn neurons can be distinguished by unbiased clustering (left), temporal distribution (top right), hierarchical clustering (bottom right), and [(B) and (C)] expression of specific markers and P_{type}, Ng_{type}, and N_{type} transcripts. (B, bottom right) Schematic in (B) provides examples of type-specific genes presented in figs. S6 to S9. Although basal progenitors eventually give rise to neurons (dotted arrow), this progeny is not included in the current data set because FT⁺ cells are

essentially VZ-born (see fig. S1). (D) Spatial segregation of progenitor and neuron-specific transcripts with *in situ* hybridization (24). Values represent median expressions for several transcripts. (E) Rapid segregation of cell-type-specific transcripts after cytokinesis. $P < 0.0001$ for all values compared to 6-hour apical progenitor (AP) values.

¹Department of Basic Neurosciences, University of Geneva, Switzerland. ²Department of Genetic Medicine and Development, University of Geneva, Switzerland. ³Department of Psychiatry, Geneva University Hospital, Switzerland. ⁴Clinic of Neurology, Geneva University Hospital, Switzerland. ⁵Biomedical Research Foundation Academy of Athens, Greece. ⁶Center of Excellence in Genomic Medicine Research, King Abdulaziz University, Saudi Arabia. ⁷Institute for Genetics and Genomics in Geneva (IGG3), University of Geneva, Switzerland.

*These authors contributed equally to this work. †Corresponding author. E-mail: denis.jabaudon@unige.ch

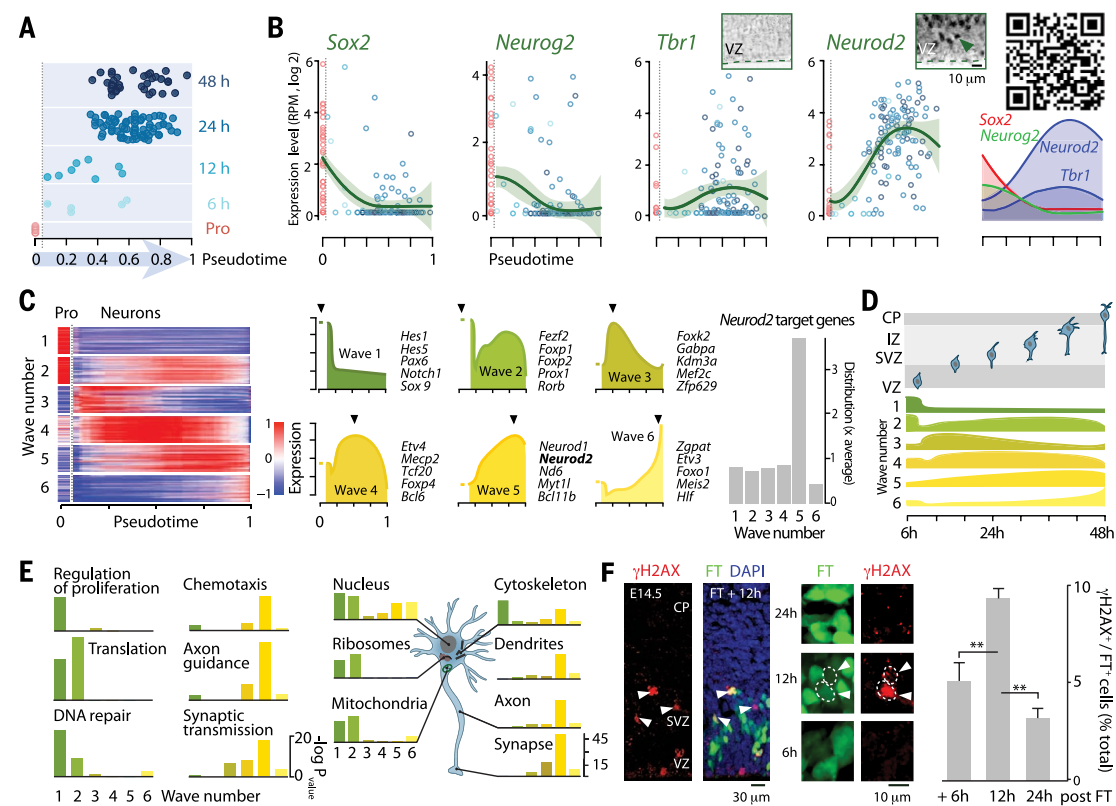


Fig. 3. Real-time functional transcriptomics of early postmitotic neurons in vivo. (A) Neurons are staggered by age along the pseudotime axis. (B) Gene expression dynamics for classical proliferative (*Sox2*), neurogenic (*Neurog2*), and neuronal (*Tbr1*) genes. *Neurod2* is expressed more strongly and earlier than *Tbr1*. QR code, <http://genebrowser.unige.ch/science2016>, for access to dynamics of all transcripts. (C) Unbiased clustering of genes based on expression dynamics reveals distinct transcriptional waves with sequential expression peaks (black arrowheads). Illustrative transcription factors are provided for each wave (see also fig. S10 and data table S3). (Right) Chromatin immunoprecipitation sequencing–identified targets of NEUROD2 (18) are enriched in its own wave but also are present across waves (see also fig. S11). (D) Summary of wave dynamics related to developmental time. (E) Gene ontology term-based analysis. Colors correspond to wave numbers. (F) Double-strand DNA breaks are transiently increased in 12-hour-old cells, as indicated by the presence of phosphorylated histone 2AX (γ H2AX) (25). $**P < 0.001$.

This approach delineated distinct groups of cells, which were identified as progenitors [genuine apical progenitors and daughter basal progenitors (14)] and neurons (early and late populations) (Fig. 2A). Apical progenitors and daughter basal progenitors were distinguished based on differential expression of markers such as *Eomes* and *Btg2* [which are enriched in basal progenitors (see references in table S1)] (Fig. 2B) and differential enrichment in P_{type} genes (apical > basal progenitors), including *Nes* and *Sox2* (Fig. 2C). Accordingly, cells in the apical progenitor cluster were mostly 6 hours old, whereas newborn basal progenitor identity was more distinct after 12 hours (Fig. 2A, top right). Neurons expressed core neuronal genes such as *Tbr1* and *Mapt*, and were enriched in N_{type} genes

(Fig. 2, B and C). With apical progenitors and their daughter neurons now distinguishable, we identified cell-type specific, stage-specific transcripts by comparing gene expression at each developmental age (data table S2 and fig. S8). Consistent with this classification, apical progenitor genes were predominantly expressed in the VZ, basal progenitor genes extended into the SVZ, and neuronal transcripts showed stage-specific sequential expression in the VZ, SVZ, and CP (Fig. 2D and fig. S9). Hierarchical relationship analysis revealed that apical progenitors are clearly distinct from daughter basal progenitors and neurons (Fig. 2A, bottom right), further supporting the lineage relationships identified above. Segregation of type-specific transcripts between newborn neurons and their pro-

genitors was detected as early as 6 hours after mitosis (Fig. 2E). This suggests that type-specific transcripts can be premitotically segregated or differentially stabilized in nascent postmitotic neurons versus progenitors. Together, these data identify progenitor and neuron-specific transcripts activated after cell division and reveal rapid cell-type specific segregation and regulation of transcripts after mitosis.

To establish a real-time quantitative account of differentiation programs in newborn neurons, we used an unsupervised approach in which single-cell expression profiles are temporally ordered based on distinct intermediate differentiation states (Fig. 3A) (15, 16). This method appropriately ordered neurons along a pseudotime axis, with 6-, 12-, 24-, and 48-hour-old neurons

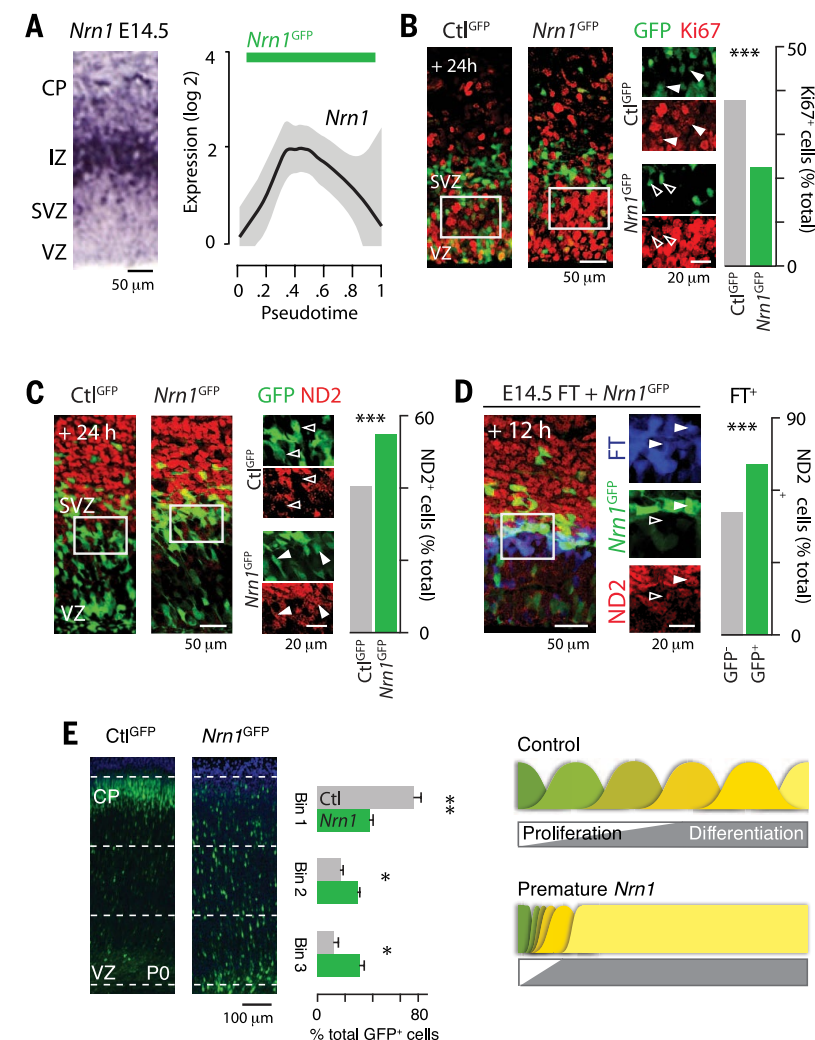


Fig. 4. Early expression of the late-wave gene *Nrn1* induces premature neuronal differentiation. (A to D) Premature expression of *Nrn1* (A) leads to a forward shift in neuronal differentiation by inducing cell-cycle exit (decreased number of $Ki67^+$ progenitors) (B) and premature neuronal differentiation (increased number of $ND2^+$ neurons) (C). This effect occurs within 12 hours of birth, as assessed within an isochronic 12-hour-old cohort of FT^+ cells (D). (A, left) In situ hybridization (24). (E) *NRN1*-overexpressing neurons undergo premature migrational arrest before reaching L4. $*P < 0.05$; $**P < 0.001$; $***P < 0.0001$. $ND2$, NEUROD2.

being progressively staggered along this time line (Fig. 3A). This allowed us to reconstruct the expression dynamics of all transcripts across this pseudotime axis and generate a high-resolution transcriptomic atlas of the first 48 hours of L4 cortical neuron development (Fig. 3B) (see <http://genebrowser.unige.ch/science2016> for the data set of all transcripts). The expression dynamics of classical P (*Sox2*), Ng (*Neurog2*), and N (*Tbr1*) transcripts were consistent with their function (Fig. 3B).

Neurod2 was identified as an early-onset neuronal transcript; accordingly, NEUROD2 protein was detected in newborn apical VZ neurons, whereas this was not the case for *TBR1* (Fig. 3B, inset).

Clustering of expressed transcripts based on their expression dynamics showed how transcriptional networks are organized in newborn neurons. Directly after mitosis, waves of transcriptional programs sequentially unfold, each including temporally distinct complements of transcription fac-

tors and networks (Fig. 3, C and D, fig. S10, data table S3, and movie S2). To understand the temporal organization of the molecular pathways across differentiation, we focused on the genetic network of *Neurod2*, a wave 5 transcription factor required for L4 neuron maturation and whose target genes have been identified in the E14.5 neocortex (17, 18). The temporal distribution of NEUROD2 target genes across the distinct waves was not random (Fig. 3C, right, and data table S4). Instead, NEUROD2 targets were strongly enriched in its own wave (e.g., *Nrn1* and *Ephb2*), in line with its role in neurogenesis, but also present across waves, including in wave 1, where targets include cyclins and cyclin-dependent kinases such as *Cend2*, *Cend3*, and *Cdk13*, which control cell cycle progression. NEUROD2 may therefore act not only on isochronically expressed genes but also across differentiation. Consistent with a repressive action on wave 1 targets, overexpression of NEUROD2 through in utero electroporation into VZ progenitors induced exit from the cell cycle, as indicated by decreased numbers of $Ki67^+$ VZ cells (fig. S11). Single transcription factors can therefore control distinct differentiation events through combinatorial actions on a variety of temporally gated genetic targets and networks.

Ontology term analysis of the transcriptional waves identified successive functional differentiation events in newborn neurons (Fig. 3E). We observed an initial rapid (6 to 12 hours after mitosis) repression of proliferation-associated transcripts (e.g., *Arx*, *Notch1*, and *Sox9*) and a surge in transcripts associated with ribosome biogenesis and translation (e.g., *Etf1*, *Rpl13a*, and *Rpl12*), which might reflect nucleolar reassembly and increased protein synthesis. Transcripts associated with DNA repair (e.g., *DNA2*, *Ddb1*, and *Exo1*) were transiently increased after mitosis, suggesting postmitotic genetic instability. Consistent with this possibility, DNA double-strand breaks were significantly increased in 12-hour-old neurons (Fig. 3F). This reveals a critical period after mitosis during which neocortical neurons are susceptible to somatic mutations and where clonal mosaicism could be generated (19, 20). Twelve-hour-old neurons already initiated differentiation programs related to late-occurring processes such as synaptogenesis, revealing an early transcriptional poise in anticipation of terminal differentiation events. Finally, chemotaxis-associated transcripts (e.g., *Ephb1*, *LICAM*, and *Nrp1*) peaked around 42 hours after birth, while neurons are reaching the CP, providing a molecular framework for input-dependent differentiation processes (21).

Finally, we examined whether the distribution of transcript expression across waves instructs the sequence and pace of neuronal differentiation events. For this purpose, we prematurely expressed a late-wave transcript, *Nrn1*, which normally peaks ~30 hours after mitosis (wave 5, Fig. 4A) and controls L4 neuron maturation through promotion of neurogenesis (22, 23). We hypothesized that heterochronic expression of this normally late-occurring gene could bypass early processes and accelerate neuronal differentiation. Indeed, in utero electroporation of *Nrn1* led to premature transition to neuronal identity and precocious expression of NEUROD2 (Fig. 4, B and C). Premature acquisition of this neuronal trait was detectable as early as 12 hours after cell birth, as revealed by assessing NEUROD2 expression within an isochronic 12-hour-old cohort of FT⁺ cells with mosaic overexpression of NRN1 (Fig. 4D). Finally, precocious molecular maturation was associated with an early loss of migrational capacity, leading to neuronal mispositioning at birth (Fig. 4E). Therefore, the precise timing of early differentiation programs is critical not only for the execution of single-cell differentiation events but also for the successful organization of the cortical networks to which it belongs. Precise and dynamic temporal control over the expression of even single genes thus controls the sequence and pace of neuronal differentiation, which is essential for circuit assembly.

Our data provide a comprehensive transcriptional blueprint outlining the dynamic acquisition of neuronal identity in vivo. We show that early neuronal differentiation is directed by a series of transcriptional waves whose proper sequence is critical for normal progression through development. These waves provide discrete time windows during which specific transcriptional complexes are present simultaneously and can interact. These transient combinatorial transcriptional niches could act as

sequential checkpoints during the course of differentiation, combinatorially coding for specific cell fates. These results build a road map for reverse engineering of cortical neuron subtypes from undifferentiated cells and provide a set of genetic targets for identification and directed differentiation of progenitors and nascent neurons.

REFERENCES AND NOTES

1. A. Zeisel *et al.*, *Science* **347**, 1138–1142 (2015).
2. T. G. Belgard *et al.*, *Neuron* **71**, 605–616 (2011).
3. P. Arlotta *et al.*, *Neuron* **45**, 207–221 (2005).
4. B. J. Molyneaux *et al.*, *Neuron* **85**, 275–288 (2015).
5. S. Fertilizinhos *et al.*, *Cell Rep.* **6**, 938–950 (2014).
6. Y. Kosodo *et al.*, *EMBO J.* **30**, 1690–1704 (2011).
7. E. Taverna, M. Götz, W. B. Huttner, *Annu. Rev. Cell Dev. Biol.* **30**, 465–502 (2014).
8. B. J. C. Quah, C. R. Parish, *J. Vis. Exp.* 2010, e2259 (2010).
9. M. Götz, A. Stoykova, P. Gruss, *Neuron* **21**, 1031–1044 (1998).
10. C. Englund *et al.*, *J. Neurosci.* **25**, 247–251 (2005).
11. A. A. Pollen *et al.*, *Cell* **163**, 55–67 (2015).
12. A. A. Pollen *et al.*, *Nat. Biotechnol.* **32**, 1053–1058 (2014).
13. E. Z. Macosko *et al.*, *Cell* **161**, 1202–1214 (2015).
14. M. Florio, W. B. Huttner, *Development* **141**, 2182–2194 (2014).
15. C. Trapnell *et al.*, *Nat. Biotechnol.* **32**, 381–386 (2014).
16. J. Shin *et al.*, *Cell Stem Cell* **17**, 360–372 (2015).
17. G. Ince-Dunn *et al.*, *Neuron* **49**, 683–695 (2006).
18. E. Bayam *et al.*, *BMC Genomics* **16**, 681 (2015).
19. P. J. McKinnon, *Nat. Neurosci.* **16**, 1523–1529 (2013).
20. M. A. Lodato *et al.*, *Science* **350**, 94–98 (2015).
21. T. Namba *et al.*, *Neuron* **81**, 814–829 (2014).
22. G. Pouchelon *et al.*, *Nature* **511**, 471–474 (2014).
23. H. Sato *et al.*, *J. Neurosci.* **32**, 15388–15402 (2012).
24. G. Diez-Roux *et al.*, *PLoS Biol.* **9**, e1000582 (2011).
25. E. P. Rogakou, D. R. Pilch, A. H. Orr, V. S. Ivanova, W. M. Bonner, *J. Biol. Chem.* **273**, 5858–5868 (1998).

ACKNOWLEDGMENTS

Annotated data are available at <http://genebrowser.unige.ch/science2016>. We thank R. Hevner for the gift of the TBR1 antibody; A. Benoit, M. Lanzillo, and the Genomics Platform and FACS Facility of the University of Geneva for technical assistance; and E. Azim, A. Carleton, S. Tole, and the members of the Jabaudon laboratory for comments on the manuscript. Work in the Jabaudon laboratory is supported by the Swiss National Science Foundation (PPO0P3_123447), the Synapsis Foundation, and the Brain and Behavior Foundation (NARSAD Grant). S.N. is funded by the Swiss SystemsX Interdisciplinary PhD Grant 51PH10-141994. S.G. and I.S. are supported by the iGe3 PhD Award. A.D. is funded by the Swiss National Science Foundation and the National Center of Competence in Research (NCCR) Synapsy. The authors declare no competing interests. The supplementary materials contain additional data.

SUPPLEMENTARY MATERIALS

www.sciencemag.org/content/351/6280/1443/suppl/DC1
Materials and Methods
Figs. S1 to S11
Table S1
Movies S1 and S2
Data Tables S1 to S4
Database S1
Reference (26)

11 November 2015

Accepted 15 February 2016

Published online 3 March 2016

10.1126/science.aad8361

RESEARCH ARTICLE

OPTICAL IMAGING

Expansion microscopy

Fei Chen,^{1*} Paul W. Tillberg,^{2*} Edward S. Boyden^{1,3,4,5,6,†}

In optical microscopy, fine structural details are resolved by using refraction to magnify images of a specimen. We discovered that by synthesizing a swellable polymer network within a specimen, it can be physically expanded, resulting in physical magnification. By covalently anchoring specific labels located within the specimen directly to the polymer network, labels spaced closer than the optical diffraction limit can be isotropically separated and optically resolved, a process we call expansion microscopy (ExM). Thus, this process can be used to perform scalable superresolution microscopy with diffraction-limited microscopes. We demonstrate ExM with apparent ~70-nanometer lateral resolution in both cultured cells and brain tissue, performing three-color superresolution imaging of ~10⁷ cubic micrometers of the mouse hippocampus with a conventional confocal microscope.

Microscopy has facilitated the discovery of many biological insights by optically magnifying images of structures in fixed cells and tissues. We here report that physical magnification of the specimen itself is also possible.

We first set out to see whether a well-known property of polyelectrolyte gels—namely, that dialyzing them in water causes

expansion of the polymer network into extended conformations (Fig. 1A) (1)—could be performed in a biological sample. We infused into chemically fixed and permeabilized brain tissue (Fig. 1B) sodium acrylate, a monomer used to produce superabsorbent materials (2, 3), along with the comonomer acrylamide and the cross-linker N-N'-methylenebisacrylamide. After triggering

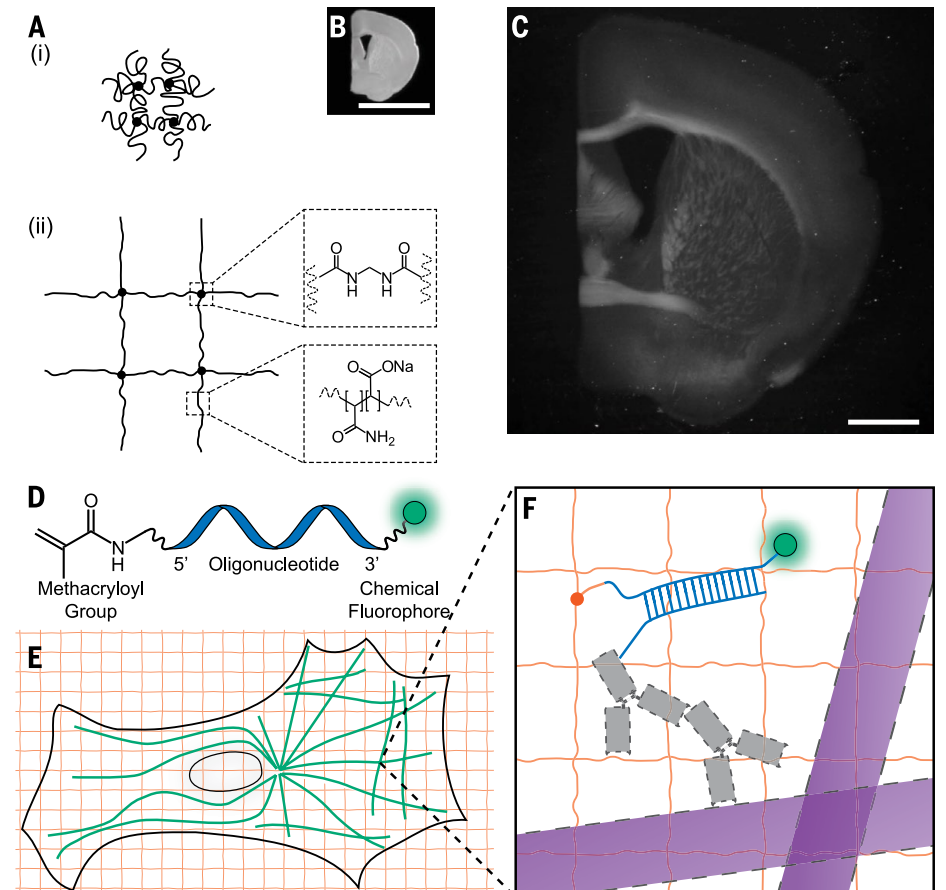


Fig. 1. Expansion microscopy (ExM) concept. (A) Schematic of (i) collapsed polyelectrolyte network, showing crosslinker (dot) and polymer chain (line), and (ii) expanded network after H₂O dialysis. (B) Photograph of fixed mouse brain slice. (C) Photograph, post-ExM, of the sample (B) under side illumination. (D) Schematic of label that can be anchored to the gel at site of a biomolecule. (E) Schematic of microtubules (green) and polymer network (orange). (F) The label of (D), hybridized to the oligo-bearing secondary antibody top (top gray shape) bound via the primary (bottom gray shape) to microtubules (purple), is incorporated into the gel (orange lines) via the methacryloyl group (orange dot) and remains after proteolysis (dotted lines). Scale bars, (B) and (C) 5 mm. Schematics are not to scale.

free radical polymerization with ammonium persulfate (APS) initiator and tetramethylethylenediamine (TEMED) accelerator, we treated the tissue-polymer composite with protease to homogenize its mechanical characteristics. After proteolysis, dialysis in water resulted in a 4.5-fold linear expansion, without distortion at the level of gross anatomy (Fig. 1C). Digestion was uniform throughout the slice (fig. S1). Expanded specimens were transparent (fig. S2) because they consist largely of water. Thus, polyelectrolyte gel expansion is possible when the polymer is embedded throughout a biological sample.

We developed a fluorescent labeling strategy compatible with the proteolytic treatment and subsequent tissue expansion described above, to see whether fluorescence nanoscopy would be possible. We designed a custom fluorescent label (Fig. 1D) that can be incorporated directly into the polymer network and thus survives the proteolytic

¹Department of Biological Engineering, Massachusetts Institute of Technology (MIT), Cambridge, MA, USA.

²Department of Electrical Engineering and Computer Science, MIT, Cambridge, MA, USA. ³Media Lab, MIT, Cambridge, MA, USA. ⁴McGovern Institute, MIT, Cambridge, MA, USA. ⁵Department of Brain and Cognitive Sciences, MIT, Cambridge, MA, USA. ⁶Center for Neurobiological Engineering, MIT, Cambridge, MA, USA.

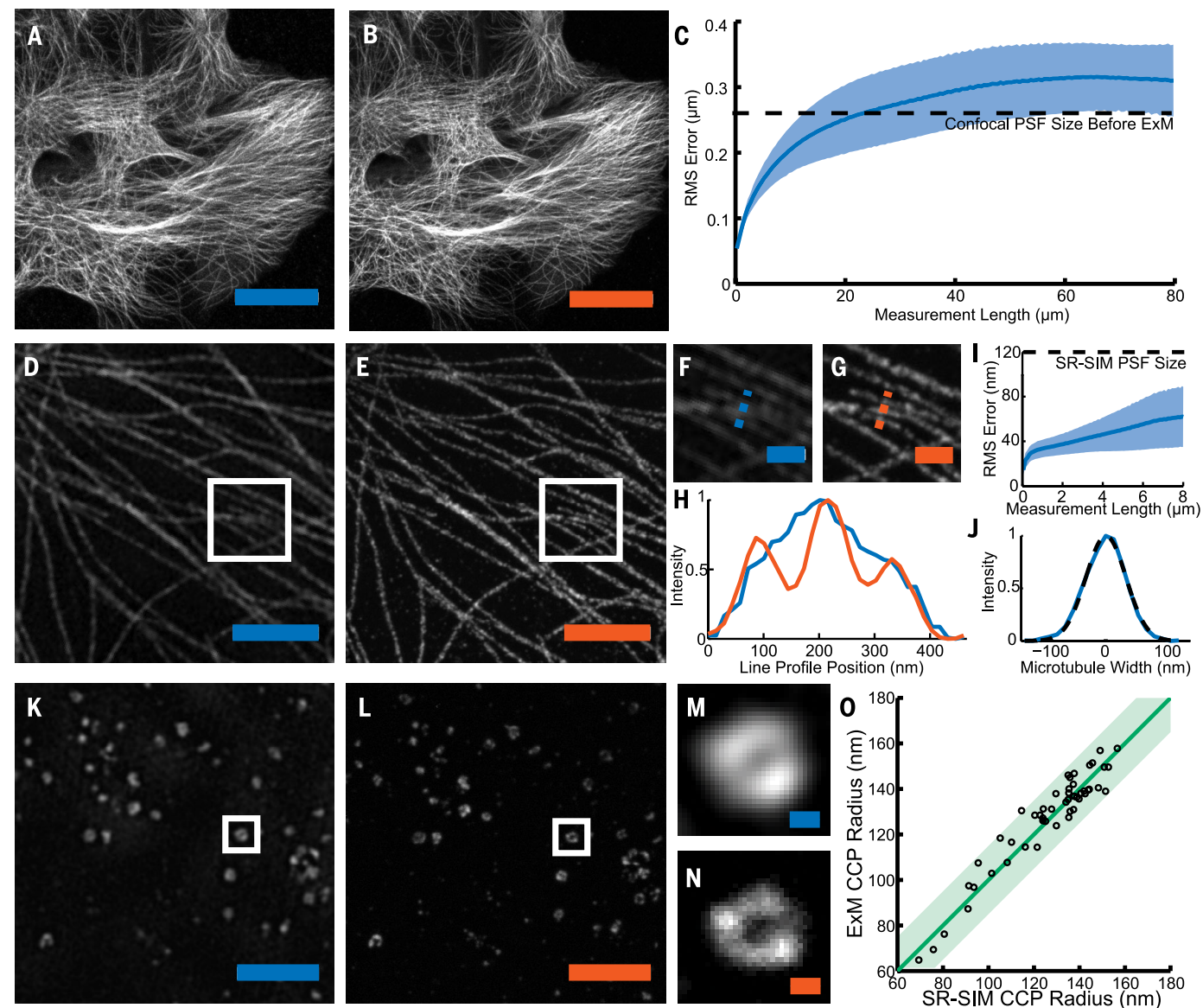
*These authors contributed equally to this work. †Corresponding author. E-mail: esb@media.mit.edu

digestion of endogenous biomolecules. This label is trifunctional, comprising a methacryloyl group capable of participating in free radical polymerization, a chemical fluorophore for visualization, and an oligonucleotide that can hybridize to a complementary sequence attached to an affinity tag (such as a secondary antibody) (Fig. 1, E and F). Thus, the fluorescent tag is targeted to a biomolecule of interest yet re-

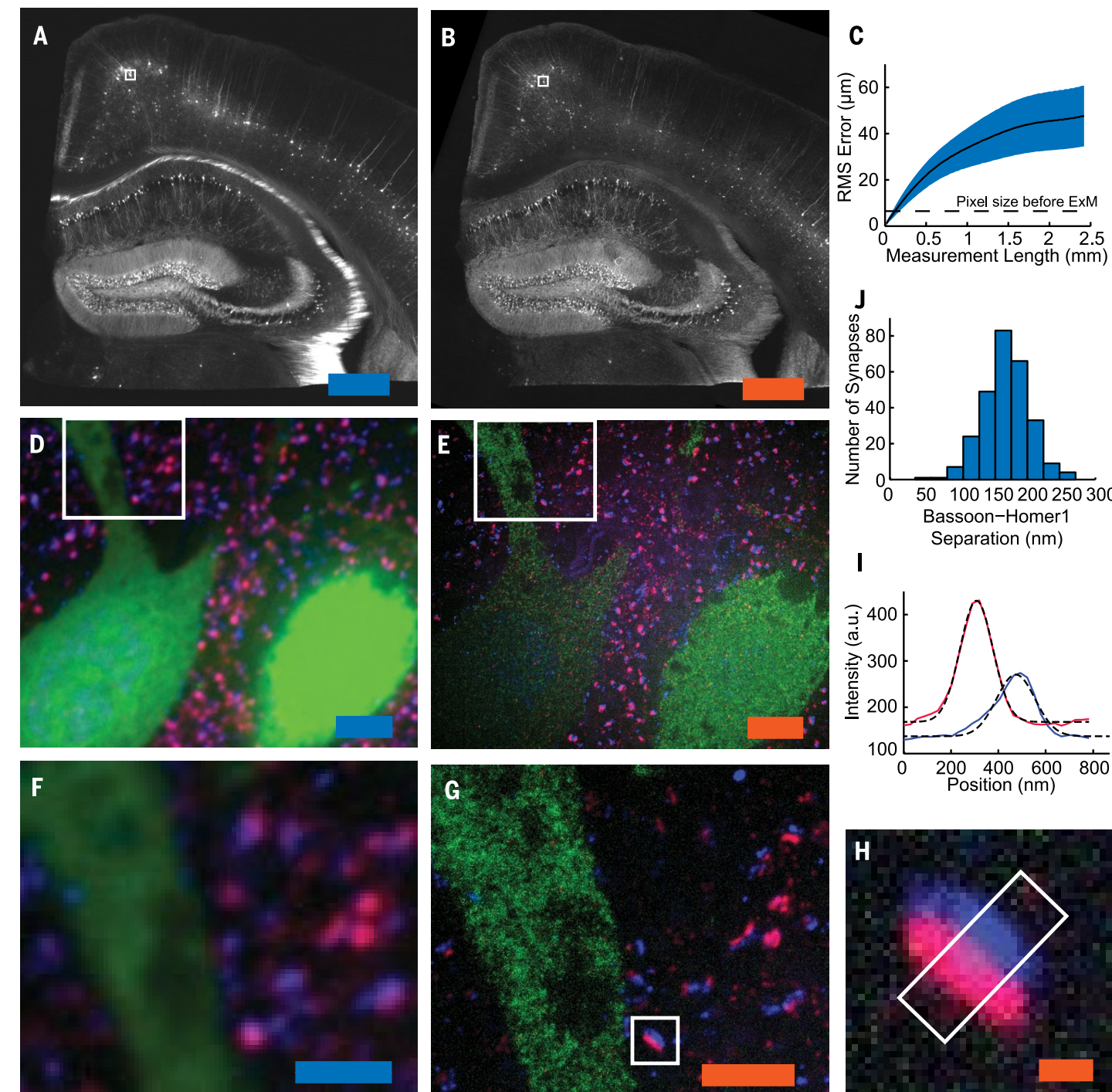
mains anchored covalently with high yield (table S1) to the polymer network. The entire process of labeling, gelation, digestion, expansion, and imaging we call expansion microscopy (ExM).

We performed fluorescence imaging using ExM, examining microtubules in fixed human embryonic kidney (HEK) 293 cells labeled with the trifunctional label and imaged with confocal laser scanning micros-

copy pre- versus post-ExM processing. The post-ExM image (Fig. 2B) was registered to the pre-ExM image (Fig. 2A) via a similarity transformation, resulting in visually indistinguishable images. To quantify the isotropy of ExM, we calculated the deformation vector field between the images via a nonrigid registration process (fig. S3). From this vector field, we quantified the root-mean-square (RMS) error of feature



mean; shaded area, standard deviation; $n = 4$ samples). (J) Transverse profile of a representative microtubule (blue line), with Gaussian fit (black dotted line). (K) SR-SIM image of clathrin-coated pits (CCPs) in HEK293 cells. (L) Post-expansion confocal image of the sample of (K). (M and N) Magnified views of a single CCP in the boxed regions of (K) and (L), respectively. (O) Scatterplot of radii of CCPs measured via ExM versus SR-SIM ($n = 50$ CCPs from 3 samples). Green line, $y = x$ line; shaded green region, half-pixel width of digitization error about the $y = x$ line. Scale bars for pre- versus post-ExM images, (A) 20 μm ; (B) 20 μm (physical size post-expansion, 81.6 μm); (D) 2 μm ; (E) 2 μm (9.1 μm); (F) 500 nm; (G) 500 nm (2.27 μm); (K) 2 μm ; (L) 2 μm (8.82 μm); (M) 100 nm; (N) 100 nm (441 nm).



regions in (D) and (E), respectively. (H) Single representative synapse highlighted in (G). (I) Staining intensity for Bassoon (blue) and Homer1 (red) of the sample of (H) along white box long axis. Dotted black lines, Gaussian fits. a.u., arbitrary units. (J) Bassoon-Homer1 separation ($n = 277$ synapses from four cortical slices). Scale bars for pre- versus post-ExM images, (A) 500 μm ; (B) 500 μm (physical size post-expansion 2.01 mm); (D) 5 μm ; (E) 5 μm (20.1 μm); (F) 2.5 μm ; (G) 2.5 μm (10.0 μm); and (H) 250 nm (1.00 μm).

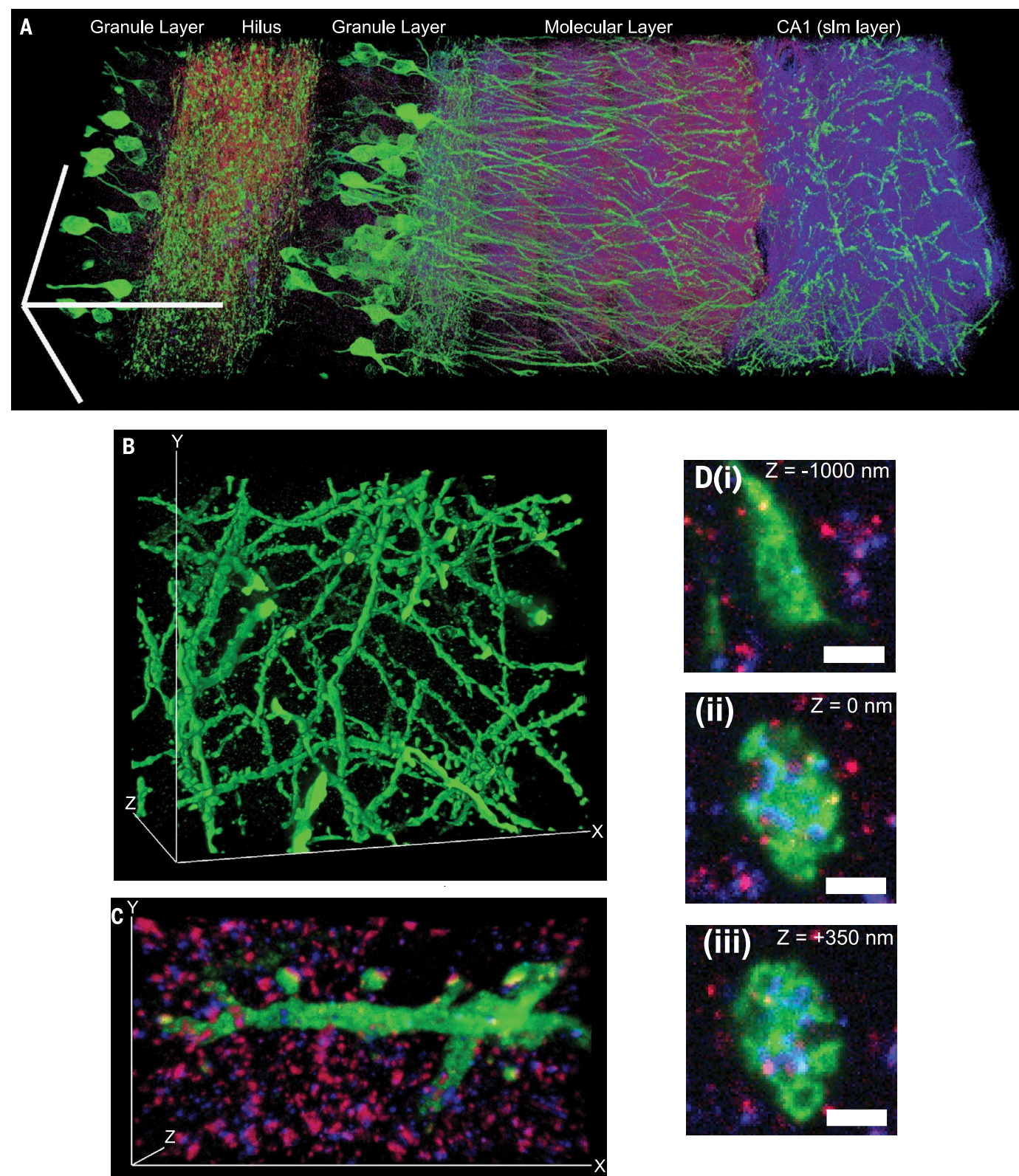


Fig. 4. Scalable 3D superresolution microscopy of mouse brain tissue. (A) Volume rendering of a portion of hippocampus showing neurons (expressing YFP, shown in green) and synapses [marked with anti-Bassoon (blue) and antibody to Homer1 (red)]. (B) Volume rendering of dendrites in CA1 slm. (C) Volume rendering of dendritic branch in CA1 slm. (D) Mossy fiber bouton in hilus of the dentate gyrus. (i) to (iii), selected z-slices. Scale bars, (A) 100 μm in each dimension; (B) 52.7 μm (x); 42.5 μm (y); and 35.2 μm (z); (C) 13.5 μm (x); 7.3 μm (y); and 2.8 μm (z); (D), (i) to (iii) 1 μm .

measurements post-ExM. The errors in length were small ($<1\%$ of distance, for errors larger than the imaging system point spread function size; $n = 4$ samples) (Fig. 2C). Throughout the paper, all distances measured in the post-expansion specimen are reported divided by the expansion factor (supplementary materials, materials and methods).

We next compared pre-ExM conventional superresolution images to post-ExM confocal images. We labeled features traditionally used to characterize the performance of superresolution microscopes, including microtubules (4, 5) and clathrin coated pits (6), and imaged them with a superresolution structured illumination microscope (SR-SIM) pre-ExM, and a spinning disk confocal post-ExM. Qualitatively (Fig. 2, D and E), the images were similar, and quantitatively (Fig. 2I), measurement errors were again on the order of 1% and well within the point spread function size of the SR-SIM microscope ($n = 4$ samples). Microtubule networks were more sharply resolved in ExM (Fig. 2G) than with SR-SIM (Fig. 2F). ExM resolved individual microtubules that could not be distinguished with SR-SIM (Fig. 2H). Microtubules imaged with ExM presented a full-width at half-maximum (FWHM) (Fig. 2J) of 83.8 ± 5.68 nm (mean \pm SD, $n = 24$ microtubules from 3 samples). This FWHM reflects the effective resolution of ExM convolved by the width of the labeled microtubule. To estimate the effective resolution of ExM, we deconvolved [as in (7)] our observed microtubule FWHM by the known immunostained microtubule width [55 nm (6)], conservatively ignoring the width of the trifunctional label, and obtained an effective resolution for ExM of ~ 60 nm. This conservative estimate is comparable with the diffraction-limited confocal resolution [~ 250 -nm lateral resolution (8)] divided by the expansion factor (~ 4.5).

Clathrin-coated pits were also well resolved (Fig. 2, K and L). ExM resolved the central nulls of the pits better than SR-SIM (Fig. 2, M and N). Clathrin-coated pit radii measured via ExM and SR-SIM were highly correlated, with a slope of 1.001 (total least squares regression, confidence interval 0.013 with $P < 0.05$, $n = 50$ pits from three samples) (Fig. 2O). Forty-nine of the 50 points lay within a half-pixel distance of the unity slope line, suggesting that variation in the ExM versus SR-SIM comparison was within the digitization error of the measurement.

We next applied ExM to fixed brain tissue. Slices of brain from Thy1-YFP-H mice expressing cytosolic yellow fluorescent

protein (YFP) under the Thy1 promoter in a subset of neurons (9) were stained with a trifunctional label bearing Alexa 488, using primary antibodies to green fluorescent protein (GFP) (which also bind YFP). Slices expanded fourfold, similar to the expansion factor in cultured cells. We compared pre- versus post-ExM images taken on an epifluorescence microscope. As with cultured cells, the post-ExM image (Fig. 3B) was registered to the pre-ExM image (Fig. 3A) via a similarity transformation. The registered images closely matched, although some features moved in or out of the depth of field because of the axial expansion post-ExM. Quantitatively, post-ExM measurement errors (Fig. 3C, $n = 4$ cortical slices) were 2 to 4%.

We synthesized trifunctional labels with different colors and oligonucleotides (supplementary materials, materials and methods) to enable multicolor ExM. We obtained pre- (Fig. 3D) versus post-ExM (Fig. 3E) images of Thy1-YFP-H mouse cortex with ExM labels directed against YFP (Fig. 3E, green) and the pre- and postsynaptic scaffolding proteins Bassoon (Fig. 3E, blue) and Homer1 (Fig. 3E, red). In the pre-ExM image, Bassoon and Homer1 staining form overlapping spots at each synapse (Fig. 3F), whereas the post-ExM image (Fig. 3G) shows clearly distinguishable pre- and postsynaptic labeling. We quantified the distance between the Bassoon and Homer1 scaffolds, as measured with ExM. We fit the distributions of Bassoon and Homer1 staining intensity, taken along the line perpendicular to the synaptic cleft (Fig. 3H, boxed region), to Gaussians (Fig. 3I). The Bassoon-Homer1 separation was 169 ± 32.6 nm (Fig. 3J, $n = 277$ synapses from four cortical slices), similar to a previous study using stochastic optical reconstruction microscopy (STORM) in the ventral cortex and olfactory bulb, which obtained ~ 150 nm separation (10). We also imaged other antibody targets of interest in biology (fig. S4).

To explore whether expanded samples, scanned on fast diffraction-limited microscopes, could support scalable superresolution imaging, we imaged a volume of the adult Thy1-YFP-H mouse brain spanning 500 by 180 by 100 μm (tissue slice thickness), with three labels (antibody to GFP, green; antibody to Homer1, red; antibody to Bassoon, blue) (Fig. 4A). The diffraction limit of our confocal spinning disk microscope (with 40 \times , 1.15 NA, water immersion objective), divided by the expansion factor, yields an estimated effective resolution of ~ 70 nm laterally and ~ 200 nm axially. Shown in Fig. 4A is a three-dimensional

(3D) rendered image of the data set (an animated rendering is provided in movie S1). Zooming into the raw data set, nanoscale features emerge (Fig. 4, B to D). We performed a volume rendering of the YFP-expressing neurons in a subset of CA1 stratum lacunosum moleculare (slm), revealing spine morphology (Fig. 4B and movie S2). Focusing on a dendrite in CA1 slm, we observed the postsynaptic protein Homer1 to be well localized to dendritic spine heads, with the presynaptic molecule Bassoon in apposition (Fig. 4C and movie S3). Examination of a mossy fiber bouton in the hilus of the dentate gyrus reveals invaginations into the bouton by spiny excrescences of the opposing dendrite, as observed previously via electron microscopy (Fig. 4D) (11). Thus, ExM enables multiscale imaging and visualization of nanoscale features, across length scales relevant to understanding neural circuits.

We report the discovery of a new modality of magnification, namely that fixed cells and tissues, appropriately labeled and processed, can be physically magnified, with isotropic nanoscale resolution (effective ~ 60 -nm lateral resolution). Although acrylate esters have been used for antigen-preserving embedding for electron microscopy (12, 13), ExM represents the first use of an embedded polyelectrolyte gel, used here to expand the specimen. Superresolution imaging methods are slower than their diffraction-limited counterparts because they must resolve more voxels per unit volume. ExM achieves this by expanding the voxels physically. ExM achieves the same voxel throughputs as a diffraction-limited microscope, but at the voxel sizes of a superresolution microscope. Ongoing technology trends for faster diffraction-limited microscopy (14) will continue to boost ExM speed.

The physical magnification of ExM enables superresolution imaging with several fundamental new properties. The axial effective resolution is improved by the same factor as the lateral effective resolution. ExM can achieve superresolution with standard fluorophores, and on a diffraction-limited microscope. Superresolution imaging is often performed within ~ 10 μm of the sample surface because of low signal-to-noise, scattering, and refractive index mismatch. We were able to perform three-color superresolution imaging of a large volume of brain tissue over an axial extent of 100 μm with a spinning disk confocal microscope. Because the ExM-processed sample is almost entirely water, eliminating scattering, ExM may empower fast methods such as light-sheet microscopy (15) to become superresolution methods. ExM potentially

enables labels to be situated within a well-defined, in vitro-like environment, facilitating in situ analysis (16). Because the sample is physically larger, any mechanical errors in post-expansion sectioning, or stage drift, are divided by the expansion factor.

The performance of ExM suggests that despite statistical fluctuations in polymer chain length at the molecular scale, at the nanoscale distances here examined these fluctuations average out, yielding isotropy. Estimates of mesh size for comparable gels suggest that the distance between nearest-neighbor polymer chains are in the ~1 to 2 nm range (17, 18). By tuning the material properties of the ExM polymer, such as the density of cross-links, yet higher effective resolutions may be possible.

REFERENCES AND NOTES

1. T. Tanaka *et al.*, *Phys. Rev. Lett.* **45**, 1636–1639 (1980).
2. I. Ohmine, *J. Chem. Phys.* **77**, 5725 (1982).
3. F. L. Buchholz, *Superabsorbent Polymers* **573**, 27–38 (1994).
4. B. Huang, S. A. Jones, B. Brandenburg, X. Zhuang, *Nat. Methods* **5**, 1047–1052 (2008).
5. E. H. Rego *et al.*, *Proc. Natl. Acad. Sci. U.S.A.* **109**, E135–E143 (2012).
6. M. Bates, B. Huang, G. T. Dempsey, X. Zhuang, *Science* **317**, 1749–1753 (2007).
7. N. Olivier, D. Keller, P. Gönczy, S. Manley, *PLoS One* **8**, (2013).
8. R. W. Cole, T. Jinadasa, C. M. Brown, *Nat. Protoc.* **6**, 1929–1941 (2011).
9. G. Feng *et al.*, *Neuron* **28**, 41–51 (2000).
10. A. Dani, B. Huang, J. Bergan, C. Dulac, X. Zhuang, *Neuron* **68**, 843–856 (2010).
11. A. Rollenhagen, J. H. R. Lübke, *Front. Synaptic Neurosci.* **2**, 2 (2010).
12. G. R. Newman, B. Jasani, E. D. Williams, *Histochem. J.* **15**, 543–555 (1983).
13. K. D. Micheva, S. J. Smith, *Neuron* **55**, 25–36 (2007).
14. B.-C. Chen *et al.*, *Science* **346**, 1257998 (2014).
15. J. Huisken, J. Swoger, F. Del Bene, J. Wittbrodt, E. H. K. Stelzer, *Science* **305**, 1007–1009 (2004).
16. J. H. Lee *et al.*, *Science* **343**, 1360–1363 (2014).
17. A. M. Hecht, R. Duplessix, E. Geissler, *Macromolecules* **18**, 2167–2173 (1985).
18. D. Calvet, J. Y. Wong, S. Giasson, *Macromolecules* **37**, 7762–7771 (2004).

ACKNOWLEDGMENTS

E.S.B. was funded by NIH Director's Pioneer Award 1DP1NS087724 and NIH Director's Transformative Research Award 1R01MH103910-01, the New York Stem Cell Foundation-Robertson Investigator Award, the MIT Center for Brains, Minds, and Machines NSF CCF-1231216, Jeremy and Joyce Wertheimer, Google, NSF CAREER Award CBET 1053233, the MIT Synthetic Intelligence Project, the MIT Media Lab, the MIT McGovern Institute, and the MIT Neurotechnology Fund. F.C. was funded by an NSF Graduate

Fellowship. P.W.T. was funded by a Fannie and John Hertz Graduate Fellowship. Confocal imaging was performed in the W. M. Keck Facility for Biological Imaging at the Whitehead Institute for Biomedical Research. Deltavision OMX SR-SIM imaging was performed at the Koch Institute Swanson Biotechnology Center imaging core. We acknowledge W. Salmon and E. Vasile for assistance with confocal and SR-SIM imaging. We acknowledge N. Pak for assistance with perfusions. We also acknowledge, for helpful discussions, B. Chow, A. Marblestone, G. Church, P. So, S. Manalis, J.-B. Chang, J. Enriquez, I. Gupta, M. Kardar, and A. Wissner-Gross. The authors have applied for a patent on the technology, assigned to MIT (U.S. Provisional Application 61943035). The order of co-first author names was determined by a coin toss. The imaging and other data reported in the paper are hosted by MIT (<http://expansionmicroscopy.org/rawdataScience2014>).

SUPPLEMENTARY MATERIALS

www.sciencemag.org/content/347/6221/543/suppl/DC1
Materials and Methods
Figs. S1 to S5
Tables S1 to S4
References (19–28)
Movies S1 to S3

18 August 2014
Accepted 26 November 2014
10.1126/science.1260088



Nikon
100th
anniversary

Latest Innovations in Nikon Confocal Technology

The laser scanning confocal microscope (LSCM) is an important tool for research across many different fields. Originally invented by Marvin Minsky in 1955, the basic idea behind this technology is to introduce a pinhole into the conjugate focal plane of a microscope system in order to decrease out-of-focus blur and increase contrast in thick specimens. Initially, this concept was not well adopted in the biological sciences, however, recent years have seen an explosion in the availability of laser scanning confocal instrumentation. Due to its popularity, innovation surrounding this technique has continued to this day, with new, confocal-based technologies being developed regularly. Some of these more recent advancements include resonant scanning for high-speed imaging, multispectral techniques for flexible analyses of fluorescent probes and other inherent fluorescent signals, and confocal-based resolution enhancement for interrogating previously unseen details. This white paper will introduce each of these concepts and will highlight recent additions to Nikon's A1R system that can be applied to utilize each of these techniques.

High-Speed, High-Resolution Scanning

In order to form an image using an LSCM, information from the sample must be collected in a point-by-point fashion over some defined field of view. This is achieved by scanning a laser beam across the sample in a precisely timed manner while recording intensities at each point. The resulting map of intensities at each point across the predefined field of view is what produces the images traditionally associated with confocal microscopy. However, when one considers making an image in this way, it immediately becomes clear that collecting data point-by-point may suffer from a disadvantage when it comes to speed. So what sets the speed limit for an LSCM? The most important component in determining the speed of these systems is the galvanometers chosen to raster the laser beam across the sample. A pair of traditional linear galvos is most commonly used for this purpose, with one mirror rapidly scanning across the fast-axis to generate each point, and the other scanning more slowly to determine the beginning of each line. It is the speed of this fast axis galvo that sets the limits for these systems and, for traditional linear galvos at 512x512 pixels, mechanical specifications limit the speed to ~2 frames per second (FPS). Above these speeds, the scanning mirrors generate damaging levels of heat, which can lead to premature failure. Cooling can help to push the limits of linear galvos, but these systems are still not capable of reaching video rates with a full 512x512 frame.

Adam White, Ph.D.

Biosystems Product Manager, Confocal and Super-Resolution
Nikon Instruments Inc., 1300 Walt Whitman Road, Melville, NY 11747-3064, USA

In living things, many events occur at rates much higher than those that can be captured by raster scanning linear galvos. Since the LSCM is such an important tool for biologists, there is an inherent desire to overcome this problem. One method for doing so is the use of a resonant scan mirror in the place of a fast-axis linear galvo. Resonant scanners are constructed using torsion springs that allow the mirrors to be driven at a very high frequency (often 4–8kHz) in a sinusoidal fashion. This avoids the rapid acceleration and deceleration necessitated by the sawtooth-driven linear galvo, thus providing high scan speeds with significantly less stress on the motor mechanisms. This means that full-frame 512x512 images can be captured at ~30 FPS, a temporal sampling rate that is much more compatible with live biology. In the early 1990s Nikon introduced the first commercial confocal system containing a resonant scanner, the RCM-8000. Building on the technical expertise gained in the development of this system, the current Nikon A1R has also adopted the resonant scanner in its unique hybrid scan system (Figure 1). The hybrid system contains both a traditional linear galvo pair for flexible, high-resolution imaging and a resonant scanning system for live imaging. The design of the A1R allows these light paths to be combined in a single experiment, with the linear galvos being used for photostimulation while the resonant scanner simultaneously captures dynamic cellular responses.

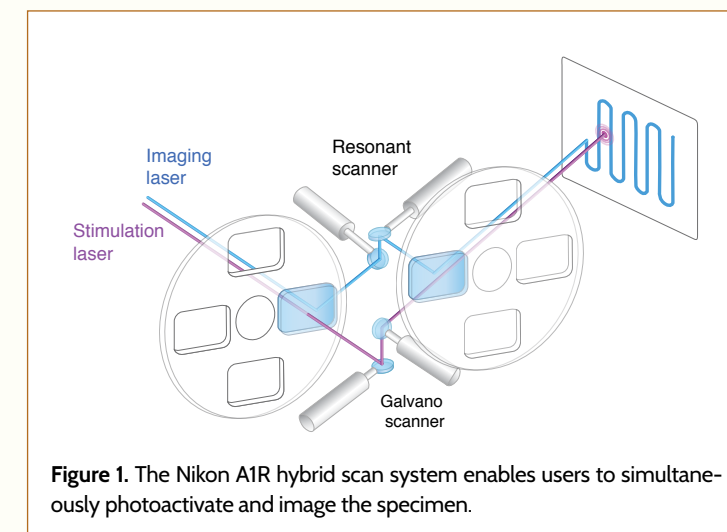


Figure 1. The Nikon A1R hybrid scan system enables users to simultaneously photoactivate and image the specimen.

A challenge presented by the use of the resonant scanner is the timing of individual pixels when driving the mirror in a sinusoidal pattern. This can be achieved by either software- or hardware-based methods, but usually limits the pixel number in the resonant axis (512 pixels in the case of the A1R). Importantly, pixel number and size define the resolution and field of view that can be achieved in a given image. Often, a pixel size that is smaller than the default for a given objective and scan area might be useful for answering a particular question. In

these cases, the 512x512 maximum image size would necessitate that the scanner sample over a smaller area, a process known as scan zooming. Recognizing a desire to increase resonant image resolution without sacrificing field of view, Nikon has developed a high resolution 1K resonant scanner (Figure 2). This new scan regime has added a more flexible timing system to the A1R in order to achieve image sizes up to 1024x1024 while still achieving a full 30FPS at 512x512. Put simply, the new 1K resonant scanner sacrifices nothing, while providing 4x the field of view at the same resolution usually generated by a normal 512x512 scanner.

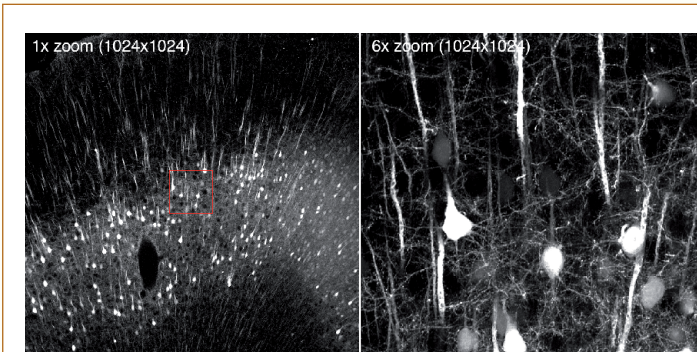


Figure 2. 1024x1024 resonant scanned image using Nikon's high-resolution 1K resonant scanner (1x zoom is shown on the left and 6x zoom on the right). H-line mouse brain slice (2 mm) cleared with RapiClear® 1.52 (Sunjin Lab). Provided by Drs. Ryosuke Kawakami, Kohei Otomo, and Tomoni Nemoto, Research Institute for Electronic Science, Hokkaido University.

Flexible Spectral Detection

Fluorescence-based microscopy has been an important driver for biological discovery since the early 1900s. However, it was the invention of immunofluorescence by Albert Coons and Melvin Kaplan in 1950 that led to the increase in specificity of fluorescent markers and thus, the development of the variety available today. In addition to these probes, advances in molecular biology and the Nobel Prize-winning discovery and application of green fluorescent protein (GFP) by Martin Chalfie, Osamu Shimomura and Roger Tsien have led to an explosion in the availability of various genetically engineered fluorescent probes. Of course, when studying biology, it is often desirable to combine several of these markers in a single experiment. This type of experiment can be complicated by the fact that fluorescent molecules emit over a range of wavelengths within the available bandwidth of the visible spectrum which, for most instruments, is only ~400 nm–750 nm. This results in the unique and familiar challenge of spectral overlap that often confuses the interpretation of these data. For example, most multichannel confocal detectors manage 3–4 separate bands at a given time. If a particular experiment necessitates 6 fluorescent probes, this detector will likely not have the spectral resolution necessary to separate the signal from each probe. However, it is critical to note that spectral information, just like temporal or spatial information, can be broken down into small segments in order to more completely understand and interpret data generated by a particular experiment. It is the idea of sampling the emission spectrum of a given specimen with a large number of smaller bands/channels that is the basis of spectral imaging.

Commercially available methods for spectral imaging can be separated into two main categories: simultaneous multispectral imaging and tunable spectral imaging. For simultaneous multispectral imaging, an image is captured in one shot that is made up of many (often up to ~32) small, individual spectral bandpasses. In short, this is usually achieved by placing a prism or something similar in the detection lightpath in order to spread light over a multichannel array detector. The width of the detection bandpasses is definable in high-end versions of these detectors and will ultimately determine the overall wavelength range and spectral resolution of a captured image. For example, a 32-channel image captured with a 2.5-nm bandpass will cover an 80-nm range (though multiples of these images can be combined to extend this range). This type of resolution is advantageous for looking at multiple probes of the same color family or for the removal of background autofluorescence in certain samples. For other applications, such as correction of cross-excitation or bleed-through from more common combinations of probes, one might define a 10-nm bandpass, which would give sufficient spectral resolution and cover a broader range in a single image. Besides high spectral resolution, a key benefit of using an array detector for spectral applications is that simultaneous capture of all channels allows experiments of this type to be carried out in dynamic living things, where motion blur and other artifacts might preclude longer sequential acquisitions.

Tunable spectral detectors are similar to the multispectral systems discussed above, in that they utilize prisms or other optical elements to break emission spectra into smaller wavelength components for interrogation. They differ in that they use physical mechanisms to stop down each bandpass, and they contain significantly fewer detector channels. What this means is that spectral profiling with these detectors is done sequentially, across several rounds of capturing and then tuning the detector elements to the next wavelength range. Though this method is slower than an array detector and is not quite capable of the same spectral resolution, these detectors generally have the benefit of lower cost and higher flexibility. In fact, one of the greatest benefits of tunable detection is the ability to use it to define wide bandpasses on the fly. This means using the detector in a fashion that is similar to traditional filter based detectors but with the advantage that the emission spectra of any visible probe can be matched at any time. The implication of this is that users no longer have to worry about whether a system contains the proper filters for a particular experiment; it's all freely definable. The recent introduction of a tunable gallium arsenide phosphide (GaAsP) detector module called the DUV-B (Figure 3) brings this capability to the entire Nikon family of confocal systems. It can be configured as the only detector on either an A1 or a C2 confocal system or can be combined with traditional, fast filter-based detectors for even more flexible experimental design. This low-cost, high-sensitivity detector has a simple interface for carrying out both traditional spectral analyses and “virtual filter”-type applications. These attributes make the DUV-B a flexible, sensitive and high-value detection solution for Nikon confocal systems.

Enhancing Confocal Resolution

Recent advances in technology have pushed the limits of the spatial

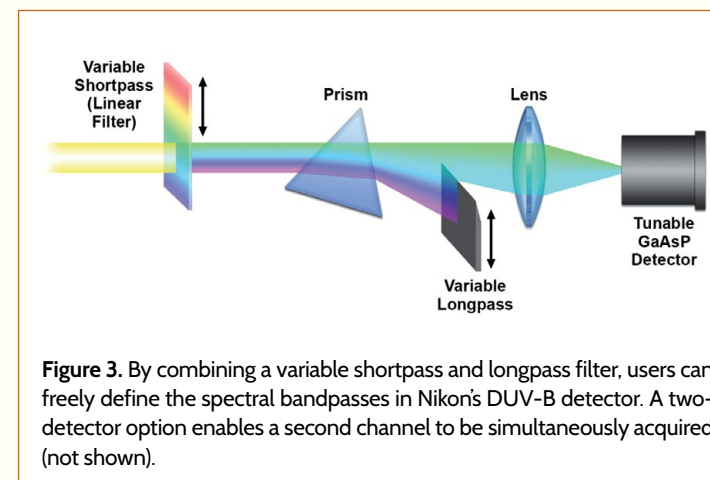


Figure 3. By combining a variable shortpass and longpass filter, users can freely define the spectral bandpasses in Nikon's DUV-B detector. A two-detector option enables a second channel to be simultaneously acquired (not shown).

resolution that can be achieved using light microscopy. These advances have included the development of “superresolution” techniques, which take advantage of particular properties of light, fluorescent probes, optics, and computation to “break the diffraction barrier.” However, for some time it has also been known that, utilizing the pinhole, one can achieve resolutions beyond traditional widefield resolution using a basic confocal microscope (reviewed in Wilson, 2011). The level of resolution improvement achieved in this case is completely dependent upon the pinhole diameter, with an infinitesimally small pinhole generating the highest improvement. Of course, an infinitely small pinhole is not practical, so investigators using this technique must carefully balance resolution improvement with signal/noise ratio.

All light that travels through a microscope system is spread, blurred and subjected to noise before it can form an image. This blurring effect has the consequence of limiting the resolution of certain details from a given sample and is known as convolution. Thankfully, by gathering specific information about the sources of convolution in a given system and defining them mathematically, algorithms can be developed to minimize the effects of this process. Application of these algorithms to an image dataset is known as deconvolution. Since deconvolution uses information about the effects of a specific system on the data it produces, it is possible to use these algorithms to reverse some of the effects of convolution and increase the overall resolution in the final data. Over the past several years, Nikon has worked to develop proprietary deconvolution algorithms that are powerful, GPU-based, and that can use convolution information gathered specifically through Nikon optics. This careful development has led to a series of fast, accurate algorithms that are suitable for a large variety of datasets captured under many different circumstances. Included in this are definitions specific to confocal microscopes that can be applied to improve contrast and resolution in any confocal dataset.

So what can be done with these two strategies for improving the resolution of confocal microscopes? The most obvious choice is to combine them for maximal resolution gain with minimal sacrifice in

signal/noise. Indeed, this is A1-ER, Nikon's solution to extending the resolution capabilities of the A1 Confocal. With this technique, users can take advantage of the extremely efficient A1 system to capture data with a reduced pinhole, when needed. Then, GPU-based deconvolution algorithms (that can take into account changes in the pinhole diameter) can be quickly applied, resulting in improved data with higher contrast and resolution (Figure 4).

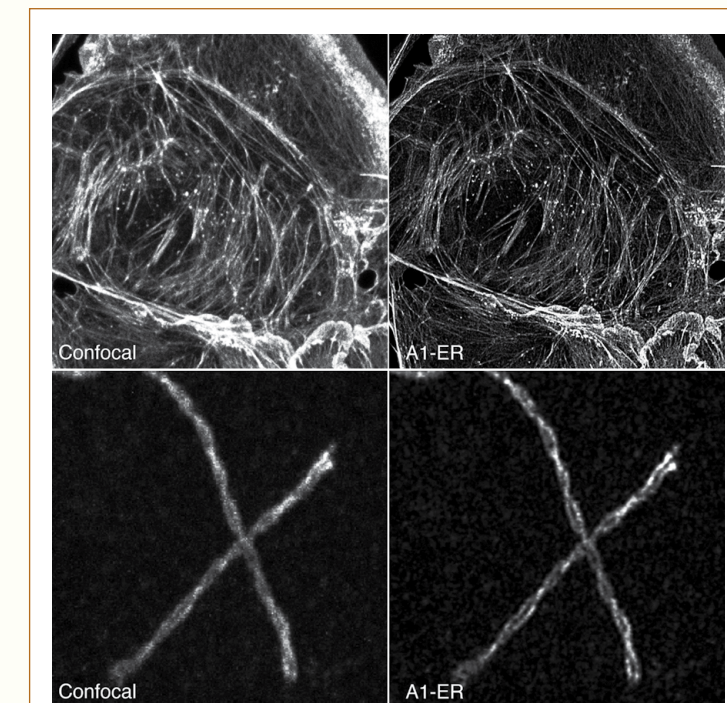


Figure 4. Comparison images between standard confocal and Enhanced Resolution. Upper panel: actin filaments; Lower panel: mouse chromosome spread.

Conclusion

Nikon's A1 confocal system is a stable confocal platform that continues to advance with the addition of new technologies. The A1's HD resonant scanner will now provide the ability to capture resonant images at higher resolution without having to sacrifice field of view. The DUV-B supplements Nikon's detector lineup with a tunable GaAsP detector that can be used for both spectral and “virtual-filter” based experiments. Finally, A1-ER synthesizes two long-understood concepts in confocal microscopy into an easy-to-use method for enhancing the resolution of A1 confocal images. The result of this combination of developments is the next major step in the continuing evolution of the A1 confocal microscope.

Reference

T. Wilson, Resolution and optical sectioning in the confocal microscope. *J. Microscopy* 244, 113-121 (2011)

The Spectrum of Resolution: Confocal, SIM, and STORM

The field of biological light microscopy is in a state of flux. The past decade has witnessed the precipitous rise and quick diversification of “superresolution” microscopy, culminating in the 2014 Nobel Prize in Chemistry. These varied techniques are designed to circumvent the conventional diffraction limit on optical resolution, and include such methods as single-molecule localization (e.g., STORM (1), PALM (2), SIM (3), STED (4)), and more.

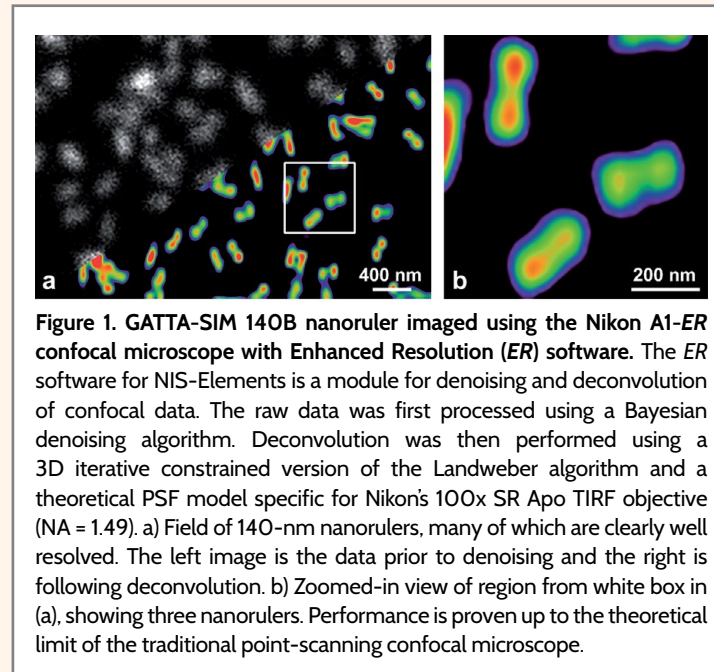
However, there is not a clearly defined threshold that must be met for a technique to be considered “superresolution”. With the recent influx of confocal-based resolution enhancing techniques, this definition has become further blurred. In general, these techniques provide up to a $\sqrt{2}$ improvement in resolution (5, 6). Nikon’s A1-ER combines high-resolution confocal microscopy with deconvolution to provide “Enhanced Resolution” (ER). Here we will show proof of resolution performance for Nikon’s superresolution and ER imaging solutions using GATTAquant® (Braunschweig, Germany) nanoruler resolution standards. We will also briefly discuss the benefits and drawbacks of each technique with respect to other performance metrics in order to help the reader decide which approach is best suited towards their research.

Enhanced Resolution with Confocal Microscopy

Deconvolution of confocal data is an old approach that has found new life due to the availability of powerful consumer-grade graphics processing units (GPUs). Analyses once requiring many hours may now be performed almost instantly (7). Realizing the full resolution of the confocal microscope requires using a sufficiently small pinhole aperture (~0.3–0.6 Airy Units), a high sampling rate, and true 3D iterative deconvolution (5). Deconvolution increases the signal-to-noise ratio (SNR) of the data, making it possible to resolve details previously obscured by noise. The theoretical resolution limit of the confocal microscope under these conditions is approximately 140 nm, which we demonstrate using the Nikon A1-ER confocal microscope in Figure 1.

John R. Allen

Applications and Marketing Specialist
Nikon Instruments Inc., 1300 Walt Whitman Road, Melville, NY 11747-3064, USA

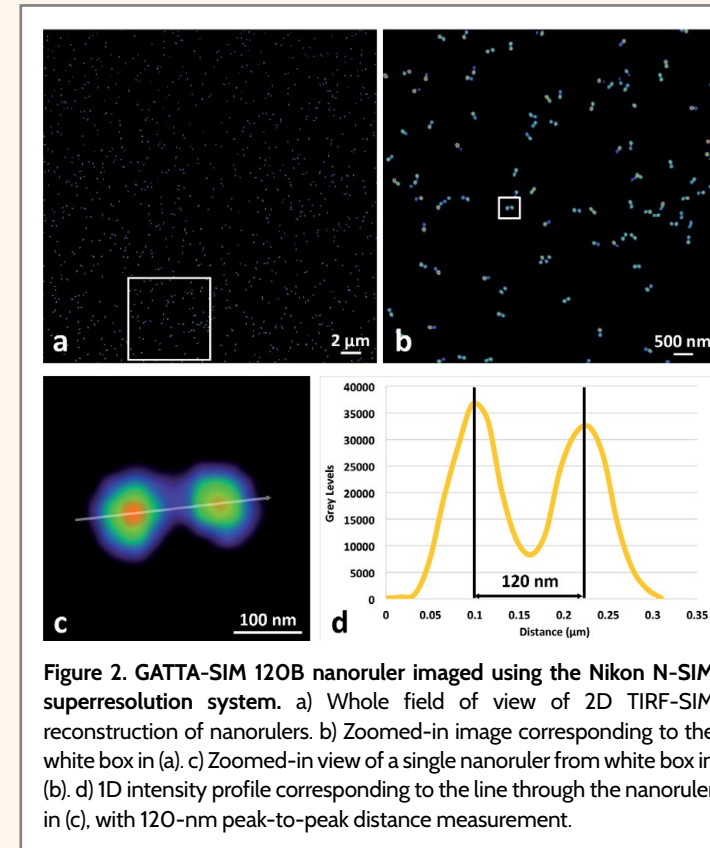


While confocal systems such as A1-ER provide greater performance than traditional widefield microscopes, they are not in the same domain as true superresolution techniques, such as SIM and STORM. However, the user retains the unparalleled flexibility of the confocal microscope, which is generally compatible with most specimens given its spectral resolving power, deep imaging capabilities, and relatively simple sample preparation. Confocal with deconvolution is thus an excellent decision for researchers requiring just a bit more resolution performance, but with less room for compromise with regard to other aspects of system performance. A1-ER may easily be realized on existing systems, and is particularly well suited for this application as it utilizes a hexagonal pinhole aperture, which is a better approximation of a circle compared to the standard square pinhole utilized by other manufacturers. The hexagonal pinhole will reject out-of-focus light more efficiently and provide better axial resolution at the same light throughput.

Structured Illumination Microscopy (SIM)

Superresolution Structured Illumination Microscopy (SIM) is a widefield interference-based technique that provides a ~2x increase in resolution compared to the diffraction-limited

case (3). A superresolution SIM image generally requires 9–15 individual widefield images at different phases and orientations of the interference pattern. While this places a fundamental limit on acquisition rate, it remains fast enough to image many dynamic processes in living systems. 120-nm lateral resolution is validated on the Nikon N-SIM system in Figure 2 below.

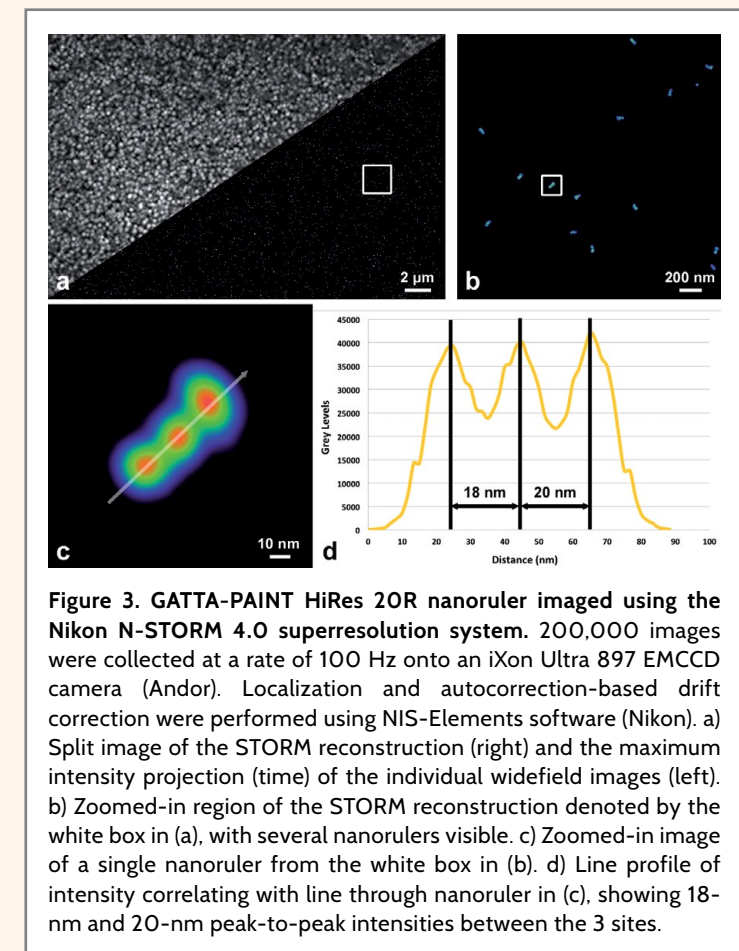


Nikon’s N-SIM system can be operated in one of three modes: 2D-SIM (9 images, lateral resolution improvement only), 2D TIRF-SIM (9 images, exceptional lateral resolution improvement to ~85 nm), and 3D-SIM (15 images, 3D resolution improvement). Up to 5 channels are available for imaging on the N-SIM.

While providing greater resolution improvement than confocal with deconvolution, SIM is more limited when applied to imaging thick specimens, generally working well up to 20 μm deep. The integrity of the interference pattern degrades quickly deeper into the specimen. More recently, systems applying the principles of structured illumination, but configured similar to traditional spinning disk confocal microscopes, have been introduced (9, 10). While able to operate at a higher frame rate, these techniques are generally limited to similar resolution improvement as point-scanning confocal microscopes with deconvolution.

Stochastic Optical Reconstruction Microscopy (STORM)

Localization microscopies such as STORM provide the greatest resolving power of any commercially available light microscopy. 20-nm optical resolution is unambiguously demonstrated in Figure 3 using Nikon’s N-STORM 4.0 system, an order of magnitude improvement over the diffraction limit. More impressively, resolution is demonstrated using autocorrelation based drift correction, precluding the requirement of adding fiducial markers to the sample.



Techniques such as STORM are best applied to fixed samples, given that a good reconstruction requires thousands of individual frames of data and high-power laser illumination. Although live-cell STORM imaging has been realized in multiple examples (11, 12), this approach is typically difficult and can suffer from motion-induced blur when attempting to capture the most dynamic processes.

Up to 3 channels may be imaged using the N-STORM system, with 6-color STORM having been demonstrated in the literature

(13). Applying either the classic STORM approach with tandem-labeled activator-reporter dye pairs (1, 13) or direct excitation of spectrally resolved probes (14) is possible. The N-STORM system has also been validated for DNA-PAINT imaging (15, 16), easing sample preparation requirements.

While a variety of localization microscopes have been demonstrated, in practice most configurations are limited to a thin monolayer of cells. This is realized with Nikon's N-STORM by combining Perfect Focus-based z-stack functionality with astigmatism-based 3D localization. Nikon's new silicon objective lens provides improved working distance for STORM and better SNR at dorsal surfaces of cells. Still, the imaging depth limit of STORM is less than SIM (~20 μm) and confocal (~100s

of μm). For imaging thick tissues with STORM, samples are generally sectioned prior to imaging in order to bypass these limitations (17, 18).

The Takeaway

Superresolution microscopies have a lot to offer, but can also impose greater limitations in other aspects of imaging—there is no perfect imaging technique. For example, confocal microscopy may offer more limited resolution improvement, but otherwise all-around robust performance well suited towards a variety of research needs. Researchers must determine the level of resolution required by an experiment and identify potential areas of compromise. In this respect, very little has changed about optical microscopy.

References

1. M. J. Rust, M. Bates, X. Zhuang, Sub-diffraction-limit imaging by stochastic optical reconstruction microscopy (STORM). *Nat. Methods* **3**, 793-795 (2006).
2. E. Betzig, G. H. Patterson, R. Sougrat, O. W. Lindwasser, S. Olenych, J. S. Bonifacino, M. W. Davidson, J. Lippincott-Schwartz, H. F. Hess, Imaging Intracellular Fluorescent Proteins at Nanometer Resolution. *Science* **313**, 1642-1645 (2006).
3. M. G. L. Gustafsson, Surpassing the lateral resolution limit by a factor of two using structured illumination microscopy. *J. Microsc.* **198**, 82-87 (2000).
4. T. A. Klar, S. Jakobs, M. Dyba, A. Egner, S. W. Hell, Fluorescence microscopy with diffraction resolution barrier broken by stimulated emission. *Proc. Natl. Acad. Sci. U.S.A.* **97**, 8206-8610 (1994).
5. J. B. Pawley, Ed., *Handbook of Biological Confocal Microscopy* (Plenum, New York, NY, 1995).
6. T. Wilson, Resolution and optical sectioning in the confocal microscope. *J. Microsc.* **244**, 113-121 (2011).
7. M. A. Bruce, M. J. Butte, Real-time GPU-based 3D Deconvolution. *Opt. Express* **21**, 4766-4773 (2013).
8. M. G. L. Gustafsson, L. Shao, P. M. Carlton, C. J. R. Wang, I. N. Golubovskaya, W. Z. Cande, D. A. Agard, J. W. Sedat, Three-dimensional Resolution Doubling in Wide-Field Fluorescence Microscopy by Structured Illumination. *Biophys. J.* **94**, 4957-4970 (2008).
9. C. B. Müller, J. Enderlein, Image Scanning Microscopy. *Phys. Rev. Lett.* **104**, 198101 (2010), DOI: 10.1103/PhysRevLett.104.198101.
10. A. G. York, P. Chandris, D. D. Nogare, J. Head, P. Wawrzusin, R. S. Fischer, A. Chitnis, H. Shroff, Instant super-resolution imaging in live cells and embryos via analog image processing. *Nat. Methods* **10**, 1122-1126 (2013).
11. S. Jones, S-H. Shim, J. He, X. Zhuang, Fast, three-dimensional super-resolution imaging of live cells. *Nat. Methods* **8**, 499-505 (2011).
12. S-H. Shim, C. Xia, G. Zhong, H. P. Babcock, J. C. Vaughan, B. Huang, X. Wang, C. Xu, G-Q. Bi, X. Zhuang, Super-resolution fluorescence imaging of organelles in live cells with photoswitchable membrane probes. *Proc. Natl. Acad. Sci. U.S.A.* **109**, 13978-13983 (2012).
13. M. Bates, G. T. Dempsey, K. H. Chen, X. Zhuang, Multicolor Super-Resolution Fluorescence Imaging via Multi-Parameter Fluorophore Detection. *ChemPhysChem* **13**, 99-107 (2012).
14. M. Heilemann, L. S. van de Linde, M. Schüttelpelz, R. Kasper, B. Seefeldt, A. Mukherjee, P. Tinnefeld, M. Sauer, Subdiffraction-resolution fluorescence imaging with conventional fluorescent probes. *Angew. Chem. Int. Ed. (English)* **47**, 6172-6176 (2008).
15. R. Jungmann, M. S. Avendano, J. B. Woehrstein, M. Dai, W. M. Shih, P. Yin, Multiplexed 3D Cellular Super-Resolution Imaging with DNA-PAINT and Exchange-PAINT. *Nat. Methods* **11**, 313-318 (2014).
16. J. R. Allen, N-STORM with DNA-PAINT for Reliable Multicolor & 3D Single Molecule Localization Imaging. <https://www.nikoninstruments.com/Learn-Explore/Application-Notes>
17. S. Nanguner, B. Flottmann, H. Horstmann, M. Heilemann, T. Kuner, Three-Dimensional, Tomographic Super-Resolution Fluorescence Imaging of Serially Sectioned Thick Samples. *PLOS ONE* **7**, e38098 (2012), DOI: 10.1371/journal.pone.0038098
18. L. Barna, B. Dudok, V. Miczán, A. Horváth, Z. I. László, I. Katona, Correlated confocal and super-resolution imaging by VividSTORM. *Nat. Protoc.* **11**, 163-183 (2015).



Nikon
100th
anniversary

A1ways Evolving

New upgrades to A1 confocal systems from Nikon extend the power of confocal microscopy and open up a world of new imaging strategies and possibilities.

The latest A1 advances include:

- New High Resolution 1K Resonant Scanner
- A1-ER (Enhanced Resolution) Module
- DUVB GaAsP Spectral Detection Unit

For more information, go to www.nikoninstruments.com/confocal or call 1-800-52-NIKON.



Nikon Instruments Inc.
www.nikoninstruments.com
nikoninstruments@nikon.net



Nikon th
100
anniversary

Explore the Nanoscale

Introducing N-STORM 5.0, the latest super-resolution imaging solution from Nikon.

Combines an ultra-stable Ti2-E imaging platform with the power of NIS-Elements to provide unprecedented flexibility in acquisition workflow. Achieve 10-fold improvement in resolution, in three dimensions, with ease.

For more information, go to
www.nikoninstruments.com/n-storm
or call 1-800-52-NIKON



Nikon Instruments Inc.
www.nikoninstruments.com
nikoninstruments@nikon.net